Formation and characterization of stochastic subwavelength structures on polymer surfaces

Dissertation
zur Erlangung des akademischen Grades
doctor rerum naturalium (Dr. rer. nat.)

Optical Coatings Department
Fraunhofer-Institute for Applied Optics and Precision Engineering

Institute of Applied Physics
Friedrich Schiller University of Jena

vorgelegt dem Rat der Physikalisch-Astronomischen Fakultät
der Friedrich-Schiller-Universität Jena

von: Dipl.-Phys. Robert Leitel
geboren am: 19.01.1980 in Jena

Gutachter

1. Prof. Dr. Andreas Tünnermann, Universität Jena
2. Prof. Dr. Hans K. Pulker, Universität Innsbruck
3. Prof. Dr. Herbert Welling, Universität Hannover

Tag der letzten Rigorosumsprüfung: 28.10.2008
Tag der öffentlichen Verteidigung: 18.11.2008

Contents

Nomenclature **II**

Abstract **1**

Zusammenfassung **2**

1 Introduction **3**

2 Optics of rough surfaces and thin films **6**
2.1 Optical properties of structured media . . . 6
2.2 Spectral properties of thin films . . . 10
2.3 Reverse engineering from optical spectra . . . 12
2.4 Rigorous calculation of spectral properties . . . 14

3 Interaction of plasmas with polymers **15**
3.1 Properties of plasmas . . . 15
3.2 Essential polymer properties . . . 16
3.3 Plasma treatment of polymer surfaces . . . 21

4 Manufacturing and instrumental analysis **33**
4.1 Generation of subwavelength structures . . . 33
4.2 Analysis of plasmas . . . 35
4.3 Simulation of ion collision cascades in polymers . . . 38
4.4 Surface topography . . . 39
4.5 Optical spectroscopy . . . 44

5 Research on subwavelength structures **48**
5.1 The erosion process . . . 48
5.2 Antireflection effect . . . 55
5.3 Structure formation . . . 61
5.4 Reverse engineering from optical spectra . . . 74
5.5 Origins of optical loss . . . 83
5.6 Aspects of self-organization . . . 86

6 Conclusions **88**

References **90**

Acknowledgments **101**

Curriculum vitae **103**

Nomenclature

AFM	atomic force microscopy
AR	antireflection
ATR	attenuated total reflection
dc	direct current
EMA	effective medium approximation
FDTD	finite difference time domain
FEM	finite element method
FWHM	full width at half maximum
IRRAS	infrared reflectance absorption spectroscopy
LIPSS	laser-induced periodic surface structures
MCM	Monte Carlo method
MF	merit function
MW	microwave
PA	polyamide
PC	polycarbonate
PET	polyethylenterephthalate
PMMA	polymethylmethacrylate
PSD	power spectral density
RCWA	rigorous coupled-wave analysis
RF	radio frequency
SEM	scanning electron microscopy
SWS	subwavelength structure
XPS	x-ray photo-electron spectroscopy

A	area
α	absorption coefficient
α_i	degree of ionization
β	phase constant
c	free-space velocity of light
C	surface concentration of mobile species

γ	damping constant
$\Gamma_{(x)}$	Number of x atoms per monomer, $C\ldots$carbon, $O\ldots$oxygen
d	thickness
d_i, d_p	penetration depth
D_S	surface diffusivity
e	elementary charge
E	energy
$\mathbf{E}$	electric field strength
ϵ_0	electric constant
$\epsilon_{(i)}$	complex dielectric function (of the material i)
$\epsilon_{\textsf{eff}}$	effective dielectric function
f	frequency (of quartz crystal monitor)
f_j	oscillator strength
$\mathbf{F}$	Coulomb force
h	height
h	Planck's constant
η	half cone angle
Θ	angle of light incidence
i	imaginary unit
i, j	numerical index (subscript)
$I_{(0)}$	Intensity
J, J_i	ion flux
k_B	Boltzmann constant
$k_{x,y}$	spatial frequency in x, y-direction
κ	extinction coefficient
l	length (lateral)
λ	wavelength
λ_0	center wavelength
λ_D	Debye length
Λ	(effective) period
$m_{(e,i)}$	(electron, ion) mass
μ	permeability
$n_{(x)}$	refractive index (of material x), $a\ldots$ambient, $s\ldots$ substrate
n'	complex refractive index
$N_{(x)}$	particle density (of x), $e\ldots$electron
$\nu_{(x)}$	volume filling factor (of material x)
p	pressure

$\mathbf{p}$	dipole momentum
$\mathbf{P}$	dielectric polarization
q	electric charge
$\mathbf{r}$	position vector
r	electric field reflection coefficient
R	reflectance
ρ	specific gravity
S	scatter loss
σ	rms-roughness
t	electric field transmission coefficient
t	time
T	transmittance
T_e	electron temperature
T_g	temperature of glass transition
TS_b	total backscattering
TS_f	total forward scattering
τ	depolarization factor
U_B	bias voltage
U_C	counter voltage
U_P	plasma potential
Υ	spectral data
v_c	critical (Bohm) velocity
V	volume
φ	angle of incidence
Φ	etch rate
Φ_S	sputtering yield
x, y, z	components of propagation
χ	susceptibility
ω	angular frequency
ω_0	eigenfrequency of a resonance
ω_p	plasma frequency
Ψ	net rate of re-deposition

Abstract

When polymethylmethacrylate (PMMA) is exposed to argon/oxygen low-pressure plasma, a stochastic aligned surface morphology forms under certain conditions. The plasma-treated surface shows a notable transmittance increase in the visible spectral region. The principle of antireflective subwavelength structures is also used in nature to increase the efficiency of the light coupling into the "moth's eye". Moreover, the technology is an inexpensive alternative to the deposition of interference coatings to increase the light transmission of polymeric optical elements. This work is driven by the need to fabricate such broadband antireflective morphologies on arbitrary shaped surfaces of different kinds of polymeric substrates.

Beside PMMA, three transparent thermoplasts (polyamide, polyethylenterephthalate, polycarbonate) have been chosen to analyze the underlying physical processes in order to understand the structure formation during plasma treatment. The plasma's optical emission spectra, the mass loss of the polymers, and the surface temperature of the substrate have been measured *in situ* to get an idea of the erosion process. The plasma-polymer interaction was supported by Monte Carlo method to investigate the energy transfer of the impinging ions on the polymer substrate. The optical effect of the structured surfaces has been optimized for the polymers by the use of spectrophotometry that was also available during the etch process. The structure formation has been analyzed by atomic force microscopy and scanning electron microscopy. The revealed effective pin shape was correlated with the results from spectral reverse engineering.

The structure formation has been established on the surface of the four tested polymers and shows a self-organized nature, since the topography was not prescribed from outside before or during the process. The revealed differences in size, shape, and antireflective effect are specific for the particular polymer. The structure formation results from a combination of physical sputter-erosion and chemical etching. Aspect ratios of the pin structure of height / width > 1 can only be explained by anisotropic etching due to impact of high energetic plasma-ions. The subwavelength structure has been modeled as effective medium, which allows for the subsequent calculation of the optical properties by means of interference coatings with nonlinear refractive index gradients. The occurrence of scatter losses can be kept low and might be negligible for many applications. Particular PET surfaces show a high, industrially appropriate transmittance increase in the visible spectral region after plasma treatment.

Zusammenfassung

Die Behandlung von Polymethylmethacrylat (PMMA) durch ein Niederdruckplasma führt zur Ausbildung einer stochastischen Oberflächenstrukturierung. Die laterale Ausdehnung der individuellen Struktureinheiten ist deutlich kleiner als die Wellenlänge des Lichtes des sichtbaren Spektralbereichs, wodurch sie entspiegelnde Eigenschaften analog zu den bekannten „Mottenaugen-Strukturen" aufweisen. Da diese Topographie weder vor noch während des Prozesses von außen vorgegeben wird, liegt es nahe das Wachstum auf Selbstorganisation zurückzuführen. Diese Arbeit wird motiviert durch den industriellen Wunsch nach einer generellen Methode zur breitbandigen Entspiegelung von Oberflächen organischer Gläser durch Subwellenlängen-Strukturen.

Dazu werden neben PMMA noch drei weitere Materialien (Polyamid, Polyethylenterephthalat, Polycarbonat) in die Untersuchungen zum Verständnis der Strukturentstehung einbezogen. Die optischen Plasmaemissionen, die Ätzrate der Polymere und die Oberflächentemperatur der Substrate werden *in-situ* aufgezeichnet, um den Materialabtrag zu charakterisieren. Die Analytik der Plasma-Polymer-Wechselwirkung wird gestützt durch Monte-Carlo Simulationen der Stoßkaskaden der auf die Polymeroberfläche auftreffenden Plasmaionen. Die optische Wirkung der strukturierten Oberfläche wird für die ausgewählten Polymere mit Hilfe der Spektralphotometrie optimiert, die auch während des Ätzvorgangs *in-situ* zur Verfügung steht. Die Strukturentstehung selbst wird mit Rasterkraft- und Rasterelektronenmikroskopie untersucht, wobei die ermittelten Strukturdimensionen über ein Effektiv-Medium-Modell mit den Ergebnissen der spektralen Rückrechnung korreliert werden.

Auf den Oberflächen der untersuchten Polymere konnte eine noppenartige Subwellenlängen-Struktur nachgewiesen werden, die eine breitbandige Entspiegelungswirkung im sichtbaren Spektralbereich zeigt. Die Unterschiede in Größe, Form und entspiegelnder Wirkung ergeben sich sowohl materialspezifisch als auch durch die Wahl geeigneter Prozessparameter. Die selbst-organisierend entstehende Struktur resultiert aus der Kombination von physikalischen Sputter-Abtrag und chemischen Ätzen. Ihr Aspektverhältnis von Höhe : Breite > 1 kann nur durch anisotropes Ätzen der hochenergetischen Plasma-Ionen erklärt werden. Der Subwellenlängen-Charakter der Topographie ermöglicht die Modellierung der strukturierten Grenzfläche durch ein effektives Medium und erlaubt damit die optische Beschreibung als Interferenzschicht mit einem nichtlinearen Brechzahlgradienten. Durch die Verwendung geeigneter Prozessparameter kann der Streulichtverlust im sichtbaren Spektralbereich deutlich unter 0,5% gehalten werden und ist damit für viele Anwendungen vernachlässigbar. Neben PMMA zeigt insbesondere PET eine gute, industriell nutzbare Transmissionserhöhung nach Plasma-Strukturierung.

1 Introduction

The reduction of Fresnel reflections of surfaces is one of the most demanding challenges in optical engineering. Typical optical systems consist of several elements and their imaging suffers from low brightness, little contrast, and the occurrence of ghost images, as long as each interface contributes with its typical reflectivity.

In fact, first efforts in reducing the reflection have been done in 1817 by Joseph von Fraunhofer who investigated the roughening of glass surfaces by sulfuric acid [1]. But with the upcoming success of vacuum technology the first commercial antireflection (AR) products based on interference coatings like the T-Belag from Smakula [2]. In general, interference coatings for AR purposes consist of several homogeneous layers of different materials having thicknesses in the scale of the wavelength [3]. However, today this technique is a standard process for glass and crystal optics.

It has been pointed out that the AR performance can be further improved by using inhomogeneous layers which have a continuously varying refractive index profile normal to the surface [4, 5]. Several attempts have been reported in literature to achieve so-called graded-index layers, whereas the change in the refractive index is induced by co-deposition of two materials [6], changing reactive gas flows during deposition [7], a variation of material's porosity (sol-gel) [8], or surface texturing with subwavelength structure (SWS). Following Bernhard [9], who discovered this effect at the cornea of nocturnal moths (Fig. 1.1, left), the latter is called "moth-eye's structure".

Quite apart from their optical performance, structured surfaces of this type offer additional advantages having no problems with adhesion or with diffusion of one material into another. Since they are monolithic and do not introduce additional material, they tend to be more stable and durable than multilayer dielectric coatings, particularly when used with high-powered lasers [10]. The strongly increased roughness can be used to amplify the chemical properties of the surface (e.g., wetting behavior) [11, 12]. On the contrary, they are generally more sensitive to mechanical damage.

The first realizations of ordered SWS were gratings for the near infrared region manufactured by holographic or lithographic methods [13]. Nowadays, surface areas up to 0.7 $\times$ 0.7 m^2 are textured to suppress the reflection in the visible [14]. The scalability and its application to complex-formed surfaces like aspheres or diffractive optical elements are the main difficulties of this approach. Self-assembling processes at the surface leading to stochastically arranged structures could overcome these problems. Most recently, a method has been developed that forms self-organized SWS (Fig. 1.1, right) by applying low-pressure plasma etching on polymethylmethacrylate (PMMA) [15].

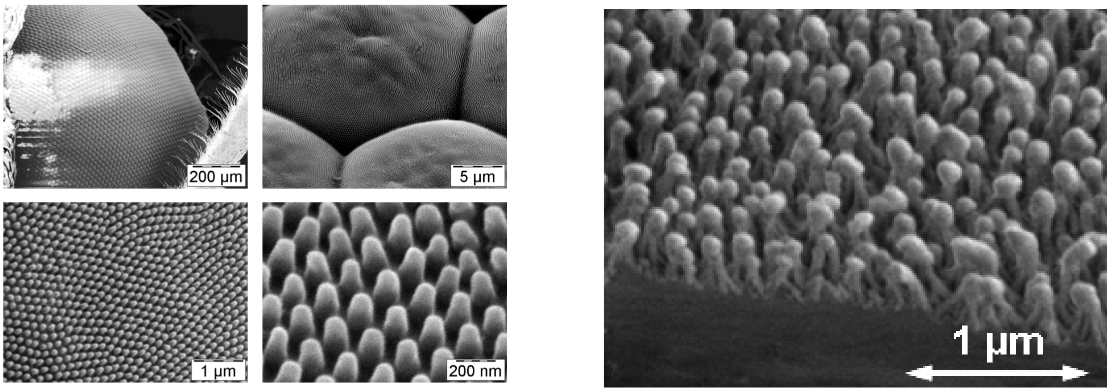

Fig. 1.1: *Scanning electron micrographs of natural moth's eye structures and the artificial subwavelength structure on PMMA by plasma treatment.*

Nowadays, self-organized processes are of great interest in industry to generate easily large quantities of small and tailored structures, but the underlying principles are not well-understood. Thus, a focus of this thesis is to extend the understanding of the mechanisms that lead to the spontaneous structure formation on polymer surfaces by plasma etching. Therefore, typical interactions of the plasma particles with the polymer surface have to be specified that cause the degradation and erosion. The behavior is compared with models that describe similar structure formation processes on semiconductor surfaces by ion-beam sputtering [16] and reactive ion etching [17].

The intense characterization of the current used plasma is the groundwork, which allows for subsequent optimization of the plasma conditions in order to improve the current process, apply the method to other polymeric materials, and to adapt this technique to inline geometry. So far, a *Syrus*$^{\text{pro}}$ box coater from *Leybold Optics* equipped with an *Advanced Plasma Source* is used which provides a dc-plasma with argon and oxygen ions of an energy around 100 eV in a pressure range of 10^{-2} Pa. Identifying the essential plasma conditions is helpful for the industrial user to be independent of proprietary process equipment.

First interrelations between plasma parameters, which affect the ion energy and pressure, and process speed have been analyzed by Kaless [18] for PMMA. Most recently, the generation of such a surface morphology was confirmed by another group that used RF plasma sources operating with oxygen as solitary process gas at $p = 0.75$ Pa and providing an ion energy around 100 eV [19]. Moreover, similar sub-micron patterning was observed for polyetyleneterephthalate (PET) [20] and opaque polyoxymethylen [21] during plasma treatment.

However, a great number of transparent thermoplastics exist for the VIS region beside PMMA and their usage is often driven by non-optical properties, like high softening temperatures, good breaking strength, low water adsorption, or biocompatibility. Hence, it is important from the application's point of view to be able to generate antireflective SWS on various polymer surfaces independent from their kind. Polycarbonate (PC), polyamide (PA), and PET have been chosen from the great diversity of polymer grades beside PMMA in order to investigate the structure formation. This includes a detailed view on collision cascades by applying Monte Carlo method as well as a review on the decomposition of polymers due to plasma-induced chemical reactions.

Revealing the nature of SWS is still challenging, since the size of the features is on a scale that optical microscopy cannot resolve. The treatment of stochastically distributed SWS is even more sophisticated due to their varying dimensions and spacings. Thus, the second aim of this work is to find adequate characterization techniques which can describe the nature of stochastic SWS. Therefore, scanning probe techniques namely atomic force microscopy (AFM) and scanning electron microscopy (SEM) have been applied.

Spectrophotometry is a contactless and non-destructive tool for determining the surface properties, e.g. by scatterometry [22]. The focus on optical characterization is founded on the technological need for optimal AR performance and the evaluation of the structured polymer surfaces regarding their potential for industrial application. In this context, the use of *in situ* optical monitoring during the etching process is also helpful in finding the shut-off time for the best AR performance [23].

Rigorous coupled wave analysis (RCWA) [24] is applied to correlate the spectral properties directly with typical shape parameters like pin height, width, and period. The comparison of continuous and discrete (binary) subwavelength gratings for AR surfaces revealed that the continuous design has to be always deeper than the discrete one to achieve an equivalent AR effect [25]. Actually, this method is suitable to describe periodic morphologies like gratings rather than a stochastic topology, but the introduction of averaged pin shapes may lead to satisfactory results.

Since the typical feature sizes are considerable smaller than the wavelength of the visible light, it is appropriate to model the structured surface as a layer of an effective medium, that has a mean refractive index [26]. The needle shape leads to a continuously varying gradient, fading the refractive index from the substrates value at the ground of the pits to the ambient's one at the top of the needles [27]. Now, the structured surface can be treated as interference coating by using the matrix method [28] to compute reflectance and transmittance. Because closed-form solutions for the calculation of the spectral properties from complex-shaped gradients do not exist, the layer has to be sliced into sufficiently thin sub-layers with homogeneous refractive indices.

The spectral reverse engineering to reveal structural information from optical data causes multiple solutions for homogeneous layer systems [29] and even more for heterogeneous coatings [6, 30]. At first, *a priori* information about the refractive index profiles are used from non-optical characterization techniques in order to constrain the parameters. Subsequently, analytic gradient functions are applied that reduce the number of variable parameters in the optimization task. In the end, both methods are combined in order to obtain real-time information about the structure formation from *in situ* recorded optical spectra.

2 Optics of rough surfaces and thin films

The surface is a region that separates two phases of different physical properties from each other and covers typically a few atomic layers [31]. Due to the perturbation of isotropy, surface forces appear that lead to a geometrical rearrangement of atoms. This microscopic picture of the surface is mentioned by the term "structure". In this context, the term "morphology" identifies the macroscopic shape of the surface and "texture" is introduced as pattern of arbitrary many individual structural elements. But, how to distinguish between microscopic and macroscopic features regarding the surface depicted in Fig. 1.1? If, on the one hand, x-rays or scanning probes are able to reveal interatomic details on the sub-nano scale and, on the other hand, light of the visible spectral region cannot resolve the morphology in a sub-micron scale, it is useful to introduce an intermediate, or mesoscopic scale [32]. In this regime, most of the appearing phenomena can be explained by the use of semi-classical approaches, where the sum of the individual quantum mechanical behaviors of a huge mass of particles lead to a collective effect that deviates from the predictions of classical physics. Being aware to the differences in their original meaning, the term structure is used, if referred to individual elements, and morphology is applied when related to the surface as a whole.

A fundamental property of a surface is its roughness, which denotes the deviation from an ideally smooth boundary. The rougher a surface the more intense is the effect of atomic rearrangement on the interface properties. As surfaces roughen by deposition [33] or erosion [34], their roughness scaling varies. A description of the dynamical scaling was given by [35] and [36]. Typically, the roughness is associated with randomly distributed surface features, but the arrangement of features in Fig. 1.1 is in a highly regular fashion. The introduction of effective and rigorous models that treat the optical properties of rough surfaces is necessary to understand the antireflective behavior and to be able to analyze the optical spectra be means of reverse engineering.

2.1 Optical properties of structured media

It is sufficient to use the classical models for the optical characterization of the applied polymers to describe the response of the materials in the presence of an electro-magnetic field. For the concerned wavelengths and intensities the effects of quantum theory do not play an important role. First the optical properties refractive index n and extinction coefficient κ are derived for isotropic homogeneous non-magnetic materials ($\mu \approx 1$). Understanding the structures as a heterogeneous mixture of different materials an artificial medium can be composed, that shows an effective refractive index. The premises for applying a so-called "effective medium approximation" (EMA) and its theory are given in the second step.

Starting from the motion of a charged particle that feels a driving Coulomb force $\mathbf{F} = q\mathbf{E}$ from a local periodic electric field $\mathbf{E}$, the model of an damped vibrating oscillator is appropriate:

$$\ddot{\mathbf{r}} + \gamma\dot{\mathbf{r}} + \omega_0^2\mathbf{r} = \frac{q}{m}\mathbf{E} \quad . \tag{2.1}$$

The eigenfrequency of the oscillator is given by $\omega_0/(2\pi)$. Because the considered polymeric materials are dielectric, their radiation-interacting electrons are bounded and γ describes their damping. The moving electrons of the density N induce dipole momentums $\mathbf{p} = q\mathbf{r}$ and lead to a dielectric polarization $\mathbf{P} = N\mathbf{p}$ and (2.1) can be rewritten:

$$\ddot{\mathbf{P}} + \gamma\dot{\mathbf{P}} + \omega_0^2\mathbf{P} = \frac{q^2N}{m}\mathbf{E} \quad . \tag{2.2}$$

In this equation $\mathbf{E}$ describes the electric field, averaged from the external field and the dipole fields of the medium. Using a fourier ansatz for $\mathbf{P}$ (and $\mathbf{E}$): $P(t) = \int_{-\infty}^{\infty} \bar{P}(\omega)e^{-\mathrm{i}\omega t}d\omega$ it follows:

$$\bar{\mathbf{P}} = \frac{q^2N}{m}\frac{1}{\omega_0^2 - \omega^2 - i\gamma\omega}\bar{\mathbf{E}} = \epsilon_0\chi(\omega)\bar{\mathbf{E}} \quad . \tag{2.3}$$

The equation introduces the complex-valued frequency-dependent susceptibility χ of the medium. This model can be enhanced to multiple resonances j, and under consideration of the contribution of the free charge carriers ($\omega_0 = 0$) the complex dielectric permittivity is given by:

$$\epsilon(\omega) = 1 + \sum_j \frac{f_j^2}{\omega_{0j}^2 - \omega^2 - \mathrm{i}\gamma_j\omega} + \frac{\omega_p^2}{-\omega^2 - \mathrm{i}\gamma\omega} \quad . \tag{2.4}$$

Now $f_j = \sqrt{\frac{q^2N_j}{\epsilon_0 m_j}}$ assigns the oscillator strength of the j$^{\text{th}}$ resonance, and the plasma frequency $\omega_p = \sqrt{\frac{N_e e^2}{\epsilon_0 m_e}}$ is introduced. It describes the eigenfrequency of an oscillating quasi-neutral free electron distribution of the density N_e. The complex refractive index of a material is defined as:

$$n' = n + \mathrm{i}\kappa = \sqrt{\epsilon(\omega)} \quad , \tag{2.5}$$

where the real part n is responsible for the reduction of the EM wave's phase velocity to c/n, while the extinction coefficient κ is responsible for the damping of the wave's amplitude. In typical heterogeneous media n and κ vary in spatial dimensions, which are larger than the wavelength λ and the propagation may be described by the laws of diffraction, refraction and reflection.

Assuming now light of the visible spectral region, the wavelengths are at least twice the lateral dimensions of the stochastic surface features. Consequently the structure is too fine to give rise to diffraction in the usual sense, but is too coarse for the medium to be considered as homogeneous.

For this, a full description can only be achieved through a rigorous solution of Maxwell's equations, which is discussed in sec. 2.4.

The effective medium theory represents a connection between the optical properties of the pure materials and the average optical response of the composition, performing a homogenization. The mixing models differ mainly in their way of describing the microstructure, and only some of them can be regarded in this work. At this level the results from the measurements of surface topology (4.4) have to be incorporated. To substitute the given SWS by an artificial medium, the knowledge from works of gratings and periodic media is helpful. Three basic conditions have to be fulfilled [26].

The **first condition** is that only the zeroth diffraction orders propagate in the substrate and in the incident medium, all the other orders have to be evanescent. Whether a diffraction order propagates or not, is given by the grating equation [37], and it follows a limitation for the materials' refractive indices (n_a, n_s), angle of light incidence θ and maximum lateral structure size Λ:

$$\frac{\Lambda}{\lambda} < \frac{1}{\max(n_a, n_s) + n_a \sin(\varphi)} \quad \xrightarrow{n_a=1} \quad \frac{\Lambda}{\lambda} < \frac{1}{n_s + \sin(\varphi)} \quad . \tag{2.6}$$

This means that for normal incidence ($\varphi = 0°$), a typical refractive index ($n = 1.5$) and the short limit of the VIS range ($\lambda = 400$ nm) the lateral sizes have to be smaller than about 270 nm. Additionally this should be valid for oblique incidence, where $\varphi = 90°$ reveals $\Lambda < 160$ nm. The scattering as the result of the diffraction into higher-orders, which is still detected for oblique angles, is caused by the violation of a second condition. Eq. 2.6 provides the cut-off value solely dependent on the diffraction geometry, which is necessary but not sufficient.

The **second condition** takes the grating geometry into account and is related to the number of propagating modes that are able to propagate under oblique angle within the structured medium. The fact that only one mode propagates for a given wavelength depends mainly on structure geometry and weakly on the diffraction geometry ($n_a \cdot \sin(\varphi)$). The shape of the grooves is described by the height-dependent filling factor ν. For $\Lambda < \lambda/\max(n_a, n_s)$ this condition is fulfilled for all filling factors, but for $\lambda/\max(n_a, n_s) < \Lambda < \lambda/\min(n_a, n_s)$ this is valid only for small ν of the high-index polymeric material.

The **third condition** is related to the grating depth. If the depth is small enough, the evanescent modes that are created at the top and the bottom interfaces may tunnel through the structured region and participate with the fundamental to the beam interference. In the case of dielectric binary gratings the grooves should be deeper than an optical quarter wave [38].

For periodical topologies like stratified media or 1D gratings the effective permittivity can be assumed as follow:

$$\begin{aligned} \epsilon_{\text{eff}} &= \sum_i \nu_i \epsilon_i \\ \epsilon_{\text{eff}}^{-1} &= \sum_i \nu_i \epsilon_i^{-1} \quad , \end{aligned} \tag{2.7}$$

where the former is valid, if the field vector $\mathbf{E}$ is perpendicular to the grating vector $\mathbf{K}$, and the latter describes the parallel case. For more accurate calculation of grating periods that are only slightly smaller than incident wavelength, transcendental equations for the second-order effective permittivity with respect to the period-to-wavelength-ratio Λ/λ can be found from Rytov [39].

Only minor work was already done in the extension of EMA for 2D-gratings. Grann *et al.* derived a formula for the static case, which means no consideration of the grating period, or $\Lambda/\lambda = 0$. For the materials 1, 2 and the filling factors of two linearly independent spatial directions ν_x, ν_y follows [40]:

$$\epsilon_{\text{eff}} = \epsilon_1 \nu_x \nu_y + \epsilon_2 (1 - \nu_x \nu_y) = \epsilon_1 \nu_x^2 + \epsilon_2 (1 - \nu_x^2) \quad . \tag{2.8}$$

The reduction $\nu_x = \nu_y$ is valid for the symmetric case. Since $\nu < 1$ it is obvious that in the 2D-case the influence of material 1 on ϵ_{eff} is smaller than in 1D for the same filling factor (cp. eq. 2.7).

To get back to the stochastic distribution of the surface features, the period has to be replaced by a quantity that describes the lateral distances between the pins best. By statistical averaging a "mean" or "effective" period can be constructed, which represents the behavior of most of the features. But, far from the average there will exist pins that cause a violation of the conditions due to their deviating size, distance, or shape. Large distances lead to a breach of eq. (2.6). The diffraction can affect a broad range of angles due the stochastic distribution, which is noticed as scattering. Small pins between larger ones can violate the third condition.

A second class of effective medium models arise from dilute systems, where only one phase is dominant (host medium ϵ_H) and the others are of minor fraction (inclusions ϵ_i). If the influence of the inclusions' different polarization is taken into account in the susceptibility χ (cp. eq. 2.3) their effective permittivity can be calculated by the use of the shared equation:

$$\frac{\epsilon_{\text{eff}} - \epsilon_H}{\epsilon_{\text{eff}} + \tau \epsilon_H} = \sum_i \nu_i \frac{\epsilon_i - \epsilon_H}{\epsilon_i + \tau \epsilon_H} \quad , \tag{2.9}$$

with specific assumptions [41]:

- Lord Rayleigh [42]: $\epsilon_H = 1$; suited to amorphous, porous media that are embedded in air or vacuum
- Maxwell Garnett [43]: the small fraction of inclusions ϵ_i are surrounded completely by the host ϵ_H; the materials are not equivalent and interchange leads to different results; proved for metal nano-particles in dielectric materials (metal island films); for $\epsilon_H = 1$ it is equivalent to Lord Rayleigh model
- Bruggeman [44]: $\epsilon_H = \epsilon_{\text{eff}}$; the inclusions are embedded in the host medium with the effective refractive index; left-hand side of 2.9 is equal to zero; the self-consistent model is used most often for all-dielectric compositions.

The shape of the inclusions is regarded by its influence on polarization described by the depolarization factor τ, with $\tau = 2$ for spheres, $\tau \rightarrow 0$ for oblate and $\tau \rightarrow \infty$ for columns. At the limits of τ the eq. (2.9) transforms into (2.7). There exist various enhancements and improvements to fit the model to specific topologies [45, 46, 47, 48].

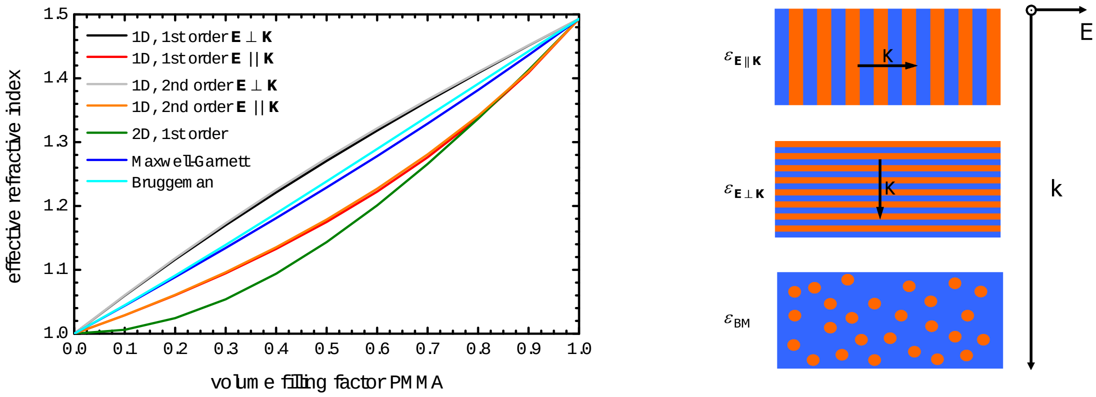

Fig. 2.1: *Effective refractive index vs. volume filling factor of PMMA (n = 1.49) for the discussed EMA (left), and structure geometry related to light's incidence (right).*

Fig. 2.1 shows the effect of the different models on the filling-factor-dependent refractive index of a PMMA-air mixture. The boundaries for n_{eff} are given in the 1D case by (2.7). If the fraction of one material's phase is small the graphs do not deviate much, but in the case of $\nu = 0.5$ differences are noticeable between the two classes of EMA. The second-order enhancements are not of great importance, since the ratio $(\Lambda/\lambda)^2 \approx$ (100 nm / 400 nm)^2 $=$ 0.06 is still small enough. The 2D-case shows especially for small ν of PMMA a remarkable lower refractive index than the other EMAs.

2.2 Spectral properties of thin films

With the help of the effective medium theory the structured surface can be described as a smooth surface that is laterally homogeneous. In the region, where the pins are, the filling factors (and the average refractive index) change continuously with increasing depth. The SWS acts in this model as a thin-film on the substrate which exhibits a gradient that alters the refractive index along its thickness d. Because the film thickness is in the order of the wavelength of incident light, the interference has to be considered in modeling.

The polarization-dependent electric field transmission t and reflection r coefficients of a surface between two media (n_1, n$_2$) is described by Fresnel's formulae:

$$\begin{aligned} t_p &= \frac{2n_1\cos(\varphi_1)}{n_2\cos(\varphi_1)+n_1\cos(\varphi_2)} & t_s &= \frac{2n_1\cos(\varphi_1)}{n_1\cos(\varphi_1)+n_2\cos(\varphi_2)} \\ r_p &= \frac{n_2\cos(\varphi_1)-n_1\cos(\varphi_2)}{n_2\cos(\varphi_1)+n_1\cos(\varphi_2)} & r_s &= \frac{n_1\cos(\varphi_1)-n_2\cos(\varphi_2)}{n_1\cos(\varphi_1)+n_2\cos(\varphi_2)} \quad . \end{aligned} \tag{2.10}$$

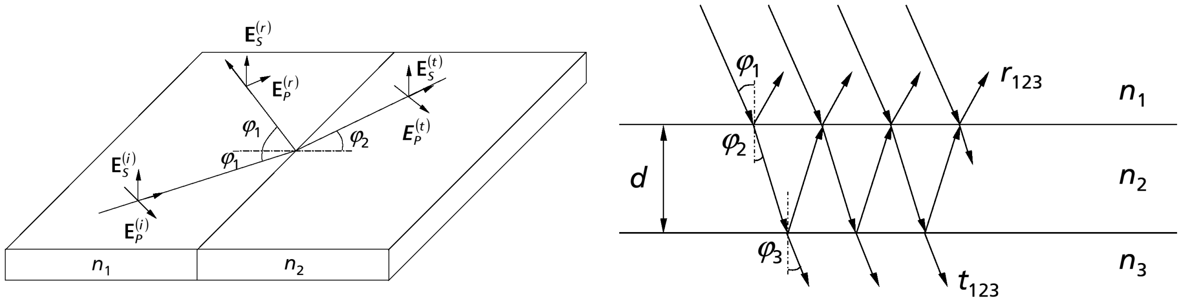

Fig. 2.2: *Behavior at a phase boundary for visualization of Fresnel's equations (left), and the path of rays for multiple beam interference for a thin film on a substrate (right).*

According to Fig. 2.2 (left) p and s denote the polarization states. In the case of a thin-film on a substrate the two interfaces ambient-film ($1 \leftrightarrow 2$) and film-substrate ($2 \leftrightarrow 3$) have to be considered and multiple beam interference occurs Fig. 2.2 (right). The overall field coefficients and the intensity-related transmittance and reflectance are given in [49]:

$$\begin{aligned} t_{123} &= \frac{t_{12}t_{23}e^{\mathrm{i}\beta}}{1 - r_{21}r_{23}e^{2\mathrm{i}\beta}} \longrightarrow T = \frac{n_3\cos(\varphi_3)}{n_1\cos(\varphi_1)}\left|t_{123}\right|^2 \\ r_{123} &= \frac{r_{12} + r_{23}e^{2\mathrm{i}\beta}}{1 - r_{21}r_{23}e^{2\mathrm{i}\beta}} \longrightarrow R = \left|r_{123}\right|^2 \quad . \end{aligned} \tag{2.11}$$

The phase difference is introduced by $\beta = \frac{2\pi}{\lambda} d\sqrt{n_2^2 - \sin^2(\varphi_1)}$, assuming $n_1 = 1$. The film is antireflective, if the numerator of r_{123} equals zero. At normal light incidence, this is known as quarterwave condition and is achieved for $n_2 = \sqrt{n_1 n_3}$ and the optical thickness $nd = \lambda_0/4$. The film generates a full antireflection effect at the center wavelength $\lambda_0/4$ ($T(\lambda_0) = 1$, $R(\lambda_0) = 0$) Around this wavelength the reflectance increases due to the non-optimal phase-match of the interfering waves. For the optical thickness $\lambda_0/2$ the waves will interfere with no phase difference and the intensity in reflection is equal to that of the substrate – the layer is optical ineffective.

Eqs. 2.11 are the solution of a homogeneous film. But as shown in the section before, it is necessary to derive the spectral properties of a refractive index gradient. Closed-form expressions of such inhomogeneous layers exist only for a few number of refractive index profiles: linear, exponential, hyperbolic [50] or small index variations [51, 52]. For all other cases the reduction to thin homogeneous slices is an appropriate method of approximation. For a sufficient approximation the number and the thickness of the slices should depend on the steepness of the gradient in a way that only small refractive index jumps emerge. Afterwards the calculation of the spectral performance is done layer by layer with the help of a matrix formalism [28]. Today, this algorithm is transferred into several notations [3, 53, 54] and is implemented in most software packages [55, 56, 57]. Thus, it is a solved problem to achieve the optical spectra from an inhomogeneous film, if the refractive index and the thickness are known.

The performance of several antireflection principles is demonstrated in Fig. 2.3 using single layers.

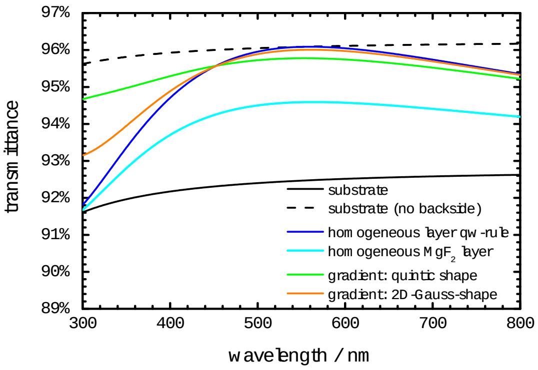

Fig. 2.3: *Transmission spectra for various approaches to increase the transmittance of a PMMA sample (absorption neglected).*

The dashed line shows the theoretical limit of a perfect antireflective surface. The residual reflection contributes only from the non-modified substrate backside. A homogeneous layer with $n = \sqrt{1.49} = 1.22$ and $d = 112$ nm causes total transmission for $\lambda = 550$ nm. Since no vaporizable material exhibits $n = 1.22$, the spectra of a MgF_2-layer ($d = 100$ nm) on PMMA is plotted for comparison. MgF_2 has $n(\lambda = 550 \text{ nm}) = 1.38$ and a transmittance increase of 2% is feasible, which is roughly the half of the theoretical possible.

The use of gradient layers allows for a broader AR-effect. The gradient of a quintic polynomial and the gradient calculated for the filling factor of a periodic 2D-array of Gaussian pins corresponding to the surface topography demonstrate that the peak performance lowers a bit as the bandwidth increases. The former has a geometrical thickness of $d = 195$ nm and the latter is about $d = 125$ nm thick. This agrees with observations by Macleod, who mentioned in his book [3], that graded index layers should be rather $\lambda_0/2$ in optical thickness for an AR effect around λ_0.

Several competing approaches to achieve a non-reflecting surface are known. Kurihara used the self-assembling of metallic nanoparticles as an etch mask to generate dies for injection molding of transparent thermoplastics and achieved a decrease in R of about 3% [58]. Anodization of metals is also familiar to produce dye-surfaces with stochastic SWS. A similar decrease on glass substrates was achieved by direct coating of self-assembled colloidal nanoparticles out of polystyrene spheres (diameter 105 nm) [59]. Using multilayer coatings, the transmittance within a limited bandwidth can be more increased [60, 61].

2.3 Reverse engineering from optical spectra

The reverse engineering from spectral data describes now the task of determining the materials properties $n(z)$, $\kappa(z)$ and d from the optical spectra Υ. For such an inverse problem a solitary solution exists just for a non-absorbing homogeneous freestanding single layer[1]. The numerical calculation of the more complex cases, especially the refractive index profiles from the stochastic SWS, lead to a multiplicity of solutions [29, 30] and require optimization techniques. Generally, the merit function:

$$\mathsf{MF} = \sqrt{\frac{\sum_{j=1}^{J}\left[(\Upsilon_{\mathsf{target}\ j} - \Upsilon_{\mathsf{calculated}\ j})^2\right] \times \mathsf{weight}_j^2}{\sum_{j=1}^{J}\mathsf{weight}_j^2}} \quad , \tag{2.12}$$

is introduced to describe the difference between the measured spectra ("target") and the calculated one(s) under variation of its (their) parameters. The weighting factors can be used to force the consideration of certain spectral ranges prior to others. Depending on the optimization algorithm the global or the local minimum of MF causes the stopping. Because this is a strictly mathematical progress, it is necessary to constrain the parameters to keep "non-physical" solutions out of it. This means that a calculated minimum for MF may be also reached for instance for unusual thicknesses or inconsistent refractive indices.

The chances of success for local search algorithms increase with well-chosen starting conditions. Generally, the closer the starting system is to the solution, the more likely the convergence. In the case of SWS a nonlinear refractive index gradient is estimated and possible start may be a linear profile in the value range of the pure materials PMMA and air. Parameters for starting systems can be gathered from investigations of topography. AFM and SEM reveal information to estimate the thickness of the gradient layer, and the considerations of the volume filling factors lead to assumptions of the shape of the refractive index profile (cp. sec. 4.4). This knowledge is used in the reverse engineering task of the *ex situ* spectra to decrease the number of possible solutions.

An alternative approach to improve the optimization process is to increase the number of spectral measurements. This can be done *ex situ* for different angles of light's incidence and polarization state or *in situ* by recording spectra during the whole fabrication process. In the latter case the small deviation of the spectra within short durations is advantageous for the convergence of the optimization algorithm.

Up to now, such systems detect only the transmittance data, because of the complex implementation of the substrate's motion and calibration. This restriction makes it impossible to assign uniquely a change in T to a variation of reflectance, scattering or absorption. Thus the reverse calculation should be avoided in spectral regions, where the substrate is absorptive and should be stopped, if scattering affects the transmission adversely. In the beginning the *a priori* knowledge from *ex situ* analytics of former experiments is urgent for evaluation. Later on the re-engineering can be done without this specific information and is ready for fast algorithms in rapid prototyping processes.

The reverse engineering strategy from *in situ* spectra differs from that of thin-films or layer stacks, where the change in the optical spectra is solely caused by the material that has been deposited since

---

[1] The above mentioned n-profiles lead to equations with cylindric functions that cannot be transformed for it.

the previous measurement [62]. Due to the plasma treatment material is etched at every surface point with a different speed and modifies the whole filling factor profile [63]. Consequently, the whole refractive index gradient has to be re-calculated, and as the pins are forming the thickness changes for each spectrum.

The most applicative profit of an *in situ* monitoring system is the ability to control the fabrication process. In the case of the plasma-ion etching for antireflective surfaces the stopping condition is given by the time of maximum transmittance.

2.4 Rigorous calculation of spectral properties

It is necessary to use rigorous methods for the direct calculation of light interaction with structures in the scale of the wavelength. The most popular approaches are Finite Difference Time Domain method (FDTD), Rigorous Coupled Wave Analysis (RCWA), and Finite Element Method (FEM). These computational-based algorithms usually model the object by discretization of a space domain in terms of gratings prior to solving the Maxwell Equations at each lattice site. The splitting and the periodic recombination are not advantageous for modeling the optical response of stochastic aligned pins or continuous profiles. FEM can compass this disadvantage by an adaptive triangular filling of unit cells.

Ehret [64] simulated diffraction spectra of the SWS on PMMA surfaces by one-dimensional FEM under assumption of a fixed height of 350 nm and a Gaussian variable distance of individual features of 200 nm $\pm$ 120 nm for a period of 5 μm. A good agreement was revealed for $\lambda = 546$ nm. Finally, for heights beyond 300 nm ($d_{opt} \approx \lambda/2$) no further decrease in reflection was predicted by FEM.

This thesis uses RCWA, which is also known as Fourier Modal Method (FMM), to model the optical response of a plasma treated surface. It is used to provide an insight into the dependencies of main shape parameters on the total antireflection performance of the arrangement. The used software package Unigit [65] embeds the RCWA into an interference matrix scheme which allows for a slicing of continuous pin shapes into stair case profiles and a sequenced calculation.

Since RCWA is a numerical method, the efforts in computation increase with accuracy. The complexity rises due to the number of Rayleigh (diffraction) orders that should be kept during calculation. The consideration of an infinite number of orders would lead to the exact result, but as the numerical solution converges[2] as the number of kept Rayleigh orders increases, the algorithm can be truncated at the accomplishment of a certain precision. Individual truncation test runs have been done to estimate the number of Rayleigh orders that are necessary to achieve an accuracy equal to that of the spectral measurement. Depending on the shape this number is typically lower than 12 for the 2D-grating calculations of the all-dielectric structures having an aspect ratio smaller than 4.

---

[2] The convergence depends mainly on material properties and aspect ratio of the structure.

3 Interaction of plasmas with polymers

In order to describe the formation of antireflective SWS by plasma etching, it is urgent to understand the ways of interaction between the plasma and the polymer at the surface. Firstly, the main properties of plasma have to be clarified, which are responsible for the interaction. Secondly, the essential polymer properties are evaluated and quantified that are affected by the plasma. With the knowledge of both, the discussion of plasma polymer interaction, divided into photon's and particle's fraction, is promising. Thirdly, models are introduced that describe self-organized structure formation on surfaces in the presence of plasmas and plasma-like environments.

3.1 Properties of plasmas

Plasma is defined as (partly) ionized gas. In contrast to an ion beam, the plasma cloud is electrically neutral with respect to its ambient. The degree of ionization specifies the fraction of gaseous matter that exists in the ionized state. For charge separation, energy is necessary and must be supplied permanently for the conservation of the plasma state, since fast recombination processes in the volume and charge neutralization at conductive chamber walls are always present. The degree of ionization is defined as the ratio of the density of the ions N_{ions} to the overall particle density:

$$\alpha_i = \frac{N_{\text{ions}}}{N_{\text{ions}} + N_{\text{neutrals}}} \quad . \tag{3.1}$$

Because of their low melting or softening points around 100 °C, polymeric substrates can be exposed only to a small thermal load. This is given by low-pressure plasmas, which exhibit pressures lower than a few Pascals and are typically not in a thermal equilibrium state [66]. The electrons' temperature is several orders of magnitude higher than that of the ions. The low ion energy causes only small propagation ranges and a low subsurface damage when hitting the surface of the polymer [67]. Under such conditions α_i is typically in the range of 10^{-6} – 10^{-2} and some conclusions from ideal gas model are still valid.

The ionization process can be forced thermally (e.g., focused laser beam, exothermic reactions), by electric fields (e.g., dc-discharge, ac-discharge (RF) 13.56 MHz, microwaves (MW) 2.45 GHz) or by electron/ion impact. The latter leads in combination with strong electromagnetic fields to collision cascades. A review of plasma sources that are applied in industrial surface modification processes was given by Anders [68].

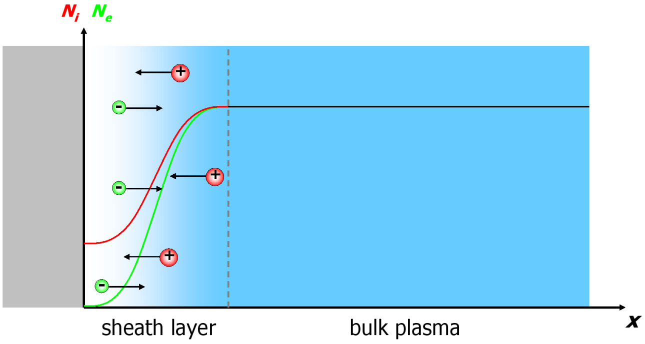

Fig. 3.1: *Formation of a plasma sheath and gradients of electron density* N_e *and ion density* N_i*.*

Due to their high mobility, electrons leave the plasma at the recipient's grounded walls and cause the generation of a sheath layer that counteracts further electron loss, see Fig. 3.1, due to an electrical potential, which is called plasma potential. The transport of ions and electrons to the surface through the sheath is mediated by ambipolar diffusion and is controlled by the Bohm sheath criterion [69], which states that only ions (ionic mass m_i) and with velocities v higher than the critical velocity:

$$v_c = \sqrt{\frac{k_B T_e}{m_i}} \quad , \tag{3.2}$$

will reach the surface. Here T_e is introduced as the electron's temperature. The Bohm criterion leads to an ion flux into the sheath layer of:

$$J = 0.6 N_0 v_c = 0.6 N_0 \sqrt{\frac{k_B T_e}{m_i}} \quad . \tag{3.3}$$

T_e may be derived from plasma potential given by:

$$U_P = \frac{k_B T_e}{2e} \ln \left(\frac{m_i}{2.3 m_e} \right)^{1/2} \quad . \tag{3.4}$$

The Debye length λ_D, which defines the distance over that significant charge separation can occur, may approximate the thickness of the sheath layer:

$$\lambda_D = \sqrt{\frac{\epsilon_0 k_B T_e}{N_e e^2}} \quad , \tag{3.5}$$

where N_e is the density of the electrons and can be roughly estimated by $N_e = \alpha_i N_0$. An additional potential can be generated in the plasma sheath region by setting the plasma parameters. The so-called bias-potential U_B allows for higher ion energies. To sum up the main plasma properties, the plasma potential is a function of the electron temperature, whereas the ion flux depends on the plasma density.

3.2 Essential polymer properties

To learn more about the growth of the features on PMMA surfaces, it is helpful to compare the results with other similar materials. Furthermore, the need of antireflective surfaces exists independent from the substrate material. Tab. 3.1 summarizes the polymer's properties, which may have an impact on the plasma etch process, for the following materials: [1]

- Polymethylmethacrylate (PMMA), Plexiglas 7N, Rhöm-Degussa Evonik Industries [70]

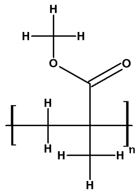

- Polycarbonate (PC), Makrolon LQ2647, Bayer MaterialScience [71]

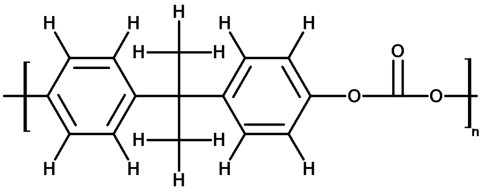

- Polyethylentherephthalate (PET), Tetoron OX50, DuPont Teijin Films [72]

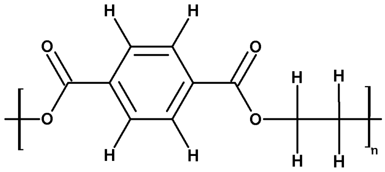

- Polyamide (PA), Trogamid CX 7323, High Performance Polymers Degussa AG, Evonik Industries [73].

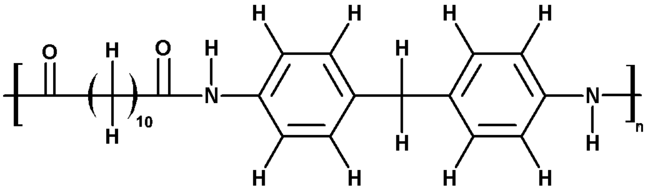

Based on their stoichiometry, the polymers have different compositions of the constituent atoms. Important to note is the high oxygen content of PMMA and PET that is close to 1/3 in mass, while PC has 1/5 and PA has less than 10%. The opposite holds for the carbon mass fraction, which is above 75% for PC and PA. Often additives are mixed in the polymer to protect the grade against

---

[1] This thesis does not pay attention to the mechanical properties, like elastic moduli or rheology, and the chemical resistance to solvents.

environmental impacts or to improve the heat resistance and the processing. In the case of PC a stabilizer against UV-degradation is added resulting in an uncertainty of the composition. To enhance the processing (winding, handling) with foil material, almost every PET film has added so-called slip agents. For Teteron the one-side acrylic coating is of a thickness that does not affect the optical properties in the visible spectral region. Structuring was done at the opposite side.

Additionally, the mass percentages may shift due to the amount of water that can be absorbed from humidity. Working under high-vacuum conditions, most of the water evaporates from the surface near region prior to the plasma-treatment.

Generally, thermoplastics tend to be amorphous. PA and PET form micro-crystallites that enable a better resistance against mechanical and chemical impacts, as well as high melting (processing) temperatures. The crystallinity of typical PET films is about 50% [74]. The substrates were fabricated by injection molding that causes a slight preferred orientation of the polymer chains. The biaxial orientated structure of the PET film is a result of fabrication process using an extruder.

Seven different kinds of chemical bondings exist for the mentioned polymers. PMMA is aliphatic, missing any ring structures. PC, PET, and PA exhibit one or two benzene rings (or phenyl groups) per monomer and thus belong to the aromatics. The stability of the bondings of benzene is very high due to the delocalized electrons of the alternating double and single bonds. This is known as a chemically conjugated system and affects the neighbor atoms within the polymer chain, too. Consequently, the energy that is necessary for full decomposition of a monomer is higher for the polymers with aromatic groups (PC, PET, PA) than for aliphatic monomers (PMMA), even if scaled to the number of participated atoms. It is advantageous for the decomposition of PET that an acrylic structure is next to the phenyl ring in the backbone.

The thermal properties are of interest, because the main energy transfer of the impinging particles attributes to heating up, and local melting may be a reason for the generation and growth of the surface structures. A model that takes the temperature-dependent surface diffusion into consideration for self-organized growth is discussed in section 3.3.3.

At the glass transition point, which is rather a temperature range, the material exhibits the maximum change of elasticity and viscosity. The kinetic theory defines the glass transition temperature T_g as the temperature at which the relaxation time for the segmental motions in the polymer chain is of the same order of magnitude as the time scale of the experiment [75]. Thus T_g is related with the degree of cross-linkage. The glass transition zone of the semi-crystalline polymers is higher than that of their amorphous companions. A similar standardized quantum for the resistance against thermal load is given by heat deflection tests (DIN EN ISO 75-1) or the Vicat-Method (DIN EN ISO 306). The softening temperature for the latter method states for a technique, which measures the deformation with increasing temperature under load of a pyramidal probe. During plasma treatment the samples are not exposed to an external load, but intrinsic stress caused by the fabrication process (molding, extrusion) may have the same effect of lowering the softening temperature.

Tab. 3.1: *Chemical properties of the tested polymers (manufacturer's data).*

	PMMA	**PC**	**PET**	**PA**
CHEMICAL STRUCTURE	$C_5H_8O_2$ amorphous	$C_{16}H_{14}O_3$ amorphous	$C_{10}H_{18}O_4$ biaxial orientated	$C_{25}H_{32}O_2N_2$ semi-crystalline
Specific gravity g/cm^3	1.19	1.2	1.4	1.02
Composition mass%				
H	8.0	5.5	8.9	8.2
C	60.0	75.6	59.4	76.5
O	32.0	18.9	31.7	8.2
N	–	–	–	7.1
# of bonds & energy (eV)				
C-H (7.42)	8	14	8	30
C-C (3.98)	4	10	6	19
C-O (5.77)	2	4	4	–
C=O (14.3)	1	1	2	2
C=C (10.0)	–	6	3	6
C-N (5.1)	–	–	–	4
H-N (8.4)	–	–	–	2
total bonding energy eV per monomer / atom	101 / 6.7	241 / 6.9	165 / 7.2	424 / 7.0
water absorption % (50% rh)	0.1 – 0.5	0.12	0.7	2.0
THERMAL PROPERTIES				
Glass transition T °C	110	145	70 – 80	140
Vicat softening T °C	103	143	170	130
Long term service T °C	91	129	105	100
Specific heat capacity kJ/kg/K	2.44	1.70	1.2 – 1.35	2.49
Thermal conductivity W/m/K	0.18	0.17	0.13 – 0.15	0.25
Viscosity number cm^3/g	53	56	65	160 – 180
ELECTRICAL PROPERTIES				
Volume resistivity Ωm	10^{13}	10^{14}	$7 \cdot 10^{15}$	10^{15}
Surface resistivity Ω	10^{13}	10^{16}	$6 \cdot 10^{17}$	10^{15}
Dielectric strength kV/mm	30	33	17	27
OPTICAL PROPERTIES				
transmittance (550 nm)	92.1%	89.2%	87.6%	91.3%
transmittance range nm	350 – 1600	430 – 1600	370 – 2700	390 – 1600
refractive index (550 nm)	1.49	1.59	1.64	1.52
extinction coefficient (550 nm)	$< 5 \cdot 10^{-4}$	$< 5 \cdot 10^{-4}$	$< 5 \cdot 10^{-4}$	$< 5 \cdot 10^{-4}$

The plasma provides a huge amount of charge carriers, and dielectric properties become important. The generation and the properties of the plasma sheath depend strongly on the electrical conductivity of the wall. The polymers are known as good insulators that have very high dielectric breakdown voltages (dielectric strength) and creepage barriers. The high surface resistance of more than $10^{13}\ \Omega$ obstructs charge transfers and thereby supports the generation of permanent electric charge polarization at the surface, which can be used for electret applications. In the case of PMMA the dipole moment is associated with the ester group $COOCH_3$ and its orientation in the electric field during formation [76]. Electrostatic microdischarges on the surface have revealed and fractal character [77]. In addition, water content in the surface region and temperature affect the performance and lead to charge equalization processes when increased. Electret properties are also well known for the PET [78], PC [79] and Nylon [80].

A change in space charge dynamics of PMMA was obtained under electron beam irradiation [81]. It was found that the distribution range of the space-charge increases with increasing beam energy. Moreover the range increases mainly within the first 20 s of treatment and attains a saturated value of about $0.3 \cdot 10^9$ eV/m. This implies a typical charge-distribution of about 70 nm for electrons that have energies related to the plasma potential (≈ 20 eV). This effect is understand as a radiation-induced conductivity, whose value can be several orders of magnitude greater than that of the original conductivity [82]. It is combined with a charge transfer into the subsurface region forced by the electric field of the space-charge and the temperature increase in the irradiated region [83].

From optical point of view the tested materials have their high transmission range in the visible spectral region and are applicable with minor optical losses up to the near infrared. The short-wavelength limit is given by the resonances of electrons in the ultraviolet region (UV). An UV-blocker was added to the polycarbonate to prevent photo-degradation and thus the absorption edge is apparent at $\lambda = 400$ nm. The highest refractive index n is specified for PET (1.64) and the lowest one for PMMA (1.49). The long-wavelength border, caused by higher-order resonances of molecule vibrations, is in the near infrared region (NIR). Beyond $\lambda = 1600$ nm the first harmonic of CH_2/CH_3 vibration appear. Higher order and combination bands of low absorption are registered around 1400 nm (combination), 1100 nm (2^{nd}) and 900 nm (3^{rd}) [84]. As the extinction coefficient κ is negligible, the fresnel reflection is governed mainly by the n, which implies the highest R for the PET followed by PC, PA, and PMMA. Nevertheless, for a proper reverse engineering $n(\lambda)$ and $\kappa(\lambda)$ of the used materials were determined by spectro-photometry of the untreated substrates by the use of (2.10) and the Beer-Lambert law. The dispersion plots will be given in Fig. 5.29 in the results section for the wavelength range of interest.

Tab. 3.2: *Typical interactions of species from plasma with a polymer (surface) [87].*

Species	**Energy**	**Interaction range**	**Characteristics of interaction**
electrons	1 eV – 10 eV	1 nm	dissociation, ionization, heating
ions	< 10 eV	monolayer	chemical reactions, functionalization
ions, fast neutrals	> 60 eV	2 nm – 5 nm	sputtering, etching, chain scission, ion implantation
excited neutrals	< 10 eV	monolayer	chemical reactions, functionalization, cross-linking
photons	< 3 eV	$\approx$ μm	energy transfer / heating
photons	> 3 eV	10 nm – 50 nm	chemical reactions, chain scission, cross-linking

3.3 Plasma treatment of polymer surfaces

3.3.1 Impact of plasma particles

Many publications exist that investigate the interaction of plasma particles with polymer surfaces, especially for PMMA. These works are mainly attributed to the behavior as photo-resist material (photochemistry, cross-linking, etching), polymerization (functionalization, chemical reactions), specific surface treatments (functionalization, chain scission, cross-linking) [85] and cleaning. In general, the decomposition is distinguished between depolymerization and chain scission. The former describes the separation of a whole monomer molecule from the backbone, whereas chain scission is a dissociation into undefined fragments [86].

Polymers for optical components are typically built of elements with low atomic masses such as H, C, N, O that are connected via covalent bonds in (branched) chains. The plasma polymer interaction is dominated by two competitive reactions namely modification and degradation. Their effect on the surface region differs strongly, whereas charged particles show smaller penetration depths due to the additional Coulomb interaction than neutrals of the same kinetic energy. If modification dominates, the polymer's properties will change due to polymerization. The typical ablation process in plasma is etching. The effect of photons which are emitted from the plasma cannot be avoided in this configuration and is discussed in 3.3.2. Their penetration depth bases on the frequency-dependent absorption. The molecular structure of the polymer and the plasma properties (pressure, kind of excitation, gas species) decide which of the interactions dominates the plasma treatment. Table 3.2 summarizes these effects.

If low-energetic ions exist, like in most RF and MW plasmas, the chemical (isotropic) etching dominates and the effect of physical (anisotropic) etching is reduced. Contrary, the impact of physical etching due to sputtering increases for high-energetic ions, like ion beams or plasmas with high acceleration potentials [88]. The effect of an additional acceleration potential on the increase in etch rate of PMMA due to high-energetic ions was demonstrated in [89].

The process of chemical erosion can be separated into the following main steps: (I) generation of the reactive species, (II) arrival of the reactive particles at the surface to be etched, (III) adsorption of the species at the surface, (IV) forming a chemical bond between surface atoms and the reactive particles (chemisorption), (V) generation of product molecules, (VI) desorption of the product molecules, (VII) removal of the reaction products from the reaction sites. The chemical etch rate of the polymer is limited by the slowest process of the steps (I) - (VI), but all steps are influenced by ion bombardment, for example in increasing the number of reactive particles ($\rightarrow$ I), forming open bonds at the surface ($\rightarrow$ III), supporting energy to form covalent bonds ($\rightarrow$ IV).

Since inert gas plasmas have only a negligible fraction of reactive species, that arise from the residual gas or plasma-induced dissociation processes at the substrates themselves[2], the chemical modifications at the surface are caused by the energy absorption due to impacts. In particular, the noble gas ions (He, Ne, Ar, Xe) do not lead to an integration of new functional groups, but can enable the recombination of broken polymer chains and the formation of new structures (cross linking). The ablation due to sputtering depends on the cross-section area during impact and is small, if the mass of the impinging ions differs strongly from that of the polymer constituents. Radicals are neutrals and have typically a low kinetic energy, because they are not amenable to the Coulomb forces. This leads to a short impact cascade in the solid and reactions near to the surface. Moreover, they are able to break directly the covalent bondings of the polymer. Atoms of typical reactive gases exhibit a higher electronegativity value O (3.5), N (3.0) and F (4.0) than the polymer constituents C (2.5) and H (2.2). In the case of an oxygen plasma, an exchange of C-C and C-H bondings by oxygen-containing groups such as $-C{=}O$ (carbonyl-), $-COOH$ (carboxyl) and $-OH$ (hydroxyl) is forced [90], whereas nitrogen as reactive gas induces $-NH_2$, $=NH$ (amine), $-NO_2$, NO (nitro) or $-C{\equiv}N$ (nitrile) groups.

Several works on plasma treatment of PMMA indicate a rapid decomposition of the (methyl ester) side chain in combination with cross-linking. The effect was proved by x-ray photo-electron spectroscopy (XPS) and infrared absorption spectroscopy[3] for Ar/H_2O DC glow discharges [91], O_2/H_2O RF plasma [92], Ar/H_2O RF plasma [93, 94], and Ar/O_2 ECR-MW plasma [95]. The latter author suggests a two-step degradation process for the side chain starting at the higher polarity bonding $C{=}O$, mainly induced by low energy ions ($<$10 eV) [96]. The saturation of the open bonding by reactive species may lead to a polypropylene-like polymer. The strong ester decomposition is in competition to the oxygen incorporation during the plasma treatment. It depends on the ion current which of the processes dominates. Mostly, an increase in the C–C and the C–H fractions to the

---

[2] chamber walls are assumed to be inert

[3] Surface sensitive measurements are achieved in attenuated total reflection (ATR) or reflectance-absorption (IRRAS) configuration that uses grazing incidence of p-polarized light.

benefit of a loss in C–O and O–C=O bondings was demonstrated. The tendency toward rapid degradation makes PMMA a favorable material in ion beam lithography [97]. Kaless confirmed the decomposition mechanism for the given APS-plasma process by XPS and IR analysis [18, 98].

The AFM and XPS analysis of Ar/N_2 plasma treated copolymer-PMMA films [99] revealed a smoothing of the surface from 5 nm (rms) to 1.5 nm (rms) and a modification of the copolymer's structure with argon content. The argon ions induce the deepest morphological redistribution of the polymeric chains, while the chemical reactivity of the molecular species becomes dominant with introduction of N_2.

The conductance of PMMA increased after bombardment of argon ions having an energy of 250 eV – 1250 eV [100]. This effect was attributed to graphitization processes in the subsurface layer [101]. As the penetration depth roughly approximates the thickness, a substantial increase in conductance with ion energy was observed. It was pointed out earlier [102, 103] that high-conducting clusters are developing in ion-bombarded materials. The obtained cluster size and their distance is about 1 nm.

It was found for CF_4/O_2 plasma treatment of Makrolon (PC), that the phenyl ring structure degrades faster with increasing oxygen content and the etch rate rises [104]. An oxygen-rich surface region was also observed.

Gröning *et al.* demonstrated for PET always an increase in oxygen content in the surface near region due to reactive gas plasmas [95], emphasizing a less intense decomposition of the analogous ester structure in the PET-chain as a reason. For PET the ester groups are bonded to the phenyl ring. This direct neighborhood disturbs the decomposition, because the high polarizability of the ring structure attracts ions rather than the surrounding atoms, and its comparable big size increases the probability for collision of impinging ions. The effects of aromatic groups in polymer chains were investigated by comparing three polyester materials, amongst them PET, with different fraction of phenyl groups [105]. The etch rate decreases in oxygen-rich RF plasmas as the fraction of phenyl groups increases in the polymer, which was attributed to a higher efficiency in cross-linking that impedes degradation.

The plasma treatment of polyamides often concerns various types of nylon. Aromatic polyamide was investigated by Inagaki [106, 107] who treated Poly(p-phenylene terephthalamide) (PPTA, $C_{14}H_{10}N_2O_2$) with an oxygen RF plasma. An increase in rms-roughness from 1.4 nm to 12.5 nm and lateral sizes of less than 100 nm were observed. Moreover oxygen functionalities (C–O, C=O) were formed at the surface.

The interaction of the plasma's electrons with the polymer surface happens in several different ways. The most prominent are emission of electromagnetic radiation (bremsstrahlung) and elastic or inelastic collisions. The first mechanism is dominant for e^- between 10 MeV and 100 MeV [108]. Below the most electrons are stopped by inelastic collision causing excited target atoms, secondary electron formation, or ionization. Beside also deflection by the coulomb field of nuclei occurs, which is the favored mechanism for low energy electrons, which is given for the current process, and for high atomic number materials.

The glass transition temperature T_g plays an important role in polymer etching [109]. Above T_g, a strong increase in the etch rate was identified for oxygen containing plasmas. This effect was related to the heat capacity changes that follow for $T > T_g$ and to the competition between the plasma-induced scission and cross-linking processes. Above the T_g the ion-induced etching becomes temperature dependent. A detrimental effect of a substrate temperature close to T_g is a permanent deformation, that can lead to the destruction of optical properties.

Sputtering is defined as the removal of near-surface atoms from a target. If an impinging particle transfers during its cascade energy to a target atom greater than the surface binding energy of that target, the atom may be sputtered. In detail, the target atom's energy normal to the surface has to be above the surface binding energy, when it crosses the surface plane. So only the cascades, which reach back to the target surface, are important to sputtering. The collision cascade ends, when the energy of the impinging ion drops below the lowest displacement energy of any target atom and the energy is transferred into phonons (vibrational energy, heat-up) or ionization. To quantify, the sputtering yield Φ_S is introduced as the mean number of sputtered target atoms per incident ion:

$$\Phi_S = \frac{\#\ \text{sputtered atoms}}{\#\ \text{incident ions}} \quad . \tag{3.6}$$

Φ_S depends on ion current density, ion energy, angle of ion incidence (effective momentum transfer) and the surface binding energy. Because the polymeric substrates are compounds, the sputter process is specific to each constituent, implying separate sputtering yields for each element. Apart from the latter the sputter-removal at low kinetic energies is practically non-selective. For real surfaces, the surface binding energy changes under bombardment due to surface roughness, and due to surface stoichiometry in the case of compounds.

It is generally excepted that small-molecule degradation products are constantly removed by sputtering or evaporation from the surface, while polymeric scission products remain intermeshed with the unaffected polymer or with cross-linked networks [110]. Gokan [111] stated, that if carbon has the smallest Φ_S then sputtering of carbon is the etch rate limiting step, implying an inverse proportionality between these quantities. He suggested a dependency of the overall ablation rate Φ on the total number of atoms per monomer Γ, the number of carbon and oxygen atoms Γ_C and Γ_O, respectively:

$$\Phi \propto \frac{\Gamma}{\Gamma_\text{C} - \Gamma_\text{O}} \quad . \tag{3.7}$$

With the data of Tab. 3.1 this gives 5.3 (PET), 5.0 (PMMA), 2.7 (PA) and 2.5 (PC). In coherence, mass spectroscopy of the volatile etch products revealed CO^+ and H_2^+ as the most prominent molecules followed by smaller counts of H_2O^+ and C^+ during plasma treatment of PMMA [111]. A linear weight loss with time was revealed for many polymer grades under treatment of atomic oxygen at 133 Pa [112] and a He discharge at 13 Pa [21]. This implies a constant etch rate which was

Tab. 3.3: *Bonding enthalpies and wavelengths of absorbed radiation.*

Bond	**Bond enthalpy** / **kJ·mol^{-1}**	**Bond enthalpy** / **eV**	**Radiation wavelength / nm**
C-H	413	4.28	290
C-C	348	3.61	343
C-O	358	3.71	334
C=O	745	7.72	161
C=C	614	6.36	195
C-N	305	3.16	392
H-N	391	4.05	306

specified for PMMA and PC under this conditions with 8.8 nm/s and 10.7 nm/s, respectively. PET showed an ablation of 0.2 nm/s for a oxygen plasma jet treatment [113].

Furthermore, very high energetic ions (keV range) are often used to implant ions in the surface or subsurface region in order to change material properties like electrical conductivity [114, 115] or refractive index for wave guiding [116, 117].

3.3.2 Impact of photons

Electromagnetic radiation emitted from a plasma depends on the excitation, the discharge power, the pressure, and the type of gas. Beside, thermal radiation is expected from the plasma-heated chamber and the plasma source. However, the high-energy radiation in the UV and vacuum UV (VUV) range from recombination and bremsstrahlung plays the essential role for polymer degradation. Many works describe the interaction with light from UV lamps or lasers against the background of resist development for lithography. These light sources have usually a more narrow spectral bandwidth compared to a plasma emission. Thus, plasma is less selective in photochemistry than the UV lamp treatment does.

If the photon energy $E = hc/\lambda$ reaches the energy of the covalent bonds, photochemical reactions are possible. For a direct photon-induced scission of the bond, the photon needs to be absorbed by resonance. The enthalpies and the related wavelengths for common polymeric bonds are summarized in table 3.3. The value for the bond enthalpy is rather a range than a fix value, since the neighboring atoms affect also the bond strength. Photon energies above 3.5 eV can lead to photochemical reactions. For PA the C-N bonds absorb already around 392 nm (3.2 eV) [4].

The absorption of photons is a statistical process. The penetration depth can be estimated by the use of the Beer-Lambert law that describes the decrease in intensity I with propagation z in an

---

[4] Often nitrogen containing polymers (amides) are added to UV-unstable polymers having the function of a radiation blocker.

absorbing media:

$$I(z) = I_0 e^{-\alpha z} \qquad \alpha = \frac{4\pi\kappa(\lambda)}{\lambda}. \tag{3.8}$$

The absorption coefficient is proportional to the specific extinction coefficient and inverse proportional to the wavelength of radiation. The penetration depth d_p is defined as propagation length at which the $I(d_p)$ drops a certain fraction of the initial intensity I_0. Common conventions are $d_p = \alpha^{-1}\ln 2 \approx 0.69 \cdot \alpha^{-1}$ for $I(d_p)/I_0 = 0.5$ or $d_p = \alpha^{-1}\ln 10 \approx 2.3 \cdot \alpha^{-1}$ for $I(d_p)/I_0 = 0.1$.

As noted by Holländer *et al.* [118], who investigated the degradation of polyethylene (PE) and polypropylene by radiation from plasma sources, polymeric materials have very high extinction coefficients for wavelengths below 180 nm and thus exhibit penetration ranges less than 100 nm. As found out earlier from hydrogen glow discharges, the main degradation processes for PE was cross linking [119]. PMMA shows a higher etch rate than polypropylene and polystyrene under UV radiation [120].

In the presence of oxygen occurs photo-oxidative degradation. The generation of polymeric radicals leads to chain scission [121] that can cause an increase in etch rate [122, 123]. For the exposure of PMMA to high-power radiation, it was figured out that the degradation starts with a scission of the ester side chain [124, 125]. The increase in ablation rate in the presence of oxygen is attributed to further photo-oxidation [126]. Photons with an energy < 8.5 eV ($\lambda > 145$ nm) influence the bondings of the side chain, while photons of higher energy affect the backbone bondings and are able to ionize the target atoms. Thus enhanced reaction mechanisms introduce new ways of degradation. A decomposition of the side chain of PMMA by UV photons of wavelengths down to 165 nm, which were emitted from the used APS plasma, was verified [127]. Radiation from a mercury lamp ($\lambda = 254$ nm) caused a distinct structure formation by different etch speeds within a two-phase compound of PMMA and PS (polystyrene) [128]. Ichihashi [129] used the cleavage of methylester groups and a decrease in molecular weight by UV radiation to increase the refractive index at the surface region in order to build waveguides. At same time he observed a decrease in T_g from 105°C to 80°C.

Polycarbonates are known to be difficult to stabilize under UV exposure. At wavelengths below 310 nm photo-induced chain scission leads to radicals that form hydrodiphenyl units followed by further conversions, whereas above 310 nm the photo-oxidation to hydroperoxides was verified as the dominating process [130, 131]. In polychromatic light, such as given by the plasma, both processes occur and the formation of hydrodiphenyl protects the PC from photo-oxidation, even if only temporarily. Moreover PC is known to deteriorate and yellow, if exposed to UV-A and UV-B radiation of sun light unless an oxidation-preventive additive is used [132].

UV light below a wavelength of 310 nm, where strong absorption occurs, causes a degradation under vacuum, nitrogen, and oxygen atmosphere [133]. The detection of terminating phenyl groups is an indication on chain scission. Even for wavelengths above 310 nm a deterioration was demonstrated under formation of carboxyl groups as long as no UV-blocker is used [134]. Due to the phenyl group the cleaved polymer chains of PET cross-link quickly [135].

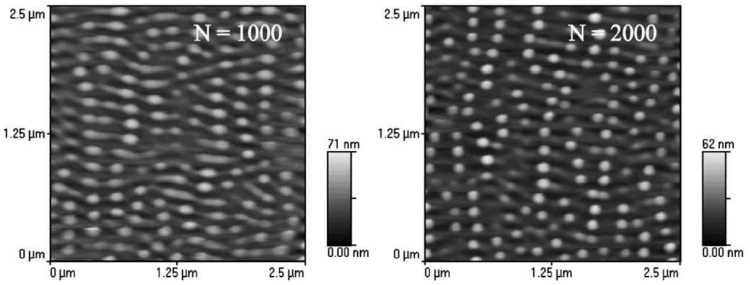

Fig. 3.2: *AFM images of LIPSS formed on a PC surface by ArF laser treatment ($\lambda = 193$ nm) for N pulses [138].*

The polychromatic emission from plasma differs strongly from the monochromatic laser light. Nevertheless, the main results of interaction with laser radiation are outlined. Comparisons of treatments with polychromatic incoherent light sources (Hg lamp) and excimer lasers (ArF, 193 nm) showed, in general, that the former causes mainly a formation of functional groups and low etch rates, whereas the latter leads to a ablative photo-decomposition at higher rates, but a negligible reaction with the surrounding atmosphere [136]. It was pointed out that the laser irradiation is more effective on surface morphology than in chemical decomposition. To achieve a significant etch rate a specific laser intensity fluence threshold is necessary, which is about 10 mJ/cm^2 for PMMA. A detailed discussion of ablation mechanisms is given for various UV wavelengths in [137].

The high degree of coherence of laser light causes an effect that is known in literature as "Laser-induced periodic surface structures" (LIPSS). The occurrence of periodic parallel fringes, see Fig. 3.2 with the distance in the order of magnitude of λ has been attributed to high energy deposition and melting for interfering partial waves [139]. Moreover, the spacing between the fringes depends on the angle of incidence and polarization of the damaging beam. It is assumed that surface roughness, confined to a region of height much less than the wavelength of light, is responsible for the inhomogeneous deposition of energy. For s-polarized light the LIPSS is independent on the roughness properties, whereas it correlates with shape and filling factors for p-polarization. This effect was demonstrated for numerous laser sources and target materials [140], as well as for polymers like PET [141, 142] and PC [138]. A review is given in [143].

3.3.3 Mechanisms of roughening and patterning

This section shows models that describe the origin and/or the formation of the SWS by means of erosion, since the macroscopic (global) temperature during the process is expected to be to low for a structure formation by melting. Nevertheless, the temperature is still present in thermodynamic processes like surface diffusion.

The impact of photons on the feature size is not regarded here since their patterning effect by interference would lead to a time-stable size correlated with the wavelength. This does not match to

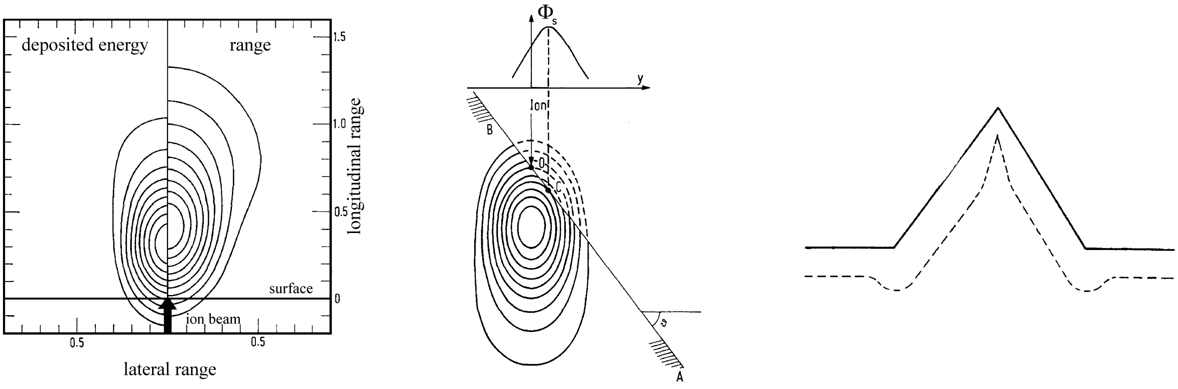

Fig. 3.3: *Normalized penetration and energy deposition depth (left), laterally shift of energy deposition for a tilted surface plane (middle), and effect on a localized surface feature (right) [34].*

the observation of pin formation. Even more the irradiation is more homogeneous than that of the charge-influenced ions and electrons, and a patterning by absorption has to be forced by material inhomogeneities that could not be detected.

A first mechanism of surface roughening by ion bombardment was given by Sigmund [34], who analyzed numerically the spatial distribution of sputter ablation. He showed that the roughness of a substrate increases under bombardment due to the angle-of-incidence-dependent sputter erosion that causes locally different ablation rates. The reason was found in the energy deposition of the entering ions within the subsurface region. Fig 3.3 (left) shows the contour plots of ion range and the deposited energy (statistical average) calculated for equal masses of bombarding ions and target atoms. The isodose lines of equal energy amount are Gaussian with respect to penetration depth and lateral deviation. When the surface plane is now tilted as in Fig 3.3 (middle), implying an oblique angle of incidence at point O, the point of the highest deposited energy shifts lower along the surface plane. Now the highest sputter yield Φ_S is not at the point of ion incidence, but next to it. Fig 3.3 (right) demonstrates what happens to a ridge (1D) or cone (2D) during ion bombardment: the ablation Φ_S is locally dependent on energy storage E,

$$\Phi_S(y,y') \propto \int \mathrm{d}y' E(y,y') \propto \int \mathrm{d}y' \exp\left[-(h(y')-h(y))^2-(y'-y)^2\right] \quad . \tag{3.9}$$

Simplified expressions are given in [144]. The top region shows a smaller regression speed than at the flanks leading to an increase in feature height and sharpness. Or in other words, the Φ_S of a positive radius of curvature is greater than a flat surface and is smaller for a negative curvature. The formed structures are oriented in a way that they face the ion beam. Thus, the surface is always unstable during plasma bombardment, since natural surfaces exhibit always roughness, inhomogeneities, and ion beams have intensity fluctuations. The result is an ongoing growth in surface roughness.

The work of Bradley and Harper [16] was now to combine the roughening theory from Sigmund [34] with a mechanism for relaxation of a nearly plane surface to flatness by diffusion after Mullins [145]. They derived a theory for periodical structure formation on amorphous solids as observed in ion beam etching [146, 147]. The self-organized growth of ripples and pin structures on various semiconductor materials, graphite [148], SiO_2 [149], and metals (both [150]) is described successfully. The model predicts an orientation, a preferred spatial frequency Λ, and a growth at exponential rates for the features, depending sensitively on flux J_i, angle of ion's incidence, surface diffusivity D_S, concentration of mobile species at the surface C and substrate temperature T:

$$\Lambda \propto J_i^{-1/2}(k_B T)^{-1/2}(D_S C)^{1/2}. \tag{3.10}$$

Any chemical etch component for erosion is neglected, which has been also pointed out by the solely use of noble gas ions in the regarding experiments.

Cuerno [36] and Makeev [151] generalized this theory by including further high order effects of different physical origins. Moreover, non-thermal relaxation mechanisms were proposed for smoothing. Especially, ion-induced viscous relaxation $C \to C(J_i)$, which is mediated by the motion of defects and created by collision cascades, is promising [149]. Since the mechanism operates on scales of the order of the penetration depth, the modifications are limited in the nanometer range, which may at most be significant at the initial state. Thus, this process cannot solely explain the growth of the mesoscopic structure. This seems possible only in combination with chemical etching.

Reactive ion etching (RIE) combines the characteristic properties of the sputter plasma with those of plasma etching. For homogeneous materials the slowest process decides on the etch rate. For the erosion of compounds, the etching is selective to each constituent. Using a material with a strongly differing selectivity as a mask is very common for patterning [152]. The selectivity is defined as the ratio of the rates of the materials to be patterned and to be etched. It is a quantity for the anisotropy of the etching process. Because the pattering material protects a etch-able material below, it passivates the ion-bombarded region. If such a passivation shows inhomogeneities in its properties, such as composition or thickness, its etch rate varies along the surface or the mask effect may even break down. A detrimental damage of the underlying pattern material follows.

Transport by diffusion is the main cause for movements of the particles in surface region. For an ideal isotropic erosion process the reaction speed is the same in all directions [152]. This is quasi valid for every wet etching process. In presence of an etch mask, the material under the mask's rim is etched, too. This effect is known as "undercutting". As the horizontal and the perpendicular etch rate are equal, the isotropic etching techniques are not able to form features with arbitrary large aspect ratios (height:width ratio). Undercutting of the mask edges limits this ratio to 0.5. To fabricate aspect ratios > 1, practically only dry etching processes are applied.

Anisotropic etching can be caused either by the dependence of surface processes on the direction, or by a preferential motion of reactive particles in the gas (plasma) phase. The former is given in the so-called crystallographic etching and can be neglected since the polymers are amorphous and the observed pins are much larger than the typical size dimensions of the monomers. Thus, the anisotropic etching is caused by the preferential direction of particle flow towards the polymer

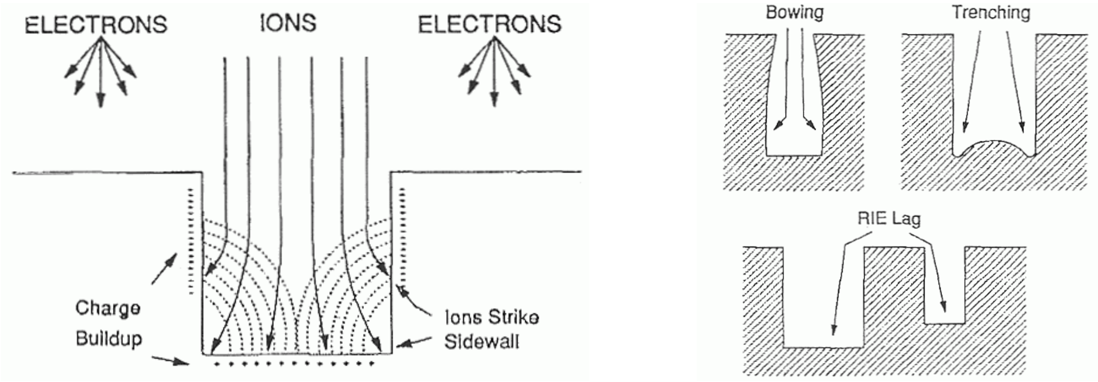

Fig. 3.4: *Cause and effect of local surface charging (left), and typical etching characteristics (right) [154].*

surface. In this context, the APS plasma is a representative of an ion (enhanced) etching technique.

The effective penetration depth increases for low-pressure plasmas where the number of collisions is small, the plasma sheath (λ_D) is large, and the ions imping practically normal onto the surface. Unfortunately, the absolute ion density is also lower. Increasing the pressure causes a shorten of the mean free path of the particles and the plasma sheath, the ions reach the surface in a broader distribution of directions and the degree of anisotropy decreases. Moreover, if the ion energy is reduced by the collisions, the effective sputter yield drops. The influence of the high energy ions on the plasma etch rate was also demonstrated by Coburn [153], who called the process "ion bombardment enhanced etching". The main impact of the accelerated ions is an increase in vertical etch rate, while the horizontal etch rate remains constant.

The speed of erosion is a function of the geometry to be etched, if the transport of the reactive species to the surface depends on rate. This effect emerges particularly for a high aspect ratio topography, whereas normally the etch rate decreases with growing depth of the etch grooves – a phenomenon called RIE-lag [154]. This can cause a faster growth of comparable large structures to the costs of smaller ones. Other known deviations from ideal anisotropic etching like "bowing", "trenching", and "dovetailing" (cp. Fig. 3.4 (right)) arise from the above mentioned electrical effects and ion scattering within the surface feature, etch rate dependence upon angle of incidence, redeposition of eroded material by plasma, and depletion of a reactant.

As already mentioned the electric properties of the polymer influence the charge transfer during plasma-ion bombardment. The dielectric strength can lead to electret domains that store the charge of the incoming particles until a critical breakdown leads to equalization. A rough estimation gives the calculation of the distance that is necessary to prevent a discharge with another domain. A short circuit current occurs, if the electric fields strength of the domains exceeds the dielectric strength. It follows for PMMA: 30 kV/mm = $30 \cdot 10^6$ V/m = 3 V / (100 nm), or a voltage in order of the plasma potential $U_P = 20$ V (additional bias potential $U_B = 100$ V) leads to: $600 \ldots 750$ nm ($3 \ldots 4$ μm). In this line of argument the patterns generated solely by U_P. U_B would cause significantly larger

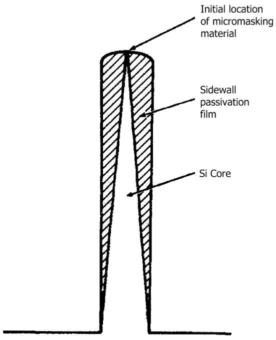

Fig. 3.5: *Schematic cross section of a single pin of a black silicon structure [17].*

domains than the SWS, which are not able to reduce reflection in the visible spectra region, but would introduce scattering.

The charging of the surface results in acceleration/deceleration of incoming particles, because of the change of plasma potential. The direction of the ion motion is determined by the degree of field distortion as a function of surface geometry, but the time of flight is determined by the ion energy and the size of the electric domain [155]. The deflecting effect for ions of a charged and structured surface is depicted in Fig. 3.4 (left).

The RIE process leads under special conditions to a structure formation on silicon surfaces that looks similar to that on the polymer surfaces induced by the APS process. In the literature this is known as "black silicon", "silicon grass", or "RIE grass". Some approaches assume contamination at the surface that acts as an etch mask enabling the patterning, which is widely used in microelectronics industry. Single atoms or molecules are not sufficient for masking in this dimensions. They have to form clusters that coalesce to closed films.

If the mask material is not adsorbed, it has to originate from the (chemical) modification of the surface itself. Oehrlein [17] used the oxidation of silicon to SiO_2 to describe the formation of a passivation layer. Thus, the quantities of the involved materials are crucial to the initiating step which is discussed in the community as "loading-effect". Besides, the formation depends on substrate temperature, pressure, and plasma power (degree of ionization, plasma temperature) as above-mentioned in this section. In the chemical regime the passivation is necessary to protect the sidewalls which demands for a sufficient fast oxygen passivation. In contrast to Sigmund, the model can describe the growth of features much bigger than the penetration depth of ions. The structure formation may be initiated by local density fluctuations of the passivation layer that leads to a micro masking, or due to an already existing structure caused by substrate roughness, or the above-mentioned ion-induced self-organization. Fig. 3.5 presents a schematic cross section of a single pin that forms the black silicon structure under assumption of a passivation layer.

According to the generation of black silicon the process was adapted to form an antireflection structure on silica glass surfaces by RIE [156]. Since a selective passivation film on top of surface cannot be formed solely from an oxidative plasma and the silica, a secondary material have to be introduced to the etch chemistry. The presence of aluminum during the etching helps by an ongoing formation of an Al_2O_3 layer that etches different than SiO_2. Moreover alumnia and silica are low-absorbing materials in the ultraviolet spectral region down to 190 nm, which make this process applicable to imaging optics of transmissive lithographic systems.

However, in the end of this section it has to be noted that ion irradiation is also responsible for smoothing, especially for high energy ion irradiation, when the chemical etching rate is small. This effect was attributed to surface diffusion at metals or enhancing the viscous flow at silica surfaces [149].

4 Manufacturing and instrumental analysis

This chapter discusses two topics. On the one hand, the fabrication equipment is presented, which is currently used to generate the antireflective SWS. This includes a detailed review of the utilized *in situ* analytics like plasma emission spectroscopy, quartz crystal monitoring, and recording of substrate temperature. Furthermore, Monte Carlo method is presented as a tool to investigate the mechanisms of energy transfer during the collision of impinging ions with the polymer target. On the other hand, SEM and AFM are evaluated as appropriate instruments for surface metrology. The transformation of the pin structure into a volume filling factor profile, which is necessary for optical modeling using EMA, is explained. Finally, *ex situ* and *in situ* optical spectroscopy are presented as fast, contactless, and non-destructive methods that are capable for industrial use. It is shown, which predictions about the surface morphology can be revealed from total scattering spectra.

4.1 Generation of subwavelength structures

The *Advanced Plasma Source* (APS) from *Leybold Optics* [157] was used for the surface treatment. The lateral cut is shown in Fig. 4.1. A cylindrical LaB_6 cathode is heated indirectly by a graphite heater to a temperature of 1500 °C. Surrounded by an anode tube, the hot filament cathode emits electrons that are accelerated in radial direction by the discharge voltage. A glow discharge plasma is created by impact ionization, if a noble gas such as argon is supplied into the internal space. Due to the magnetic field of a solenoid magnet, which surrounds the anode tube, the mobility of the charge carriers is increased in axial direction and decreases in the radial direction yielding in an improved cross section for impact.

The APS is mounted in a *Syrus*$^{\mathrm{pro}}$ deposition plant[1] that is evacuated by a combination of a cryogenetic pump (*Leybold Coolvac 10.000*) and a cold trap (Meissner trap) to a base pressure of 10^{-4} Pa. The working pressure p in the order of magnitude 10^{-2} Pa results from the balance between flow of the supplied gases, the leak rate, the pumping speed of the cryogenetic pump and the adsorption/desorption rate of the recipients inner walls. This implies a particle density N_0 in the order of 10^{18} m^{-3} and a mean free path length of 0.1 m – 1.0 m.

---

[1] The original task of the APS is to assist the deposition process by thermal evaporation with plasma-ions, whereas argon takes on the role of increasing the momentum of the condensing particles and the oxygen should maintain the stoichiometry of the growing film.

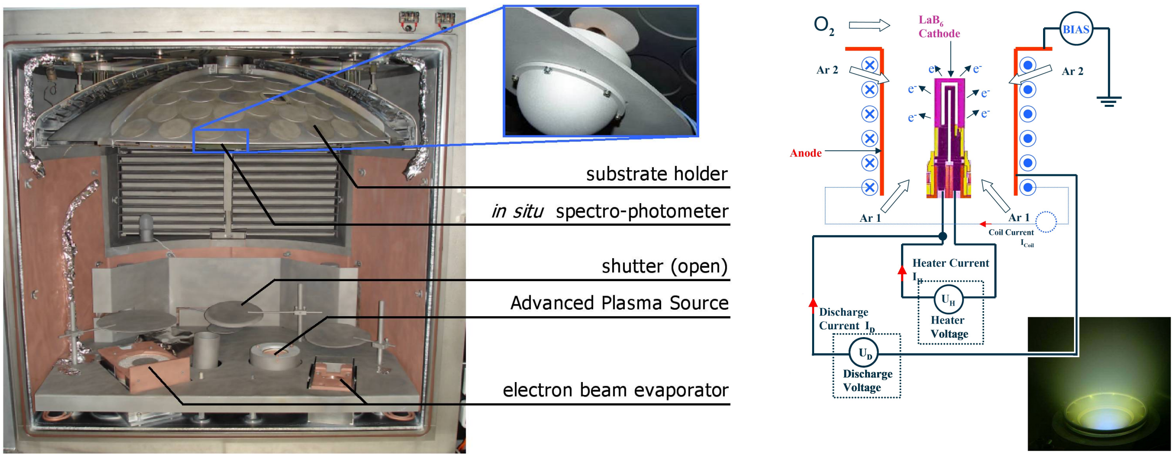

Fig. 4.1: *Leybold Optics Syrus*^{pro} *deposition plant (left), and sketch of the Advanced Plasma Source*® *with image of operating mode (right).*

The plasma expands into the chamber due to diffusion and impact-induced axial motion. Reactive gases such as O_2 or N_2 are provided via gas shower directly above the APS and get partly dissociated (activated) and ionized by ion/electron impact. An additional bias voltage U_B impresses between the isolated APS and the grounded chamber walls. This causes an additional potential drop along the plasma sheath, which represses the electrons and accelerates the cations stronger. U_B is a useful control parameter for plasma generation that is correlated with the mean kinetic ion energy. It depends on the discharge power, the gas flows and the coil current of the solenoid magnet.

The distribution of the kinetic energy of the impinging ions was determined earlier by Faraday-Cups, that are also known as Faraday Cage Collector [158]. The mean ion current density at the substrate holder is about 0.5 mA/cm^2 [159]. An energy-dependent measurement was achieved by ion retardation due to a static electric field of a counter voltage U_C. Only ions with a kinetic energy $E > e \cdot U_C$ are detected. For the APS the ion current as a function of U_C increases with pressure as shown on the left of Fig. 4.2. On the right, the slope $\mathrm{d}I/\mathrm{d}U_C$ gives information about the velocity distribution of the ions within an (infinitesimal) energy range. The peaks are attributed to the plasma potential $U_P \approx 20$ V and to the bias voltage $U_B = 120$ V. The rise in pressure causes a shift of U_P from 19 V to 28 V. If oxygen is added, more frequent energy transfer by inelastic collisions of the particles causes the broadening of the energy distribution peaks as the pressure increases.

Considering eq. (3.4), the electrons' temperature can be estimated for an argon flow of 14 sccm ($m_{Ar} \approx 40$ u) and $U_P = 22$ V: $T_e \approx 98500$ K. Furthermore, the Debye length follows $\lambda_D \approx 80$ μm from eq. (3.5) with the assumption of $N_e = \alpha_i \cdot N_0 = 6.7 \cdot 10^{16}$ m^{-3} at a pressure of $2.8 \cdot 10^{-2}$ Pa and the degree of ionization $\alpha_i = 0.01$. [2]

Noticing only the electric charge of the ions, the Faraday-Cup measurement is non-specific. The

---

[2] A rapid decrease in ion current when tilting the Faraday-Cups with respect to the substrate holder, suggests only a small number of non-normal (scattered) ion impacts to the surface.

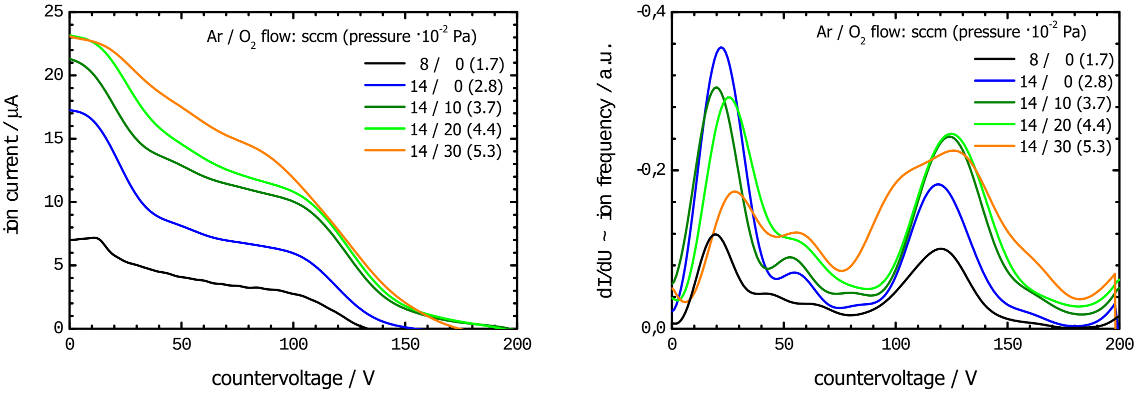

Fig. 4.2: *Ion current (left) and ion frequency (right) as a function of the counter voltage for different gas flows during an APS plasma, $U_B = 120$ V.*

kind of ion, neither oxygen nor argon, cannot be assigned from the ion energy distribution function of Fig. 4.2 (right). Because of the sign of the counter voltage, anions and cations cannot be detected at once. Mass spectrometers (e.g., time-of-flight, quadrupole) are more adequate methods for gas composition analysis [160].

4.2 Analysis of plasmas

4.2.1 Plasma emission spectroscopy

The principle uses light emission of the excited plasma species [161]. Excited ions and atoms release the energy ΔE during the transition from a high (excited) state to a lower state by spontaneous emission of a photon of the wavelength $\lambda = h \cdot c / \Delta E$. Having its specific energy states, each kind of atom or ion shows attributable emission spectra. The intensity of a certain line depends on the density of the species and the probability of the transition between the states [162]. Fig. 4.3 shows the optical emission spectra within the range 450 nm – 800 nm of the APS plasma, that was recorded with a grating monochromator and a CCD array detector ($\Delta\lambda = 0.5$ nm). The signal was coupled out of the recipient using a quartz glass window and fiber optics.

Since not calibrated to a known quantity of species, this method reveals only qualitative information about the occurrence. The spectral lines were attributed to the excited particles by the use of the Atomic Spectra Database from NIST [163]. Atomic and single-ionized argon have been detected as well as atomic oxygen and molecular oxygen ions. The high electronegativity (3.4 after Pauling) is the reason for a fast recombination of oxygen ions to atoms and recombination to molecules respectively. Having essentially less intense spectral lines, traces of Ti (gas shower), Cu (anode tube), La (cathode), B (cathode) ions have been detected in the spectra that were recorded with long-term integration.

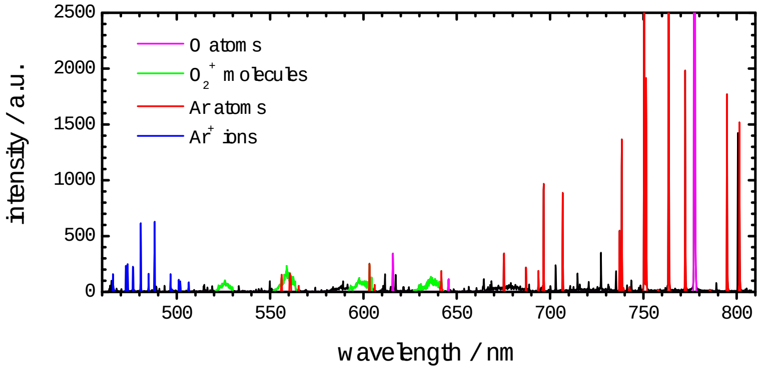

Fig. 4.3: *Photon emission spectra of the APS plasma (near to the source). Ar-flow 14 sccm, O_2-flow 30 sccm, bias voltage 120 V.*

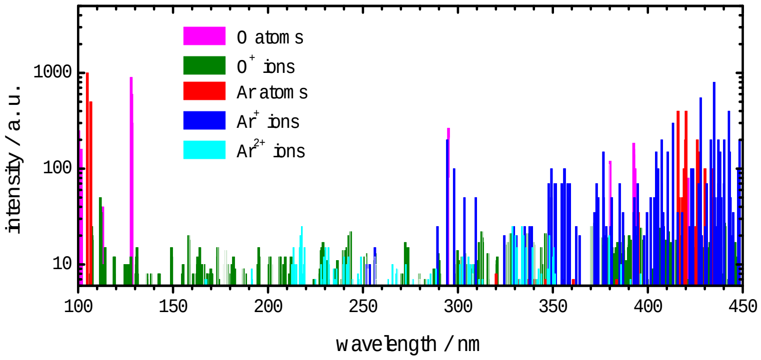

Fig. 4.4: *Expected photon emission spectra of the APS Ar/O plasma below the detectable wavelength.*

The optical loss of the used fiber optics in the UV range does not allow for a registration of photons that are able to break chemical bondings of the polymers. Thus, the expected spectral lines of the plasma particles are plotted in Fig. 4.4 with the knowledge of the detected species from Fig. 4.3 and the Atomic Spectra Database from NIST [163]. In contrast to the measured signal the spectra from the database incorporates no information about the frequency of occurrence (particle density in the excited state and pressure). The spectra of O^+ and Ar^{2+} are included, because they might be also apparent in the plasma, but do not show any strong emission in the measured wavelength range of Fig. 4.3. Intense spectral lines from Ar^+ are expected around 300 nm and most of the Ar^{2+} excitations emit above 200 nm. If O^+ is present, photons between 5 eV (250 nm) and 11 eV (110 nm) can lead to sustained modifications of the polymers according to sec. 3.3.2. Signals of high-excited atoms below 130 nm are very intense, but will be very rare due to the required excitation energy.

4.2.2 Heat-up and weight loss

The substrate temperature was measured by a thermocouple [164] at the front and the back surface of a PMMA sample during plasma treatment. Hence, the tip of the thermocouple is in the range

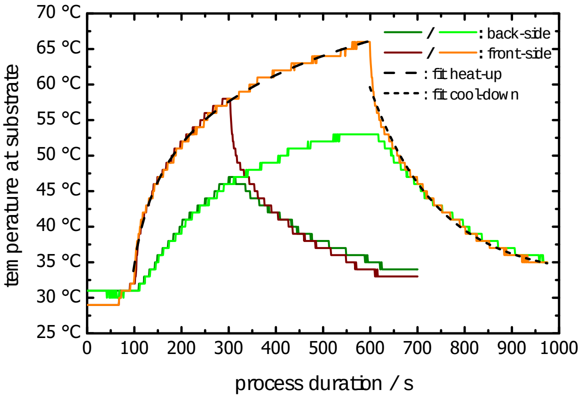

Fig. 4.5: *Temperature measured at front- and backside of a PMMA substrate during plasma treatment for two runs: 200 s and 500 s. $U_B = 120$ V, Ar: 14 sccm, O$_2$: 30 sccm.*

of several millimeters the measurement is rather macroscopic. The temperature was recorded with a precision of $\pm 1°$C each second.

As presented in Fig. 4.5 the etching starts at a time of 100 s. The previous temperature increment is associated with the plasma ignition, which is an effect of (reflected) thermal radiation, since a shutter blocks nearly all plasma particles during this initial stabilization process. The back side warms up slower than the plasma facing surface. The change in temperature of the back side is retarded by a couple of seconds, and the maximum temperature is lower than on the front. Both effects depend strongly on the heat impact from plasma, the substrate's thickness, and the thermal material properties, namely specific heat capacity and thermal conductivity. The slope of the heat-up may be described by a logarithmic increase, whereas the cool-down is an exponential decrease in analogy to natural decay processes.

For a 200 s duration the achieved temperature is below $60°$C, and after 500 s it is still below $70°$C. The slope steepens when the discharge power of the plasma source is raised (e.g., at high pressure or increased bias voltage). As a result of the analytics with the thermocouple, the typical plasma process does not achieve the critical temperatures (T_g) of table 3.1. The retarded heating of the sample's back side indicates thermal transport mechanisms inside the polymer. As the impinging plasma particles transfer their energy only in the surface near region, this method disregards that the temperature can reach or exceed microscopically T_g at the surface.

The processes of physical sputtering, chemical reactions, and photo-induced degradation sum-up into an overall etch rate Φ. The mass loss can be precisely measured with the use of quartz crystal monitoring[3] [88]. The resonant frequency f of a piezoelectric crystal is proportional to mass. Furthermore, the mass difference Δm can be converted into a volume difference $\Delta V = \Delta m/\rho$,

---

[3] This technique is actually used for determination of thickness of adsorbed materials during film deposition. Then a mass increase is observed.

where ρ is the specific gravity of the material that is eroded. For a constant base area A the volume changes proportionally with height ($\Delta V = A \cdot \Delta h$). The change in frequency is measured with high accuracy and thus the change in height $\Delta h = 1/(A\rho)\Delta m \propto 1/\rho\Delta f$ can be determined with high precision. The ablation rate follows with height change per time.

It is important to note that this measurement does not consider the surface structure and the change in thickness, that is understand as a mean ablation. Furthermore, the quartz crystal monitoring is an indirect method, meaning the measurement at a different location has not the same result as for the sample to which the result should be related. It is known from film deposition that the rate varies along the substrate holder and a so-called "tooling factor" is introduced. This multiplier has to be calibrated otherwise, such as by optical methods. Because only relative values are of interest, the calibration was not done.

To measure the polymer specific etch rate, it is necessary to overcoat the quartz crystal chip with this material. This was done by spin-coating with subsequent annealing for the particular solutions. Quartz crystals were coated with PMMA (7N), PC (Makrolon), PET (Teteron) and PA (Trogamid) of 1 μm – 3 μm thickness and tested with several plasma parameters.

4.3 Simulation of ion collision cascades in polymers

The physical interaction of plasma particles with the polymer surfaces comes along with collision cascades of the impinging ions and electrons within the surface or subsurface region [165]. Since most of the ions have enough energy to break chemical bondings, this section determines the influence of physical sputter erosion on the etch rate, when polymers are in the presence of a plasma or ion beam. The stochastic process of collision cascades was analyzed using the Monte Carlo method (MCM) software SRIM [166] to reveal the penetration depth and sputter rate. The former is equivalent to the mean penetration depth and will be given in average: $d_p = N^{-1} \cdot \sum_i d_i$. This value depends strongly on the type of interaction of the first monolayers of the target and is straggling (statistical spread) in the order of $\sigma_{d_p} = \sqrt{N^{-1} \cdot \sum_i d_i^2 - d_p^2} = 0.5$.

MCM is a stochastic method to achieve numerically a solution for a problem that is not (or with big expenses) analytically solvable. It bases on the frequent repetition of random experiments that lead by use of statistics to a result. The convergence in probability for a large number of experiments legitimates the method as long as each experiment is independent from another. Although a notable amount of double-charged ions has been detected in the plasma process, this analysis considers only single charged cations. SRIM executes the stopping of ions in compounds by using the formalism described by J. F. Ziegler and J. M. Manoyan [167].

Stable results, regarding the convergence in probability, are obtained for more than 20000 runs. Thus, the collision plots for different scenarios is shown in Fig. 4.6 for 20000 cascades of ions impinging on a PMMA substrate. The different dots represent the stopping location and their color

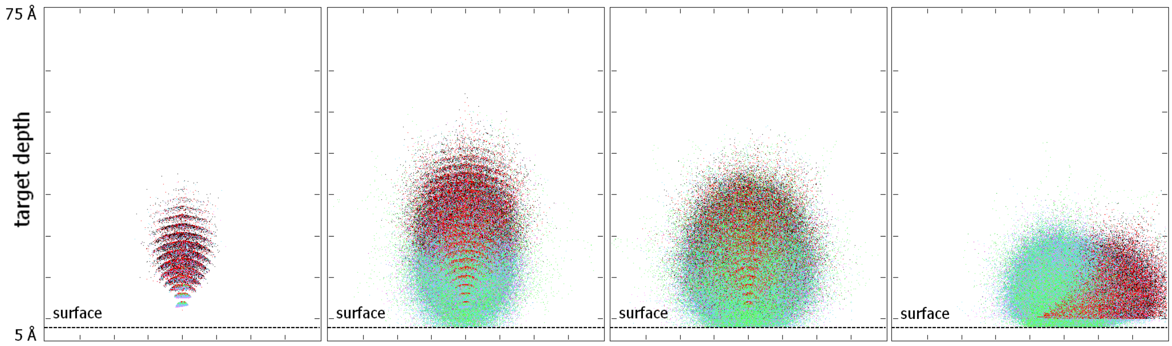

Fig. 4.6: *Collision plots for different scenarios: Ar^+, 25 eV, 0°; Ar^+, 100 eV, 0°; O^+, 100 eV, 0°; Ar^+, 100 eV, 80° (f.l.t.r.).*

encodes the affected target constituent atom during collision: (H) green, (C) blue, (O) purple.

From optical plasma emission spectroscopy ionic molecular oxygen (O_2^+) has been found. In MCM these are treated as two single charged ions ($O_2^+ \rightarrow 2O^+ + e^-$), because the binding electrons are the first to go after an initial collision within the first monolayers of a solid target. There are still effects while the atoms of the molecule remain close to each other since the ion polarizes the target proportional to the square of the ion's atomic number. For the polymeric targets, any target polarization may be very dilute, so that the quasi-molecular ion effect is minimal. In most polymers, it is assumed that there is only modest polarization of the medium by the impinging ion[4].

4.4 Surface topography

Since the lateral dimensions of the surface features are in subwavelength scale related to the visual spectral range, optical methods based on light microscopy cannot resolve the texture. The reason is the resolution limit after Abbe: $Y \propto \lambda/(n \cdot \sin\alpha)$, depending on wavelength λ and degree of coherence of illumination, geometry of aperture and numerical aperture [168]. This can be avoided by the use of high-resolution scanning probe microscopy for visualization. Appropriate probes are optical fiber tips (Scanning Near Field Optical Microscope), monolithic tips (Atomic Force Microscope (AFM), Scanning Tunnel Microscope (STM)), or an electron beam (Scanning Electron Microscopy (SEM))[5]. In this thesis, AFM and SEM were applied which are complementary techniques and provide a more complete representation of a surface, when used together, than if each was the only technique available. The resolution of the microscopes is not limited by diffraction, but only by the size of the probe-sample interaction volume.

---

[4] personal correspondence to J. F. Ziegler, author of SRIM.

[5] Strictly spoken, the SEM does not belong to Scanning Probe Microscopy, because the electron beam is not substantial.

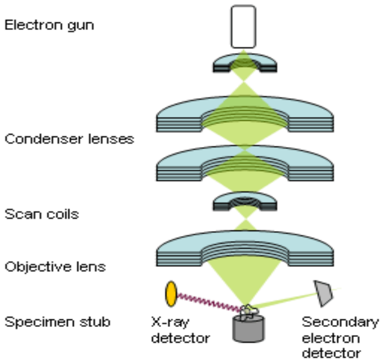

Fig. 4.7: *Principle of SEM*

4.4.1 Scanning electron microscopy

An electron beam scans the sample surface at high vacuum conditions, see Fig. 4.7. The electrons are thermal emitted from a tungsten filament, ceramic cathode (LaB_6), or via field emission. Magnetic fields from coils shape and focus the beam onto the surface. Hitting the surface, the beam is monochromatic with an electron energy in the range from several keV to 100 keV. Additional coils cause the deflection of the electron beam in two independent lateral directions leading to a scanning along the surface.

The incident electrons cause several complex interactions with the surface matter, amongst others electromagnetic radiation (EDX), secondary electrons (SE), backscattered electrons (BS), and Auger electrons that can be measured and evaluated separately, depending on the detector's parameters. The number of registered electrons from secondary electron emission or electron backscattering determines the intensity of the signal. Both processes depend on morphology leading to a higher number of detected electrons from peaks instead of pits. The result is an image of topography in means of intensity. In addition, the intensity of backscattered electrons due to Rutherford-Backscattering slips into with the forth power of the substrate's atomic number (Z^4) and allows for a material contrast.

The spatial resolution is limited by the size of the interaction area which is typical larger than the common used wavelength of an electron with an energy of some keV [169] [6]. The area from which electrons are registered is a function of electron energy, material, focus size, and distance to the detector. A second limitation arises from image acquisition. With digitalization, the smallest resolvable feature size is a pixel. Typical magnifications are 10× to 150000×. An advantage of SEM technique is its high depth of focus.

A XL40 from *Philips* [170] was used to analyze the majority of samples. It is equipped with SE and BS detector units. The sample is placed on a tiltable and rotatable stage allowing for off-normal electron incidence. Hence, it is feasible to visualize overhangs and undercutting or slanted surface

---

[6] $\lambda = h/p \approx 0.3$ nm – 3 nm follows for an electron energy of 5 keV – 50 keV.

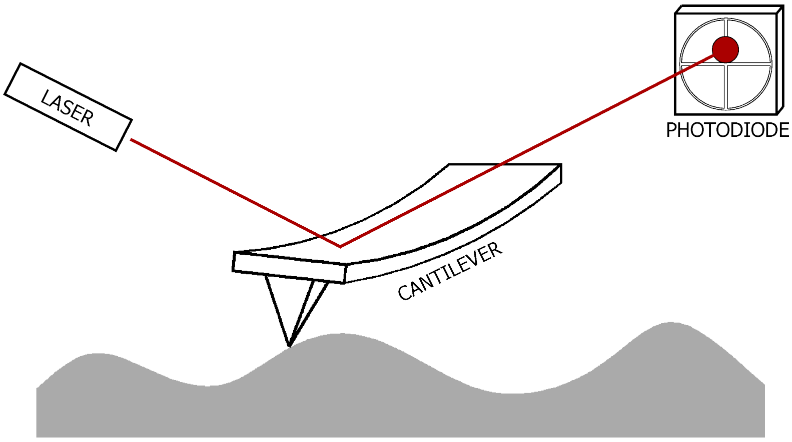

Fig. 4.8: *Principle of AFM*

features. An electric conductive sample surface is required for a sufficient imaging. Therefore, the samples have been coated with a ≈ 20 nm thick conductive gold layer that excludes the use of the BS detector at the same time. An alternative approach (currently not available) is to purge the sample chamber with an ionized inert gas that would be responsible for electric discharge. The polymer samples are extremely sensitive to thermal input and thus only electron energies less than 10 keV were used, which limits the practicable magnification to $30000\times$.

4.4.2 Atomic force microscopy

The AFM method is a further development of the principle of Scanning Tunneling Microscopy [171] that scans a sharp tip on the end of a flexible cantilever across a sample surface while maintaining a small force. A piezo-electric scanner conducts the scanning motion in two independent horizontal directions (x, y). The tip-surface interactions cause an amplitude of the tip and thus a vertical motion of the cantilever $h(x, y)$, which is monitored by a deflection of a reflecting laser beam using a split photo-diode detector, see Fig. 4.8.

Three working modes are to be distinguished. In *contact* mode, the tip is dragged across the surface while monitoring the change in cantilever deflection with the split photo-diode detector. A feedback loop maintains constant deflection (and thus constant contact force) of the cantilever by vertically moving the scanner. In *non-contact* mode, the tip does not contact the sample surface, but oscillates close to the surface ($<$ 10 nm) during scanning at a frequency which is slightly above the cantilever's resonance frequency. The resonance frequency is decreased by strongly distance-dependent dipole-dipole interactions (van-der-Waals forces) followed by a decrease in the amplitude of oscillation. Now the feedback loop maintains a constant oscillation amplitude or frequency by a vertical scanner shift. The *intermittent contact* mode or TappingMode$^{\mathrm{TM}}$ combines both principles leading to high sensitivity and spatial resolution [172]. The tip oscillates with a high amplitude of 20 nm to 100 nm near to the cantilever's resonance frequency and lightly touches or "taps" on the sample surface during scanning. Because the tip only contacts the surface briefly during each oscillation cycle, lateral shear forces are minimized that can tear the sample, distort data, or dull the tips. The feedback loop maintains a constant oscillation amplitude by setting a constant RMS of the oscillation. In all cases, the topographic image of the surface results from the scanner's vertical difference at each point. The spatial scan range exhibits typically 1×1 μm^2 - 100×100 μm^2.

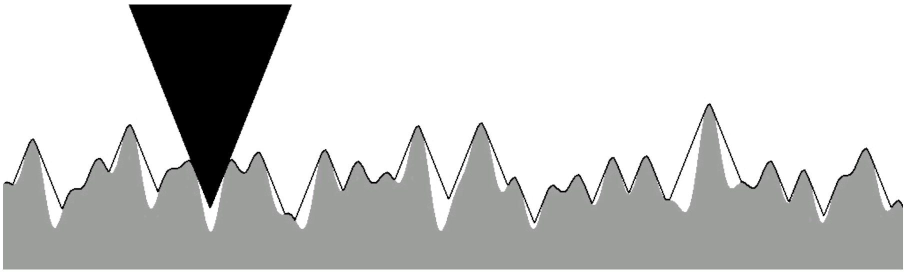

Fig. 4.9: *Visualization of the dependence of tip geometry on the result of AFM measurement [173].*

As seen from Fig. 4.9, the spatial resolution of AFM is strongly limited by the geometry of the used tip. The recorded height-profile (black line) $h(x, y)$ is a convolution of the real surface (gray profile) with the tip shape (pyramidal). Firstly, the smaller the tip's nominal radius of curvature (typically 3 nm to 10 nm) the smaller (higher) the detectable feature sizes (spatial frequencies). Secondly, the aspect ratio of the tip, given by the sidewall angle, decides on the best resolvable aspect ratio within the texture. The tip cannot profile sidewalls steeper than its own half-cone angle. Further restrictions in spatial resolution are pixelization of the image, whereas features that are smaller than the pixel size cannot be resolved, and the lateral scan range, that limits the lowest detectable spatial frequency.

If the resolution in the vertical direction is not governed by the tip shape, it is primarily determined by the resolution of the vertical scanner movement which is typically < 0.1 nm. Again, pixelization is limiting due to the maximum number of data points over the full vertical range of the piezo-scanner. In general, feature overhangs as generated by over-etching or grazing ion's incidence cannot be recognized by this technique.

A "diDimension$^{\text{TM}}$ 3100" device from *Digital Instruments* [174] was applied in TappingMode$^{\text{TM}}$ ($f \approx 320$ kHz) for sample analysis. High-aspect ratio tips out of high density diamond-like-carbon (HDC) with a sidewall angle of 7° ($=$ aspect ratio ≈ 4) and a tip diameter of less than 5 nm were used to maximize the spatial resolution. The sharp tip is about 300 nm long implying a width at its basis of about 75 nm. Contrary, this distance between two pins is necessary to allow for a full penetration of the tip into a groove.

The quantitative evaluation of the surface scans becomes clear, if represented as power spectrum. The power spectral density function (PSD) declares the value of a certain signal within an infinitesimal frequency band:

$$\mathrm{PSD}(k_x, k_y) = \lim_{l\to\infty} \frac{1}{l^2} \left| \int_0^l \int_0^l h(x,y) \exp\left(-2\pi \mathrm{i}(k_x x + k_y y)\right) \mathrm{d}x\mathrm{d}y \right|^2 \tag{4.1}$$

In the case of AFM a roughness component is plotted against its reciprocal correlation length (spatial frequency). The stochastic surface shows isotropic roughness and a 2D-isotropic PSD can be calculated by averaging over all in-plane directions. Further evaluation of the surface topography by cross-sectional line scans $h(x,y)$, histograms of the height distribution, and area filling factor determination ("bearing ratio") are discussed in the next section.

4.4.3 Determination of the filling factor

The volume filling factor ν_i describes the volume fraction of each material i in a composition with $\sum_i \nu_i = 1$. In the case of a grating, this is known as "duty-cycle". ν is a function of the structure's geometry. The volume filling factor is calculated according to the principle of Fig. 4.10 by setting the length of the projected line l under the curve for each height in relation with the length of the base line Λ. The latter is equal to the (effective) period in one dimension or the (effective) primitive cell in two dimensions:

$$\nu_{\mathsf{PMMA}} = \frac{l_{\mathsf{PMMA}}}{\Lambda} \qquad \nu_{\mathsf{air}} = \frac{l_{\mathsf{air}}}{\Lambda} \quad . \tag{4.2}$$

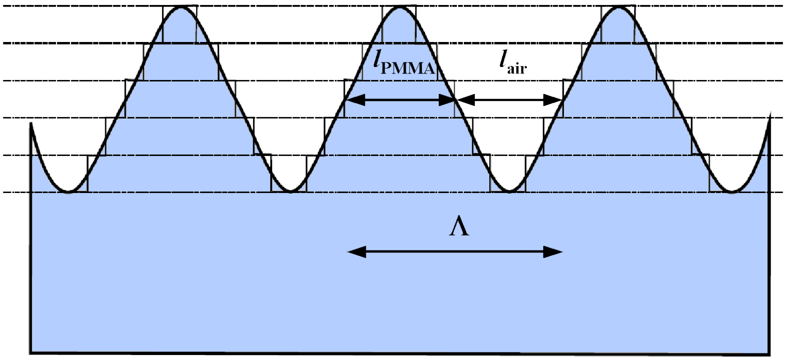

Fig. 4.10: *Derivation of the volume filling factor ν of a structured surface.*

In order to describe analytically the stochastic shape, an averaging process is necessary. On the one hand, the line-scan data (Fig. 5.25) can be used to estimate a deterministic shape of the pins with mean properties such as height and width. As a disadvantage, the specific base line of each pin cannot be considered. On the other hand, the digital height data of a mapped area from AFM can be evaluated using statistics. An effective ν-profile follows in both cases.

That method is suitable to topologies with surface features of well defined size like gratings or ordered arrays [175, 176]. Especially, the stochastic height distribution results in substantial modification of ν at the boundaries $h \to 0$ and $h \to h_{\mathsf{max}}$. They become shallower, because the occurrence of structures that contribute to the filling factor decreases at the boundaries. Moreover, the absolute size of the ν-profile extends, because of consideration of additional pins within the scan range.

Taking the statistics in all dimensions into account, a more realistic volume filling factor profile can be generated. The integration from the bottom to a certain height considers all data points on the surface below this altitude. The retrieved area is equivalent to the air-filled area. The other data points are not regarded, because their height is above the threshold, which means they are located within the pin, and thus belong to the fraction of the substrate material. It may be helpful to imagine a unique pin with the lateral dimensions of the mapped area and the height of the detected range. The subsequent normalization with respect to the scan area ($1\ \mu$m $\times\ 1\ \mu$m) leads to ν_{air}.

As the undercutting or slanted surface structures cannot be analyzed with AFM, their effect was not considered here. The former may cause a local change in monotony of ν, if the occurrence is dominant within a certain height range. The latter causes a decreased profile height with respect to the surface normal. Both modifications cause detrimental optical effects like scattering and thus should be suppressed in most cases.

4.5 Optical spectroscopy

Using optical spectroscopy at appropriate wavelengths is a common way to reveal the optical properties of surfaces (n, k) without sample destruction or even contact. Moreover, today exist high-sensitivity optical monitoring systems that are able to record a whole broadband spectra with a high photometric accuracy and a sufficient wavelength resolution at once within a few microseconds. Additionally, the main applicative aim beyond this work is the modification of the spectral properties of polymer surfaces in a way that reflection R is minimized in favor of an improved transmission performance T. Detrimental effects like scattering S and absorption A should be kept minimal. Enhanced information can be achieved using polarized light and/or light incidence from multiple angles. Total scattering (TS) and angle-resolved scattering technique (ARS) provide access to the surface's topography.

4.5.1 Ex situ spectroscopy

For *ex situ* measurements of transmission and reflection a commercial dual-beam ratio recording spectrophotometer *Lambda 900* from *Perkin Elmer* [177] was used, see Fig. 4.11. This all-reflecting optical system is equipped with two sequenced holographic grating monochromators in Littrow mounting. The deuterium and tungsten-halogen light sources and the high-sensitivity photomultiplier and peltier-controlled PbS detector allow for measurements in the spectral region from 190 nm to 3200 nm. The width of the slit can be controlled from 0.05 nm to 5 nm. The spectral precision is better than 0.2 nm in UV/VIS spectral region and about 0.5 nm in the NIR range. The photometric accuracy is limited by two effects. The reproducibility of a measurement is better than 0.3% which may result from

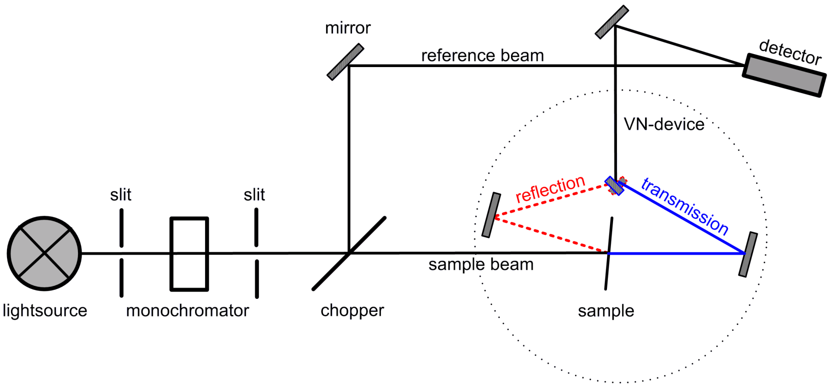

Fig. 4.11: *Optical path of the dual-beam spectrophotometer with VN-device from Perkin Elmer.*

long-term fluctuations of the light source's intensity after calibration. The noise within a measurement at stable conditions is about 0.5%. A special VN-device guarantees the absolute measurements of T and R at the same position at the sample surface, avoiding errors due to lateral inhomogeneities or tilt. The beam's angle of incidence is 6°, whereas polarization effects are negligible[7]. In addition, a comparable device for 45° angle of incidence was used in combination with a broadband polarizer.

4.5.2 In situ spectroscopy

Optical spectroscopy was also applied as process monitor to record *in situ* spectra during ion etching. Therefore, it is necessary to adapt the optical path to the conditions inside the vacuum chamber. The applied optical broadband monitoring system [178] performs transmission measurements of samples that are located at the rotating substrate holder of the *Syrus*$^{\text{pro}}$ plant, cp Fig. 4.1 (left).

A tungsten-halogen lamp, used as light source, is mounted in the recipient inside an integrating sphere [179] for homogeneous sample illumination. An additional gain-flattening-filter reduces the light's intensity in the near infrared spectral region to prevent partial saturation of the detector. The background illumination (signal) was minimized by setting up the place of measurement behind a shield (plate), which blocks the photons emitted from the plasma and the evaporating sources as well as the particle flux. After sample transmission, the light is guided to the detector via fiber optics [62].

The monochromator works in the spectral range from 400 nm to 920 nm, having a spectral resolution of 1.5 nm due to the number of pixels of the CCD sensor matrix. The photometric accuracy is limited to $\pm 0.5\%$, whereas the main errors result from Gaussian noise and should be reduced numerically by software after measurement. The ongoing recalibration of the signal is necessary, because the intensity of the halogen lamp and the detector sensitivity are drifting during the etching process. Practically, this is done for each transmittance spectra, and thus the lamp-, the background-

---

[7] at least for dielectric materials

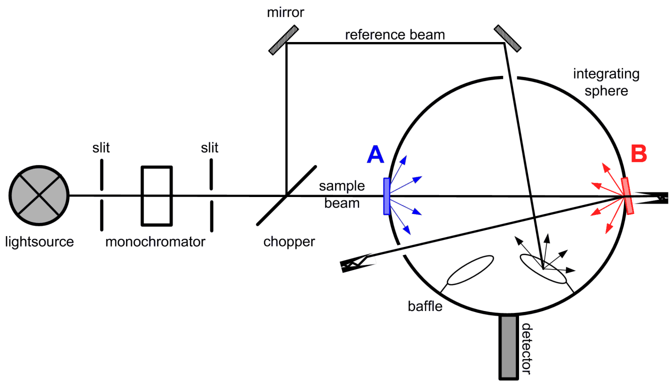

Fig. 4.12: *Optical path of the dual-beam spectrophotometer with integrating sphere from Perkin Elmer.*

and the sample-intensity are recorded for every turn of the rotating substrate holder:

$$T(\lambda) = \frac{I_{\text{sample}}(\lambda) - I_{\text{back}}(\lambda)}{I_{\text{lamp}}(\lambda) - I_{\text{back}}(\lambda)} \quad . \tag{4.3}$$

For clarity in illustration during parameter variation a mean transmittance is introduced by averaging the transmittance within the enhanced visible spectral region (400 nm – 700 nm). This means for the set of T spectra a transformation into a solitary curve that has an upward slope as long as T increases and is sloping down as T decreases due to scatter losses. At the maximum of T_{mean} the practical limit is achieved. The applicative limit for a "scatter-free" AR-effect is achieved a bit further, because close to the maximum the occurring scatter losses in the short-wavelength range compensate with the still increasing transmission in the long-wavelength range. Even small scatter losses may be noticed stronger by the human eye than slightly higher reflections.

4.5.3 Analysis of scatter losses

Being far from ideal, each material exhibits optical losses and the sum of reflectance and transmittance is smaller than unity. Optical loss groups into absorption and scattering. The rough surfaces are susceptible to scatter losses S, and an analysis can help in understanding the growth process and finding the reasons of an optimal switch-off time in the process. Scattering is distinguished between a volumetric origin (imperfections, local inhomogeneities) and the surface-related cause (roughness). The light that is diffracted by random perturbations can be described by scattering, too.

The total scattering (TS) results from integration of the intensity over the full solid angle, except the definite angles for direct transmission and direct reflection. TS is separated into forward direction (TS$_f$) for the transmittive hemisphere and the backward direction (TS$_b$) for the reflective hemisphere. The scattering was measured using a *Perkin Elmer* Lambda 19 spectrophotometer that works similar to the above-mentioned Lambda 900 device. TS was measured using an integrating sphere (ISO 13696) also known as Ulbricht sphere [180]. The sample is mounted as part of a strongly diffuse reflecting surface of the sphere, see Fig. 4.12. For TS$_f$ the sample was mounted at position A and having a normal light incidence. In TS$_b$-mode the sample is attached at position B and is tilted 7.5° according to beam incidence in order to couple out the reflected light. Beam traps absorb the directly transmitted and the reflected light.

With the use of scalar theories based on the Kirchhoff diffraction integral, the rms-roughness σ can be estimated from TS$_b$. Assuming small heights of the surface structure compared to the probing wavelength and considering only near-angle scattering, Bennett derived [181]:

$$S = R \cdot \left(\frac{4\pi\sigma}{\lambda}\right)^2 \quad , \tag{4.4}$$

which allows for proper describing of the impact of inhomogeneities in the order of the wavelength. The scattering from even smaller inhomogeneities or imperfections $\ll \lambda$ may be described by Rayleigh scattering [168]:

$$S \propto \frac{1}{\lambda^4} \quad . \tag{4.5}$$

Thus, the origins of the scattering can be determined from the wavelength dependence, and the TS$_b$ spectra spectra can be described by a function:

$$S(\lambda) = \left(\frac{X}{\lambda}\right)^{-4} + \left(\frac{Y}{\lambda}\right)^{-2} + Z \quad , \tag{4.6}$$

where the first term on RHS introduces scattering from very small particles (Rayleigh, $d << \lambda$, bulk inhomogeneities & SWS), while the second term on RHS originates from scattering of features in the order of magnitude of the wavelength (Mie, $d \approx \lambda$, waviness). Finally, the third term declares the scattering to features larger than the wavelength ($d > \lambda$, dust etc.). The coefficients X and Y show the weighting of the respective reason for scatter loss.

The alternative approach is to investigate the angular distribution of scattering. With its help, it is possible to distinguish between near-angle- and wide-angle scattering, which may be also helpful in revealing typical shape information of the SWS, since the angle-resolved scattering (ARS) spectra are correlated with the power spectral density function. ARS technique and AFM overlap in this application, so that it has been decided to prefer AFM. Nevertheless, ARS analysis is advantageous, if a direct, fast, and non-contact method is required or the effect of the roughness on a limited wavelength-range is important [22].

5 Research on subwavelength structures

The results of the instrumental analysis starts from the analysis of the etch rate, which is discussed in the context of findings from plasma analytics and Monte Carlo method. In the next step, the spectral properties of the plasma treated surface are analyzed in order to optimize the process and evaluate the polymers with respect to their potential for antireflective SWS. The temporal evolution of structure formation and the comparison of pin shapes between the polymers is given in the subsequent section. The analysis of pin shapes is also helpful for the computation of structural information from optical spectra. A separate section studies the origins of optical loss, especially the reasons for scattering and how scatter losses can be avoided. Finally, the structure formation is discussed in the context of self-organization.

5.1 The erosion process

From the preliminary considerations of plasma-polymer-interaction, a certain degree of material removal is expected during the plasma treatment. The erosion is discussed in the context of the results from PES, Faraday-Cup measurements, and MCM. The speed of erosion was measured by quartz crystal monitoring as described previously in 4.2.2. Fig. 5.1 shows the etch rate as a function of the bias voltage and the oxygen fraction of the plasma for the tested polymers.

The speed of erosion increases linearly with U_B for a fixed Ar:O_2 flow ratio of 2:1. The slope of the etch rate for PET is equal to PMMA, but both are steeper than that of PA and PC. The etch rate of PC is the lowest for most bias voltages, having half the value of PMMA. Because of the lower erosion speed for PA and PC, longer process duration than for PMMA can be predicted for them in order to achieve the same structure height. For instance, the duration should be at least 1.7× (2.3×) longer for PA (PC) than for PMMA at $U_B = 120$ V, if the growth process is comparable for the polymers.

The influence of the O_2-fraction in the plasma gas on the etch rate of PMMA and PET was measured at constant argon flow and bias voltage of 120 V. Here, the pressure doubles from $2.5 \cdot 10^{-2}$ Pa to $5.0 \cdot 10^{-2}$ Pa, if the O_2-flow increases from 0 sccm to 45 sccm. Again, the growth in etch rate is linear with the oxygen flow for both polymers, but the slope is higher for PMMA $(1.5\times)$ than for PET.

The etch rate is constant with time for maintained process parameters. At the same time, the

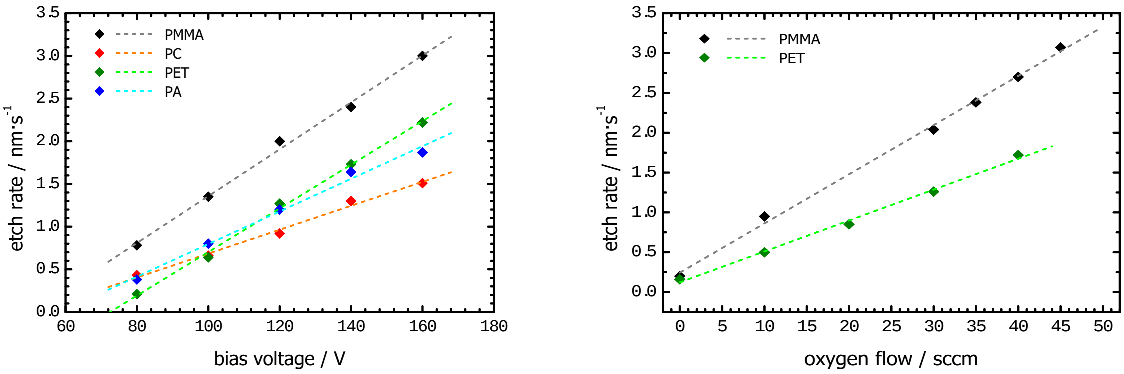

Fig. 5.1: *Etch rate of the tested polymers as a function of* U_B*, Ar: 14 sccm,* O_2*: 30 sccm, (left) and as a function of* O_2*-flow,* $U_B = 120$ *V, Ar: 14 sccm, (right) measured by crystal monitoring.*

substrate temperature increases with time according to Fig. 4.5, but does not exceed macroscopically the glass transition temperature T_g. Thus, it is suggesting that either an increase in temperature – even microscopically above T_g – does not lead to a significant variation in etch rate or $T > T_g$ is always valid microscopically.

The change in bias voltage has two effects. On the one hand, the mean ion energy varies, as revealed from Faraday-Cup measurement. On the other hand, the plasma emission spectrum intensifies as demonstrated by Fig. 5.2. As an explanation, the system control regulates the bias voltage to a constant value via the degree of ionization by changing the discharge power or the coil current of the plasma source[1]. When the discharge power is increased, more energy is used to excite the plasma particles. A strong increase is obvious in the emission lines of the specified particles, when U_B increases from 60 V to 80 V. A further increment to 120 V benefits mainly for the oxygen species, especially for O_2^+. The highest tested bias voltage of 160 V leads only to low additional rises in the emission bands, particularly obvious for the atomic oxygen line at 615 nm and the O_2^+ bands. Thus, an increase in (chemical) reactivity with U_B is evident by the frequent occurrence of ionic oxygen molecules and oxygen atoms from dissociation.

The number of impinging particles per time changes with pressure and the fraction of reactive species in the plasma varies with gas composition. Consequently, both parameters affect the fraction of physical sputtering and chemical etching of the total erosion. Because the probability of charge recombination increases with pressure, the ion source has to bring in a higher energy in order to guarantee for a certain degree of ionization for U_B-conservation. Again, the regulation of the bias voltage by the process control must be considered.

In the absence of oxygen, the ablation is comparable low for PMMA and PET (0.2 nm/s). At this point, the sputtering effect of the high energetic argon ions dominates the erosion. The chemical

---

[1] During a plasma-assisted coating process, it is important to have a constant momentum transfer by ions, which lead to a homogeneous densification of the condensing film material.

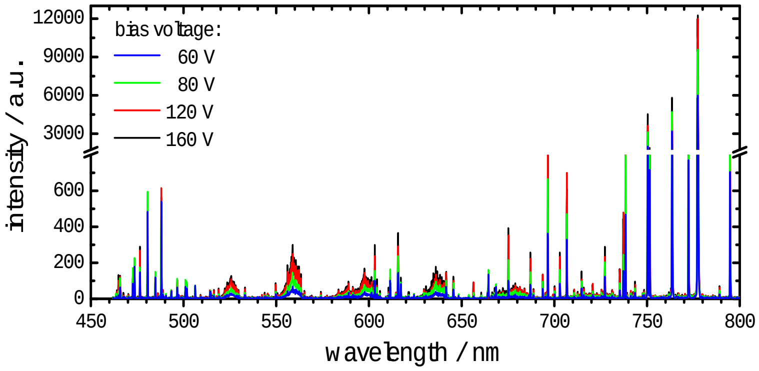

Fig. 5.2: *Dependence of the plasma emission on* U_B *for constant gas flows: 14 sccm Ar, 30 sccm* O_2*.*

etching from (oxygen) radicals of residual gas and dissociation products, which are still detectable by PES, is low. The same etch rate for different plastics is an evidence for a negligible selectivity of the sputter mechanism regarding the polymers' constituents. With increasing oxygen flow, the amount of reactive oxygen grows and the chemical decomposition process accelerates. The etch rate is about one tenth (sixth) of that for a typical plasma treatment with an O_2-flow of 30 sccm for PMMA (PET).

The chemical decomposition dominates the physical erosion as long as the former is not obstructed by a lack of reactants or the accumulation of products. Nevertheless, the physical mechanism can be the key to the structure formation via angle-dependent sputter efficiency as basic principle for the Bradley-Harper model [16] or the generation of a (passivation) layer on the surface in terms of Oehrlein's proposal [17]. The effects of ion bombardment on the sputtering yield have been investigated by Monte Carlo method. At first, the consequences of impinging Ar^+- and O^+-ions are examined in detail for PMMA substrates. Afterwards, the characteristics are compared with that of the other polymers.

Fig. 5.3 (left) presents the ion's energy loss ($\mathrm{d}E\mathrm{d}x$) for Ar^+- and O^+-ions impinging on PMMA caused by the target's nuclei and electrons. $\mathrm{d}E\mathrm{d}x$ increases with ion energy and is one order of magnitude smaller for electrons than for nuclei. Because the atomic mass of Ar is higher than for O, Ar^+ have a lower velocity than O^+ of the same ion energy, and thus notices a higher $\mathrm{d}E\mathrm{d}x$.

The ion range, depicted on RHS of Fig. 5.3, has been estimated by using the transport equation approach developed by Biersack [165] which allows to calculate rapidly the ion range over a wide band of kinetic energies. The ranges are accurate within 5%. Naturally, the mean penetration depth increases with ion energy, obtaining 2.2 nm (1.7 nm) for argon (oxygen) ions of 100 eV. This is two orders of magnitude smaller than the size of the antireflective SWS. Since the Bradley-Harper model treats only the self-organization in the size of the penetration depth, this fact is a strong restriction of its suitability for the observed structure formation.

Evaluating the recoil cascades statistically, the penetration depth is 5× (3×) larger than the lateral

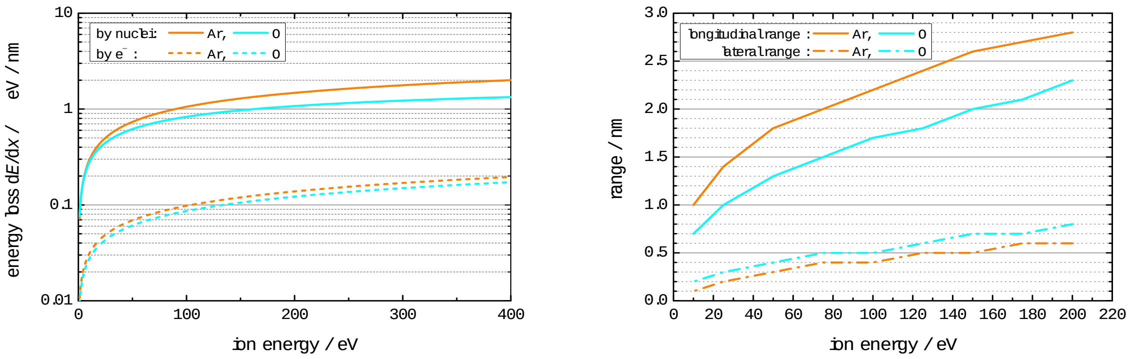

Fig. 5.3: *Energy loss of plasma-ions (left), and the mean range of collision cascades (longitudinal = depth, lateral = parallel to surface) (right), against ion energy in bulk PMMA .*

deflection range. This corresponds to a half cone of $\approx 6^\circ$ ($\approx 10^\circ$) for Ar^+ (O^+). The oxygen ions scatter stronger during collision (cp. Fig. 4.6) than argon ions which is a consequence of a comparable mass to the target atoms C, O(, N). The difference between longitudinal and lateral range indicates an angular dependence of sputtering, since the lateral deflection becomes more relevant on tilted surfaces. Moreover, the penetration depth is a rough estimation for the subsurface zone, which is modified by the impinging ions. Such a layer of differing composition or chemical structure may act as a protecting layer that inhibits further decomposition. As pointed out earlier from XPS and FTIR data, the surface region shows an enrichment of C-C bondings and oxygen bondings [98].

The total sputter yield Φ_S, which is the sum of the sputter efficiencies of the polymer's constituting elements, is presented for a plain and homogeneous surface in Fig 5.4 as a function of ion energy and angle of ion incidence. It results from MCM that Φ_S increases with ion energy. The slope is steeper for reactive ions than for Ar^+. Reactive gas ions do not sputter for normal incidence, if their energy is below 25 eV. Hence, the ions, which gain their energy from the plasma potential (cp. Fig. 4.2), do not contribute to the sputter erosion. This is even valid for Ar^+ up to 50 eV. The result denies or at least slows down the relevance of the sputter-induced roughening mechanism according to Sigmund [34] for low energetic plasmas with $E_{\mathrm{kin}} < 25$ eV. An increase in ion energy has constructive and destructive effects on the thickness of the subsurface region. On the one hand, the energy is deposited in deeper regions and forms an enlarged region of subsurface damage. On the other hand, the sputtering effect increases with ion energy, which causes a quicker thinning of the layer from top due to a higher Φ_S. Since the chemically less-modifying Ar^+ penetrate deeper than O^+, they cause an enhancement of the oxidative decomposition by providing additional energy within the collision cascades. However, the ratio of physical to chemical erosion increases with ion energy, which will end-up in a more anisotropic (directional) etching. Thus, it is assumed that a change in U_B has an impact on the achievable aspect ratio of the SWS that corresponds to the antireflection performance.

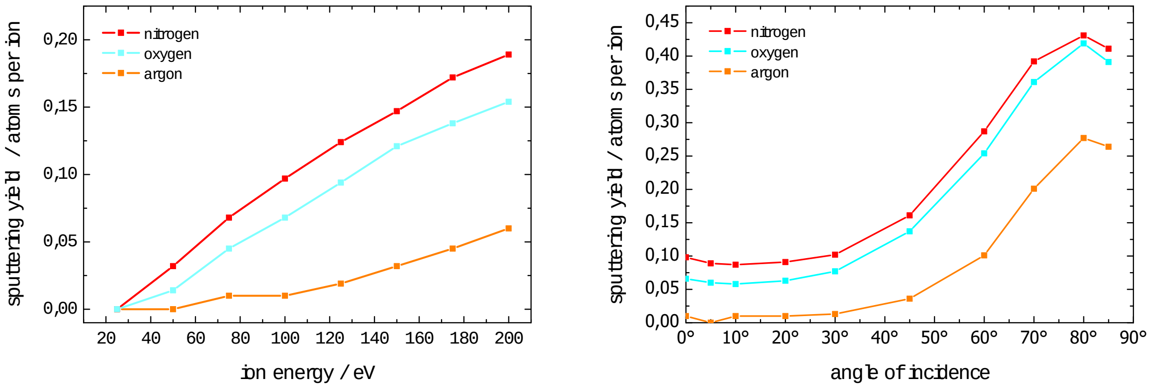

Fig. 5.4: *Sputter yield of PMMA for ions of typical process gases as a function of kinetic energy at normal incidence (left) and the angle of incidence at energy 100 eV (right).*

The revealed sputter efficiency of oxygen and nitrogen is quite similar, because the neighboring elements have comparable atomic weights. Nevertheless, the formation of antireflective structures was only observed for oxygen containing plasmas, and not for nitrogen as reactive gas [18]. In the latter case only a small scale roughening, comparable to the effect from the inert gas plasma was found. This finding underlines once more the importance of the chemical decomposition for the formation of antireflective structures. The difference in chemically reactivity between O_2- and N_2-plasmas has been already mentioned in sec. 3.3.1 and causes a reduced etch rate for the Ar/N_2 plasmas.

Φ_S increases tremendously for angles of ion incidence above 40° and reaches its maximum at $\approx 80^\circ$, having a 6 (27) times higher value than for normal incidence for oxygen (argon). The characteristics originates from the paths of the collision cascades, which run closer to surface for oblique incidence (cp. Fig. 4.6). Consequently, more recoil particles have the chance to leave the surface plane followed by an increase in Φ_S. If the angle of incidence exceeds a critical value, Φ_S drops rapidly. The collision cascades run now so close to the surface that the probability of an early lost of the impinging ions increases enormously. Then only a small amount of energy is transferred into the target, and a low Φ_S follows.

The plasma sheath-layer is much larger than the growing surface features. Thus, the ions impinge generally close to normal on the macroscopic surface plane. Contrary, the microscopic roughness of the substrate leads to a corrugated surface and oblique ion incidence. This leads in the case of pins, like that of Fig. 3.3 (right) with a half cone angle $\eta = \arctan(\Lambda/(2h))$, to an ion incidence of $\theta = 90^\circ - \eta$ at the sidewalls. The high Φ_S implies faster erosion and a subsequent amplification of surface features. According to Sigmund's theory (sec. 3.3.3), the predominant cones would exhibit $\eta \approx 10^\circ$ after ion-beam treatment. In terms of the generation of a subsurface damage region, the microscopic roughness leads to a decrease of the penetration depth and to an increase in the lateral range at the flanks. Thus, a thinner modification zone in the subsurface region follows at the sidewalls

Tab. 5.1: *Results of MCM analysis for different target materials and O^+- / Ar^+-ions.*

oxygen / argon	**PMMA**	**PC**	**PET**	**PA**
Stoichiometry	$C_5H_8O_2$	$C_{16}H_{14}O_3$	$C_{10}H_{18}O_4$	$C_{25}H_{32}O_2N_2$
ION ENERGY **20 eV**				
$\mathrm{d}E\mathrm{d}x$ nucl. / eV·nm^{-1}	40 / 44	38 / 4	42 / 46	40 / 43
long. range / nm	0.9 / 1.3	0.8 / 1.2	0.8 / 1.1	0.9 / 1.3
ION ENERGY **100 eV**				
$\mathrm{d}E\mathrm{d}x$ nucl. / eV·nm^{-1}	83 / 106	80 / 104	87 / 116	83 / 102
long. range / nm	1.7 / 2.2	1.6 / 2.1	1.4 / 1.9	1.7 / 2.3
ENERGY LOSS				
Ionization %	10.2 / 11.6	10.5 / 11.4	9.8 / 10.5	10.8 / 12.5
Vacancies %	3.1 / 2.0	2.8 / 2.0	2.8 / 2.1	3.1 / 1.9
Phonons %	49.0 / 52.8	48.3 / 53.1	47.4 / 51.6	49.0 / 53.0
Recoils %	37.7 / 33.6	38.4 / 33.5	40.0 / 35.8	37.2 / 32.6
SPUTTERING YIELD				
Total	0.068 / 0.010	0.053 / 0.010	0.074 / 0.013	0.058 / 0.010
hydrogen	0.047 / 0.004	0.033 / 0.005	0.032 / 0.005	0.045 / 0.004
carbon	0.007 / $5 \cdot 10^{-4}$	0.010 / 0.001	0.014 / 0.001	0.005 / $3 \cdot 10^{-4}$
oxygen	0.014 / 0.003	0.010 / 0.002	0.028 / 0.007	0.004 / $7 \cdot 10^{-4}$
nitrogen	– / –	– / –	– / –	0.005 / 0.001

of surface features, which can be discussed as the introduction of a regional-dependent selectivity in terms of a different etch resistance.

Table 5.1 compares the results of Monte Carlo method (MCM) for PMMA with those of the other polymers. The differences between them are small and refer solely to their stoichiometry and the total bonding energy per monomer. $\mathrm{d}E\mathrm{d}x$ is only presented for the interaction with the target nuclei, since the energy loss due to the target electrons is one order of magnitude smaller [2]. The reasons for the substantial energy loss are ionization, vacancies, phonons, and recoils. The former three processes can be caused in turn by recoils. Generally, argon ions cause more ionization and phonons than oxygen ions, while the latter lead to higher values of vacancies and recoils. The sputtering efficiency is highest for hydrogen, followed by oxygen and carbon. For PA only the sum of oxygen and nitrogen exceeds the value for carbon. The total sputtering yield of PMMA, caused by O^+-ions, is $\approx 7\times$ higher than for argon – for the other polymers this factor is still 5.5×. In the case of 20 eV, Φ_S is close to zero and vacancies do not occur.

---

[2] The influences of complex bonding effects, such as the stabilizing de-localized electron cloud of the phenyl group, are neglected.

In detail, the highest energy loss and thus the smallest penetration depth holds PET, while the others have nearly the same values. About 50% of the energy loss is attributed to phonons that cause the heat-up of the samples. The percentage of energy loss due to phonons increases to 80% for ions of 20 eV. Thus, the main part of the kinetic energy from the plasma is transformed into a heat-up, and a (local) exceed of the glass transition temperature could be the consequence, especially if T_g is lowered due to previous backbone breakage. In contrast to this, the energy loss due to vacancies is around 3% and is only of minor importance. Thus, the thermal-induced surface diffusion is rather suggesting as smoothing component than the vacancy-caused viscous flow diffusion, if the structure formation is discussed in terms of Bradley-Harper model.

The highest total sputtering yield exhibit PET followed by PMMA, PA and PC. An interrelation can be drawn to the carbon content and the number of C-C or C=C bondings according to Tab. 3.1. Moreover, this is in agreement with the assumptions of Gokan [111] (cp. sec. 3.3.1). Carbon has the smallest Φ_S of the constituents, so it becomes apparent that the amount of carbon at the surface limits the total sputter rate. PET and PMMA have a comparably low carbon fraction per monomer ($\approx 60\%$), and a small amount of energy stored in C-C and C=C bondings. The selectivity for sputtering is high for the constituents themselves, whereas it is slower for the polymers among each other. Effectively, there is no selectivity between the total Φ_S for argon ions, which is in agreement with the measured total etch rate of Fig. 5.1 (right), when oxygen was absent. The better performance of PMMA for typical processes may be found in its chemical structure. It is suggesting that the phenyl ring in the backbone of PET reduces the speed of chemical decomposition, which could cause the decreases in etch rate by 0.8 nm/s compared to PMMA. The erosion of PA and PC is even more impeded by two phenyl rings and high carbon content. This property is especially important for low ion energy, for which the modification (breaking) is less efficient than for high ion energy.

The sputtering of carbon is recognized as the speed-limiting step and thus, the additional quantum of oxygen quickens the carbon depletion by forming volatile CO^+ or CO_2^+. The linear correlation between oxygen flow and etch rate is an indication of the dominance of the chemical decomposition compared to the sputtering. Consequently, changing the gas composition will have an effect on the thickness of the modified surface region. The balance between subsurface damage and erosion at the surface shifts in a way, that the damage layer becomes thinner as the oxygen fraction increases. Since the Bradley-Harper model does not consider chemistry, a change in ion flux due to a variation in the degree of ionization is the only consequence of a pressure variation. From eq. (3.10) follows a smaller lateral feature size for a higher ion flux.

The investigated polymers show only minor differences in their energy loss mechanisms, longitudinal penetration depth, and sputter yield. Thus, from the point of view of MCM, there is no reason, why a comparable structure formation should be restricted to a single thermoplastic type. The more similarities in chemical structure the more comparabilities may be found in the surface structure.

However, there is one limitation: The total etch rate defines the speed of process, and the surface is pronounced to thermal load for long-term etchings. An additional question arises, whether argon ions are necessary for structure formation. Unfortunately, the experiment cannot be done, because the inert gas is urgent for plasma generation using the Advanced Plasma Source. The physical effect of argon ions could be substituted by oxygen ions of higher ion energy, causing a higher penetration depth. The same value can be achieved for O^+-ions having twice the kinetic energy of Ar^+. However, they exhibit higher sputter efficiency, the chemical modifications in the subsurface region are stronger, and the (oxidative) depletion of carbon are increased in such a regime. Recently, high-aspect ratio SWS were demonstrated from a pure oxygen-driven process [19] using a different plasma source.

It was learned from etch rate measurements and Monte Carlo method that the erosion depends strongly on ion energy and oxygen content. Plasmas that supply only ions with a low kinetic ion energy do not have significant sputter ablation, which is necessary for the discussed structure formation mechanisms. The enrichment of carbon at the surface seems to be the speed-limiting process that can be avoided by oxidation. The etch rate of typical oxygen driven processes are one order of magnitude higher than for a pure inert gas plasma, where sputtering dominates the chemical decomposition. The penetration depth of about 2 nm is too small to explain the formation of antireflective structures solely by sputter roughening. The generation of a layer with a different composition that impedes the process and introduces local etch selectivity is more likely. Furthermore, about half of the kinetic energy of the ions is transferred to a heat-up of the substrate in the surface region. This is a local effect in contrast to the thermal load from IR radiation. Thus, it is difficult to conclude the microscopic heat-up behavior from the measurements with a macroscopic thermocouple probe.

5.2 Antireflection effect

The reduction of reflection is driven by different needs. Suppressing reflected light at decorative surfaces or beam dumps does not take care of the transmitted part. The use of transparent polymers as substrates aims the optimization of light transmission by avoidance of any losses from reflection, absorption, and scattering. Thus, the ultimate goal is a maximized transmittance.

Fig. 5.5 shows the transmittance and the reflectance spectra of one-side plasma-treated PMMA samples for different process durations. A broad increase in transmittance and a decrease in reflectance are observed. The spectra of double-side treated samples are drawn in, to imagine the antireflection potential for an optical component. A peak value of 99% in transmittance has been achieved and means 7% more light intensity in transmission.

The reflection is reduced better for short wavelengths than for the long ones within a given process time. However, the zone of antireflection extends to long wavelengths with increasing duration. The residual reflection of the non-treated backside limits theoretically the reflection of the single-side plasma-treated samples. Since the absorption of PMMA is negligible in the VIS, this reflection is half the amount of the total reflectance of the untreated sheet. Consequently, the residual reflectance of a 600 s plasma-treated surface is about 0.3% at 550 nm, which might be the practical limit for these SWS.

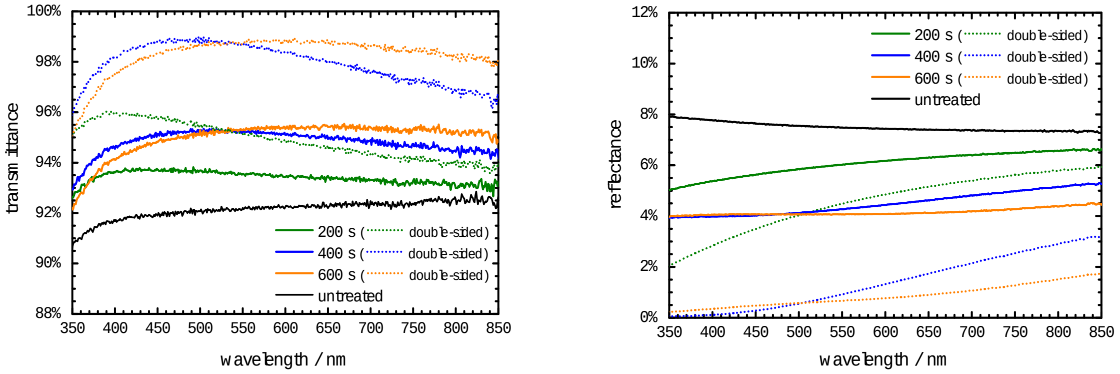

Fig. 5.5: *Transmittance spectra (left) and reflectance spectra (right) of PMMA at normal light incidence for different treatment times.* $U_B = 100$ *V, Ar-flow*$= 13$ *sccm, O*$_2$*-flow*$= 30$ *sccm.*

The transmittance reveals a slightly different view. The increase in T proceeds inversely for 200 s and 400 s, but subsequently a decrease is obvious for $\lambda < 500$ nm. Because the reflectance stays low in this region, the emergence of optical losses causes this discrepancy. The duration for an optimized performance is identified best with the help of *in situ* monitoring which has been used for the investigation of the ion energy and pressure dependence of the process.

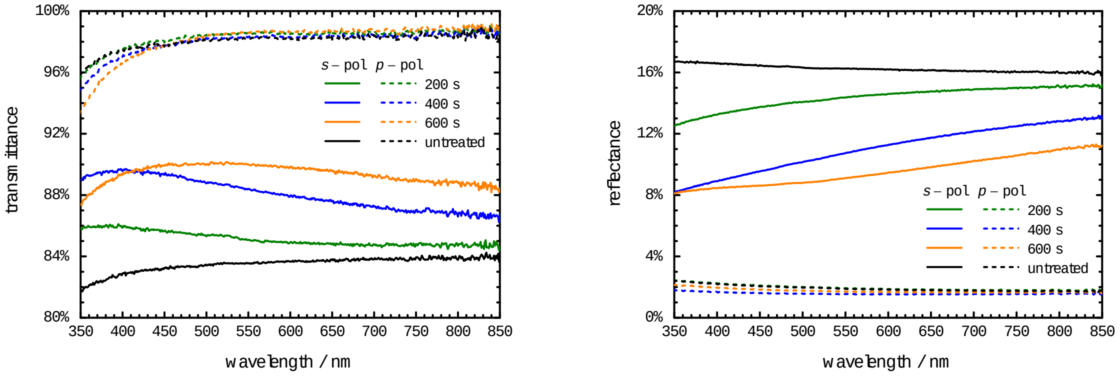

Fig. 5.6: *Transmittance (left) and reflectance (right) spectra of the same samples as in Fig. 5.5, measured under 45° light incidence.*

Oblique angles of light incidence are often inevitable in optical engineering. Prominent cases are lenses and diffractive optical elements. The optical path through the surface structures gets longer at oblique light incidence than for normal illumination. Moreover, the projected lateral feature size increases with respect to wavelength. Fig. 5.6 shows the transmittance and reflectance spectra for an inclination of 45°, split into s- and p-polarization. The average AR-performance, regarding the

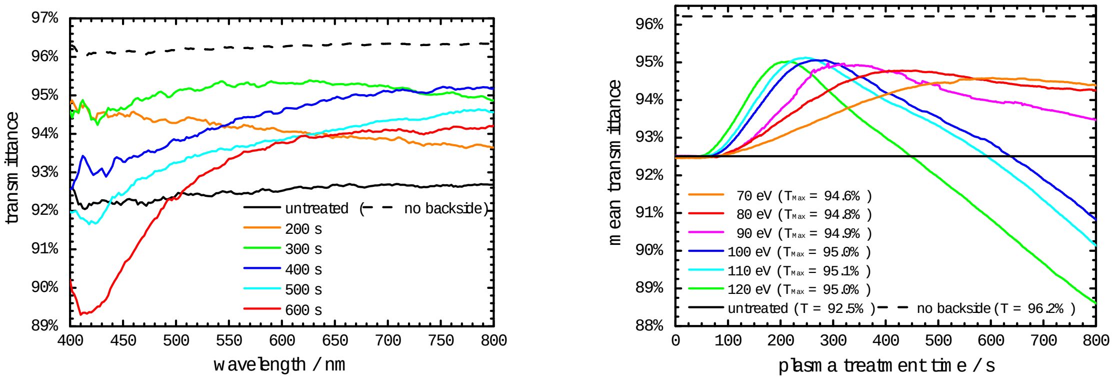

Fig. 5.7: *Transmittance spectra from broadband monitoring system during plasma treatment of PMMA for* $U_B = 100$ *V (left), and mean transmittance (400 nm – 700 nm) vs. duration for different* U_B *(right), all: 14 sccm Ar, 30 sccm* O_2.

polarization states, is lower than under normal incidence (6°), but is still significant. Now, optical losses in T_p are present below 450 nm even for the 400 s plasma treatment. This effect is not observed in T_s until a process time of 600 s. In contrast, the practical limit in reflection may be only achieved in the wavelength range below 450 nm.

The *in situ* spectrophotometry is an appropriate tool to compare the dynamics in the antireflection progress of the investigated polymers. Fig. 5.7 (left) shows consecutive transmittance spectra for a PMMA sheet during a plasma treatment ($U_B = 100$ V, 14 sccm Ar-flow, 30 sccm O_2-flow). The decrease in T is apparent for treatment times beyond 300 s. The transmittance drops below the value of the untreated sample in the short-wavelength range after 500 s. The measurement results from *in situ* monitoring are slightly higher than those achieved by *ex situ* spectrophotometry (cp. the spectra of the untreated substrates), because of unequal device functions. This effect must be considered in reverse engineering tasks from optical spectra.

For a better visualization, the mean transmittance is introduced by averaging T in the spectral range of interest (extended VIS: 400 nm – 700 nm). The progress of T_{mean} is presented in Fig. 5.7 (right) for different U_B. It becomes clear, that the maximum of transmittance T_{max} emerges sooner when the U_B increases. The peak transmission occurs for $U_B = 120$ V at half the time (≈ 215 s) compared to $U_B = 80$ V (≈ 425 s). This is in agreement with the increase in etch rate from 0.8 nm/s (80 V) to 1.9 nm/s (120 V) as revealed from quartz crystal measurement. The progress speed in this series is not directly comparable to that of the experiments of the *ex situ* analysis, because the gas and plasma parameters have been modified to have stable process conditions over a broad range of bias voltage variation.

The bias voltage, which is responsible for the mean ion energy and the fraction of reactive oxygen, accelerates the antireflection progress. Furthermore, the value of T_{max} increases slightly with U_B. Contrary, the peak transmission is significant lower for $U_B < 90$ V.

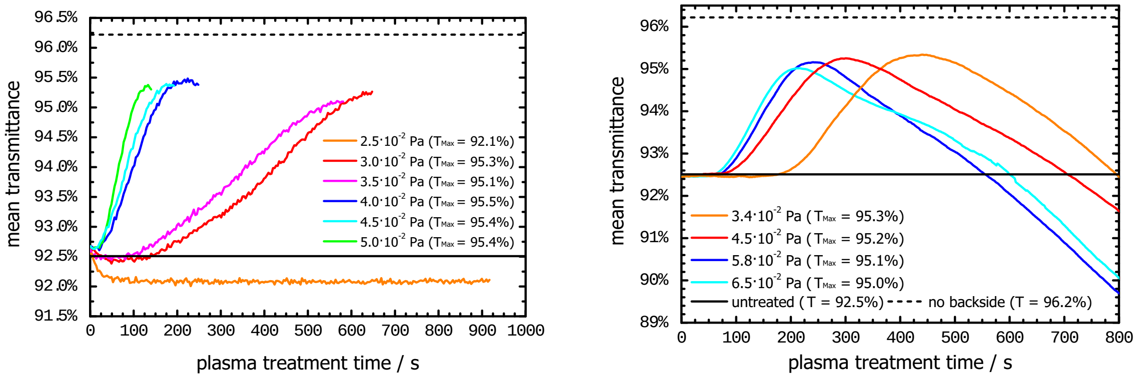

Fig. 5.8: *PMMA, $U_B = 100$ V: Mean transmittance (400 nm – 700 nm) vs. duration for different pressures by varying O-flow (left), and at constant gas mixture: O_2:Ar = 2:1 (right).*

An increase in process speed with oxygen flow is also obvious for the mean transmittance spectra as presented in Fig. 5.8 (left). Here, the process has been stopped shortly after obtaining the best *in situ* transmittance. The peak value is nearly independent of the oxygen fraction at constant argon flow, as long as oxygen is added to the process. In particular, the speed doubles when the pressure is increased by $1 \cdot 10^{-2}$ Pa. This correlates again with the results from quartz crystal monitoring that showed a doubling of etch rate when oxygen flow was increased from 10 sccm to 30 sccm.

The run at a pressure of $p = 2.5 \cdot 10^{-2}$ Pa was performed without any oxygen addition. The pure argon plasma causes a transmission decrease, which becomes constant after 100 s of duration. This is remarkable, since plasmas with oxygen fraction cause a continuous lowering in the excess of the peak transmittance and even drop significantly below the value of transmittance for the pure argon plasma treatment, cp. Fig. 5.7 (right) and Fig. 5.8 (right).

The impact of argon was studied by setting a constant flow ratio of Ar:O$_2$ $\approx 1 : 2$ at different pressures. The graphs for T_{mean} are plotted in Fig. 5.8 (right). Now, a variation in peak transmittance is evident beside changes in process speed. Again, a high pressure causes a sooner peak transmittance, but with the expense of a lower value. The increase in speed is mainly a result from the higher O$_2$-flow that scales with the Ar-flow. Secondary, an increased argon flow may lead to a more efficient oxygen dissociation, and thus to an acceleration of the etching process. The principal consequence of an increased argon flux to the surface plane may be a change in heat impact from argon ions, since they do not contribute to the chemical decomposition and physical sputtering plays only a minor role in erosion. The rise in pressure affects the thickness of the plasma sheath layer. However, the estimated value of ≈ 50 μm for $p = 6.5 \cdot 10^{-2}$ Pa is still two orders of magnitude higher than the typical structure height. Thus, it is expected that the directionality of particle impact is not critically lowered. The effect of non-normal impinge would arise for both series in the same way, but a decreased aspect ratio was found solely for high argon flows. Nevertheless, the drop in antireflection efficiency is smaller than that of low ion energies from Fig. 5.7 (right).

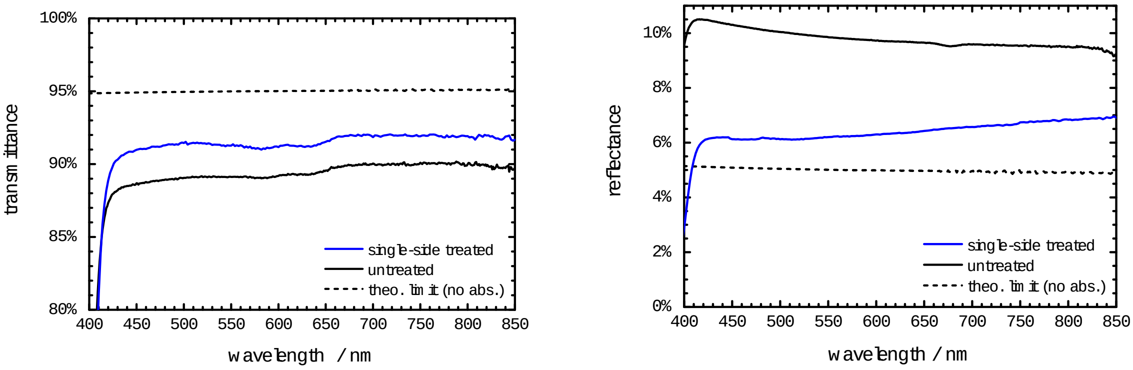

Fig. 5.9: *Transmittance (left) and reflectance (right) spectra of PC after treatment* (O_2 : *Ar* $= 45 : 14$, $p = 4.8 \cdot 10^{-2}$ *Pa*, $U_B = 140$ *V*, $t = 660$ *s), AOI* $= 6°$.

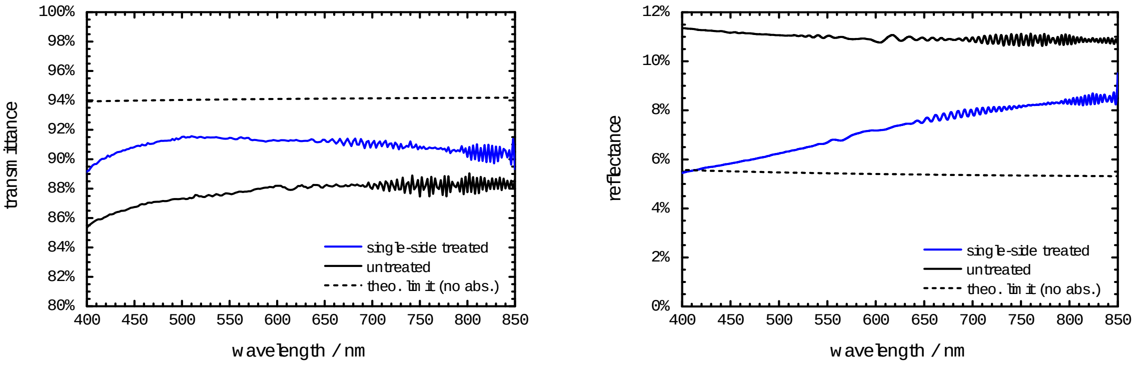

Fig. 5.10: *Transmittance (left) and reflectance (right) spectra of PET after treatment* (O_2 : *Ar* $= 15 : 12$, $p = 3.0 \cdot 10^{-2}$ *Pa*, $U_B = 120$ *V*, $t = 1800$ *s), AOI* $= 6°$.

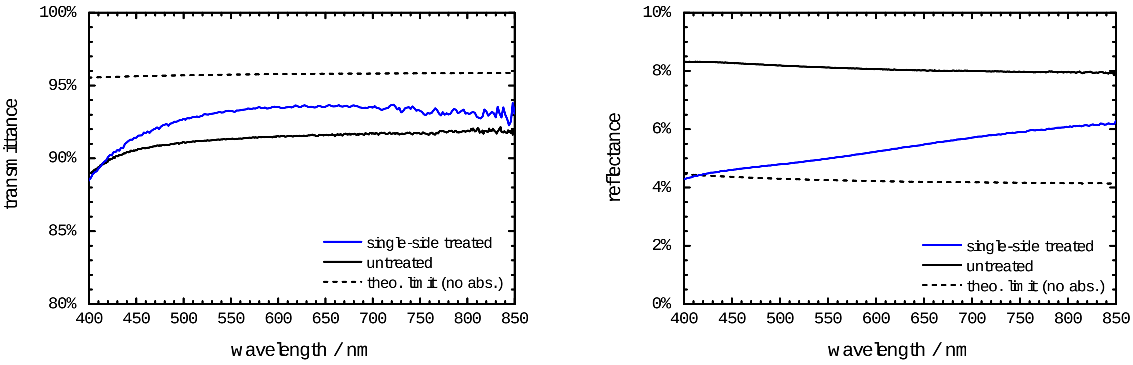

Fig. 5.11: *Transmittance (left) and reflectance (right) spectra of PA after treatment* (O_2 : *Ar* $= 37.5 : 15$, $p = 4.4 \cdot 10^{-2}$ *Pa*, $U_B = 160$ *V*, $t = 750$ *s), AOI* $= 6°$.

The transmittance and reflectance spectra after plasma treatment are presented for PC, PET, and PA in the figures 5.9, 5.10, and 5.11. All of the tested polymers show a significant increase in

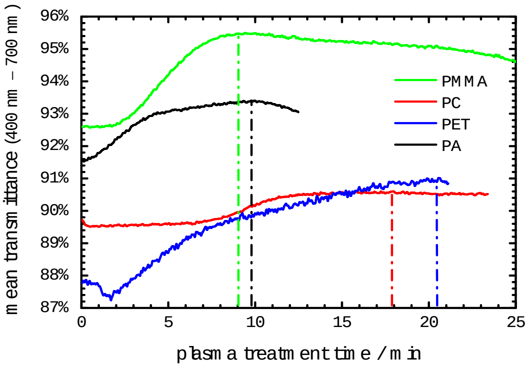

Fig. 5.12: *Comparison of the progress of mean transmittance for the tested polymers.*

transmittance. The captions present the process parameters that lead to the best antireflection performance at this time. The theoretical limits from the backside reflection are drawn in for clarification. Regarding the optical properties of the untreated substrates, the best improvement besides PMMA has been achieved for PET with $\Delta T \approx 4\%$. The ripples in the PET spectra result from interference due to the sheet thickness of only 50 μm. The transmittance increase for PC is about 2% within the whole VIS region, whereas the transmission of the treated PA suffers from the early occurring losses at short wavelengths, but is close to 1.9% above the substrate's value at $\lambda = 550$ nm. PET and PA achieve the theoretical limit for R at short wavelength limit, but PC does not. A detailed correlation between structure dimensions and spectral properties is discussed for PMMA in sec. 5.4.

It is important to note, that different plasma parameters had to be used in the processes in order to obtain these AR performances for the tested thermoplastics. PC and PA were plasma-treated by applying a higher U_B and a raised oxygen flow. It was pointed out previously that both settings affect the etch rate and the modification at the substrate's surface. Contrary, gentle plasma conditions were chosen for PET in the purpose of a low thermal load of the very thin substrates.

The difference in process dynamics for the tested materials is a striking fact and is compared in Fig. 5.12. The structure formation influences the spectra in the VIS range for PMMA and PET not until 1.5 minutes, while the increase in T_{mean} starts instantaneously for PA. The structure formation of PC is optically noticeable from the seventh minute on. PA shows a strong increase within the first four minutes followed by a shallow slope until it reaches its maximum after 10 minutes. The increment of T_{mean} for PET slows down with time, having its steepest slope between the second and fifth minute. The speed of increase in T_{mean} is analogous for PC and PMMA, but the latter tends to form a distinct maximum, whereas the former's peak transmittance stays nearly constant with time.

A small but very important detail is the transmittance decrease in the beginning of plasma treatment, which is particularly visible for PET and PC, but is also found in smaller amplitude for PA and PMMA. At this stage, this effect cannot be addressed uniquely to a certain change in one of the other photometric quantities for sure. Moreover it is not clear, if the cause of this decrease is reversible, or if it is compensated by the transmittance increase. This uncertainty motivated to carry out additional *ex situ* measurements that helped to attribute the loss to S, or A, which are discussed in section 5.5.

The tested polymers show a transmission increase in a broad spectral range after plasma treatment. The process speed varies for the different materials in agreement with the results from etch rate measurements. Thus, the plasma parameters must be adapted to the respective thermoplastic. The best antireflection performance has been achieved for PMMA, which results in about 99% transmittance for a double-side treated sheet under normal light incidence. Beside PMMA, the transmission improvement for PET is of industrial interest. It is important to stop the plasma treatment at the right time to prevent optical losses. The *in situ* spectrophotometry is the adequate tool for this task.

5.3 Structure formation

The formation of the SWS was observed with atomic force microscopy and scanning electron microscopy. Since both methods have limits in imaging, their use must be well considered. First, the structure formation is analyzed via AFM, which gives best results as long as the structure's aspect ratio does not exceed that one of the measuring tip. The comparison of the different polymer surfaces at the stage of best antireflection performance (cp. previous section) is carried out by sharing data from both methods. Here, complementary information is evaluated in order to obtain a more general view of the structured surfaces. Furthermore, efforts are made to correlate the difference between the habitus of the pins with results of the erosion analysis. Finally, the shape of the structure is investigated in preparation for the reverse engineering of the following section. Therefore, profiles of individual pins and the figure from statistical AFM analysis are expressed analytically.

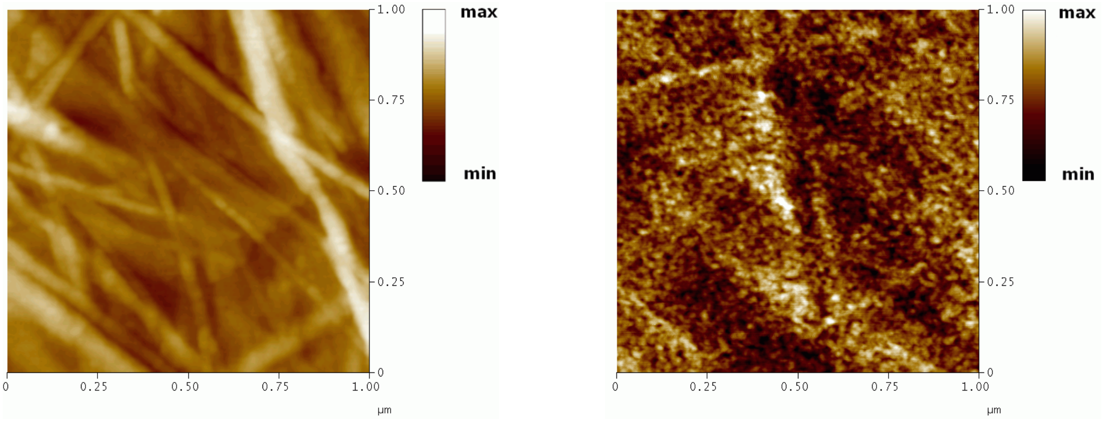

Fig. 5.13: *AFM-scan of an untreated PMMA surface (left) and after 10 s plasma treatment (right).*

Starting from the surface of an untreated PMMA substrate, only grooves from the molding tool are recognizable in Fig. 5.13 (left). Their typical height is 2 nm – 3 nm which is not of relevance for the optical properties in the VIS region. A roughening is instantly obvious with the beginning of plasma treatment. The following plasma parameters were used: $U_B = 120$ V, Ar flow = 13 sccm, O_2 flow = 30 sccm. Fig. 5.13 (right, illustrated in a separate color scale) shows a granular surface for a treatment time of 10 s – so the initiating step for self-aligned structure formation has happened already before that moment. The height range doubles, achieving ≈ 5 nm, but a distinctive pin structure is not visible at that time. The investigation of earlier stages is problematic, since the plasma-influencing parameters are still unstable in the beginning and cause non-reproducibility.

With ongoing plasma treatment, the pin structure becomes visible as depicted in Fig. 5.14 for four consecutive scans after different durations ($t =$ 30 s, 100 s, 150 s, 300 s). The color ranges have been equalized for a better visualization of the growing process. Tab. 5.2 lists the according height range with other averaged feature sizes.

The (mean) diameter of the pins increases with time (FWHM = 25 nm, 40 nm, 50 nm, 85 nm). Since the pins are standing compact together, this can only happen, if some of them vanish. Evidently, the smaller pins are suppressed stronger in their growth than the bigger ones, which indicate more intense erosion at their position. Vice versa, the pin size is a function of available space. Residual topography from the casting tool is still detectable in the scan of the 100 s treated surface. There is only a weak affinity of the pins to arrange along such grooves, and the initial topography does not confine the structure formation.[3] The elimination of smaller pins during the growth, suggests that the topography does not originate from an intrinsic property of the substrate, that is bared by leaching, but results from the etch process itself.

In analogy to the silicon grass fabrication, where small impurities are discussed as trigger for micro masking, contamination of plasma-treated surfaces was also detected by XPS [18]. The amount of foreign atoms (with respect to the polymer) increased with plasma treatment. The sputter efficiency of the detected species Si, Cu, La is extremely low and their oxides are non-volatile. If the impurities would be present already at the beginning, all the pins should possess about the same height, as it is known for silicon grass. In this context, the significant height distribution for PMMA surface could be an evidence for a permanent pollution by plasma, or an induced mobility [149] of the mask material due to high energetic ions from the plasma.

SEM analysis reveals first effects of structure formation not until 100 s of duration. At this time, the surface is covered with small dimples (Fig. 5.15), which have diameters of about 50 nm. Probably, the preparative gold coating has smoothed the finer structures. Considering the accuracy of measurement, this is in agreement with AFM analysis. The location of the dimples appears randomized and independent from each other. The local increase in etch rate may arise from density fluctuations of the substrate material. Contrary, the inhomogeneities are present independent from fabrication and are incapable of measurement with non-scanning methods, AFM, and SEM. Surface

---

[3] The structure formation was also observed on surfaces of substrates that had been fabricated by casting and spin coating, which exhibit a different initial topography and roughness.

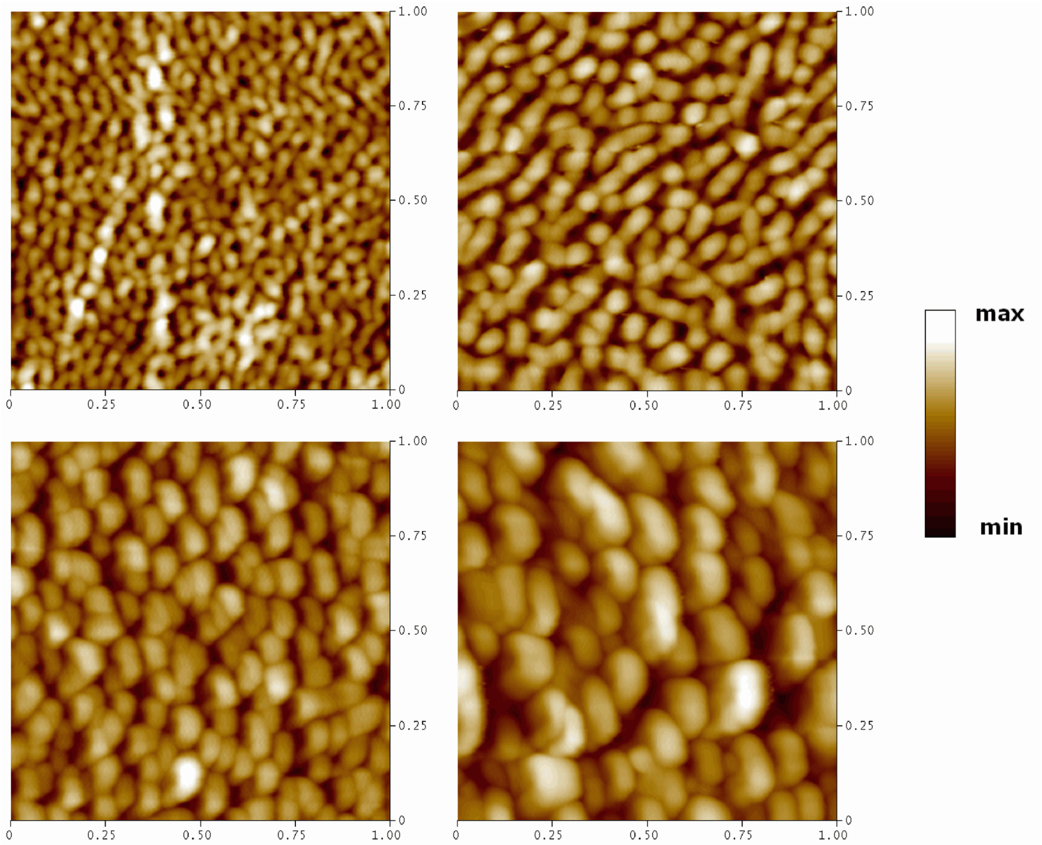

Fig. 5.14: 1×1 *μm^2 AFM-scans of a PMMA surface for increasing plasma-treatment times: 30 s (top-left), 100 s, 150 s, 300 s (bottom-right).*

charging as a reason is unlikely, because charge domains are expected to be larger and the dimple structure implies a local acceleration of the ions to increase the etching. If charging is important at this phase, the initial roughness from the molding tool would influence the structure formation in a more distinctive way. A weak alignment of dimples along the grooves is obvious, but it is expected that charging influences the orientation also in the immediate vicinity.

A methodical analysis of the scan areas is given by the power spectral density function (PSD), which is shown in Fig. 5.16 for the five treatment times in combination with the PSD from the untreated surface. The combined plots have been merged from single PSDs of three scan ranges using a weighting algorithm [182]. The PSD of the 10 s treated sample was only taken from a 1×1 μm^2 scan and was not weighted like the other PSDs in this frequency range, and is shifted therefore.

Real surfaces with a self-similar roughness cause straight lines with negative slopes in double-logarithmic scale. The untreated surface shows a comparable behavior. The incipient structure formation violates the affinity and the deviation from the curve follows. A distance correlation between surface points of the same height value is introduced as "correlation length", L_C. The

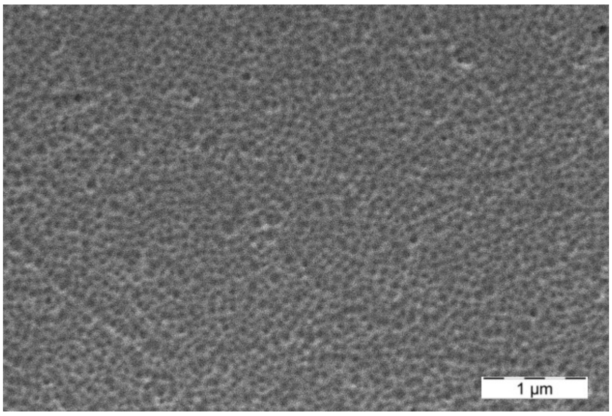

Fig. 5.15: *SEM micrograph (topview) of a PMMA surface after a plasma treatment of 100 s.*

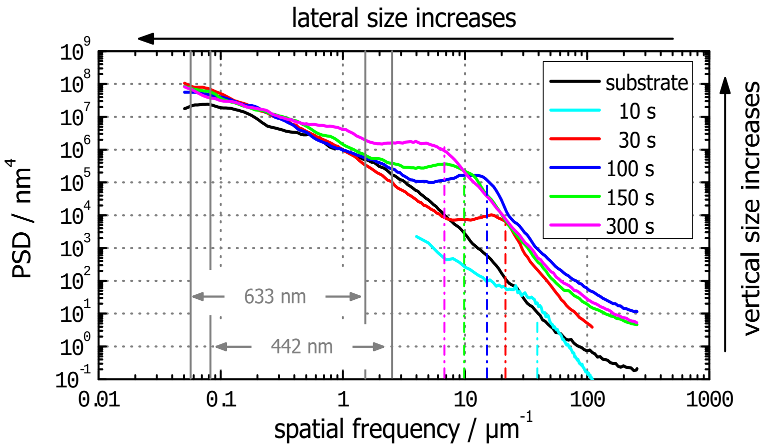

Fig. 5.16: *PSD function of structured PMMA surfaces for increasing treatment time, merged from three AFM scans:* 1×1 *μm^2*, 10×10 *μm^2 and* 100×100 *μm^2*.

maximum deviation from the ideal curve appears at the spatial frequency that corresponds to the mean L_C. A correlation length of about 30 nm has been found even for 10 s from PSD. With ongoing plasma treatment, the bulge shifts to lower spatial frequencies, implying an ongoing lateral growth. As the bulge moves along the substrate curve, the PSD-values also increase, because of the normal pin evolution.

L_C cannot be identified simply with the typical pin width (full width at half maximum, FWHM), since the distances to the points of all flanks are considered. If the features have different heights, L_C increases stronger than the pin width. Because the space between the pins is also considered, L_C can be seen rather as effective period than as FWHM. A comparison of L_C, FWHM, height range, rms-roughness, and the calculated aspect ratio during the pin growth is given in Tab. 5.2.

To demonstrate which lateral size is necessary to violate the subwavelength criterion and cause light scattering in the VIS region, the respective ranges of the spatial frequency are drawn into

Tab. 5.2: *Averaged pin sizes, aspect ratio, and rms-roughness during the plasma treatment process of PMMA.*

time	L_C	**FWHM**	**height**	**aspect ratio**	**rms-roughness**
untreated	–	–	2.6 nm	–	0.5 nm
10 s	30 nm	15 nm	7 nm	0.5	0.8 nm
30 s	45 nm	25 nm	50 nm	2.0	4.1 nm
100 s	65 nm	40 nm	80 nm	2.0	7.2 nm
150 s	105 nm	50 nm	100 nm	2.0	10.2 nm
300 s	150 nm	85 nm	135 nm	1.6	18.0 nm

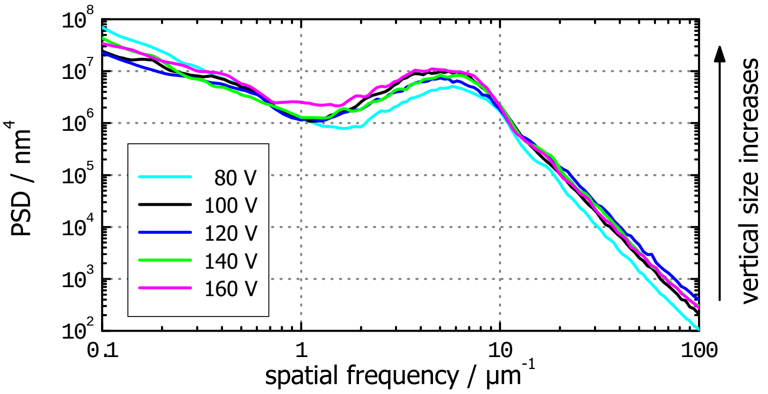

Fig. 5.17: *PSD function of structured PMMA surfaces for various bias voltages during plasma treatment.*

the PSD plot for two wavelengths. They correspond to the angle of scattered light under normal illumination. The left limit marks a L_C that causes scattering in normal direction, whereas the right border addresses the scattering into an angle close to 90°. 10×10 μm^2 and 100×100 μm^2 scans can only detect these spatial frequencies. The bulge is outside of the interval for the shown treatment times. Inside, the curves of the treated samples are close to that of the untreated substrate, meaning no additional scattering from the pins themselves. The exceptional case is the scan for 300 s, which exhibits a second bulge at the right limit (in the center) for light of $\lambda = 633$ nm ($\lambda = 442$ nm). Consequently, for this sample noticeable scatter losses are expected. The argumentation refers only to backscattering – a scattering in forward direction is even more critical, because of the impact of the substrate's refractive index on the lateral structure size in compliance with the subwavelength condition eq. (2.6). A more detailed analysis of scattering is given in sec. 5.5.

In principle, the investigation revealed an increase in structure dimensions with time. The question is now, if it is possible to control the size via setting the plasma parameters. Fig. 5.17 demonstrates the influence of the bias voltage on the PSD. Therefore, the processes were stopped at the time of

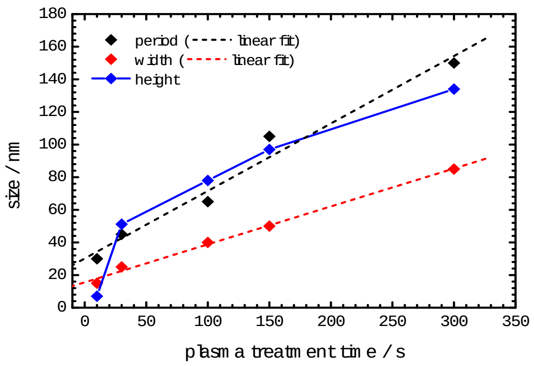

Fig. 5.18: *Visualization of feature size data from table 5.2 for consecutive etch times.*

peak transmittance, which lowers since as the process speeds up due to higher U_B. In this context, it is remarkable that the product of treatment time and mean ion energy (U_B), which represents the physical quantity of an action, stays nearly constant.

Only slight differences in the height and the width of the bulge are obvious. They are on the same position regarding the spatial frequency ($\approx 8\ \mu$m^{-1}) implying a correlation length or effective period of about 125 nm. The run with $U_B = 80$ V shows a significant smaller bulge referring to a lower structure height. This finding correlates with the change in T_{max} from the *in situ* spectrophotometry of Fig. 5.7, which differs notably for bias voltages below 100 V. The smaller width of the bulge is advantageous for the prevention of scatter losses in the VIS.

Fig. 5.18 illustrates again the variation in the size, according to tab. 5.2. The pin growth is very fast within the first 100 s. Because the height increases faster than the width, an aspect ratio of about 1:1 is obtained around 15 s at a size of 20 nm. A ratio bigger than unity is established from 30 s to 200 s, when the blue curve is above the red one. The width and the period are fitted by straight lines, implying a linear growth with time. Evidently the period (L_C) increases faster than the width. Although the height shows a linear increase for most of the time, it was not fitted by a straight line in order to consider the initial slope and a potentially constant (average) pin height as a steady state for long durations. A logarithmic function may be an adequate approximation.

From the AFM's point of view, this result suggests a stable aspect ratio around unity, which implies an upcoming of scatter losses with ongoing pin growth. Contrary, a constant limitation of height may also result from the aspect ratio of the AFM tip which restricts the detectable height range due to a necessary groove width for getting at the bottom of the grooves themselves. This effect should play a role only for the bottom of the pits as mentioned in Fig. 4.9. The tips half-cone angle of about 7° complies with a tip aspect ratio of ≈4. However, the limitation in aspect ratio affects mainly the detectable structure height, which affects rather the description of the antireflection performance than the impact of the scatter losses.

To overcome the dilemma of AFM analysis, it is preferable to switch to the alternative imaging of

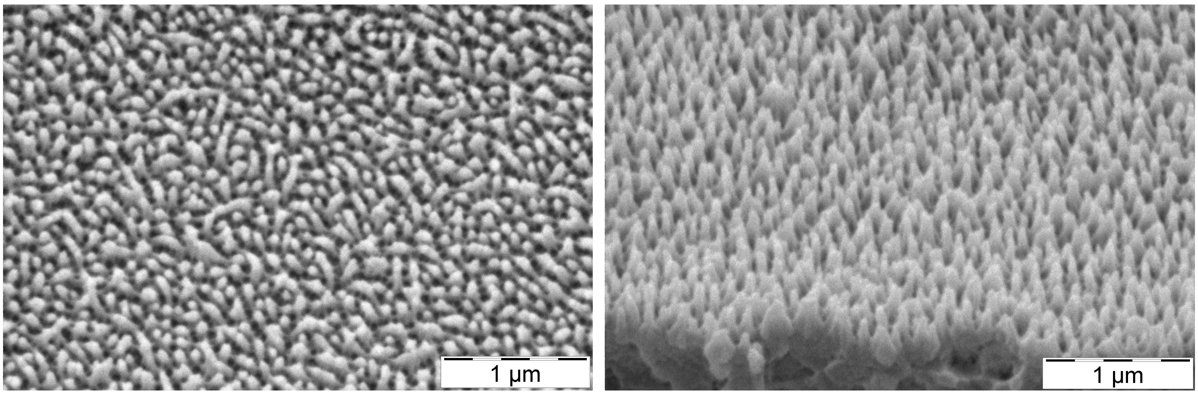

Fig. 5.19: *Scanning electron micrographs of plasma treated PMMA surface in top-view (left) and with 45° tilt (right), 6 kV, SE detector, magnification 30000×; $U_B = 120$ V, Ar-flow$= 14$ sccm, O_2-flow$= 30$ sccm.*

SEM. Beside the top-view image the representation of a tilted surface at a breaking edge provides complementary information, as can be seen from Fig. 5.19 for 300 s of treatment. From top-view, the topography exhibits pins as light dots, but also holes between the pins as black dots. The pins look like trunks that have roots (darker gray). The holes are spherical shaped and have about the same diameter as in Fig. 5.15 for 90 s of treatment. Instead, the trunks are hardly circular and sometimes seem to look like grown together. This apparent difference to the AFM images may be caused by heat impact from gold-sputtering or electron beam that both may result in a deformation of the freestanding pins.

The tilted surface represents the pin shape and the arrangement better than under normal incidence. The wide range of depth of focus reveals a true depiction for the whole pin altitudes. The pins have a cone-like habitus, and their orientation is normal to the surface. The picture is distorted due to perspective. To measure the correct pin height, it is necessary to correct the vertical scale or to stretch the image vertically as it was done for Fig. 5.19 (right). The typical pin height is in the range of 200 nm – 300 nm, which is much smaller than the thickness of the plasma sheath layer. However, it is still difficult to determine or even estimate the bottom of the grooves between the pins. A statement about the height distribution is demanding and may be better revealed from AFM analytics. The variable width of the pins becomes visible at the breaking edge. The FWHM of the pins can achieve values more than twice the average of about 90 nm.

What are the differences in structure formation for the different polymer surfaces? The plasma treated surfaces are depicted in Fig 5.20 (PC), 5.21 (PET), and 5.22 (PA) for comparison with that of PMMA (5.19). The manufacturing parameters are the same as previously stated in section 5.2 to achieve the best antireflection performance. The interpretation of the topology is supported by AFM imaging, see Fig. 5.23. Artifacts and distortion appear for PET, because of charging effects on the surface during measurement.

The top-view images and the 1 μm × 1 μm AFM scans have in common that they do not show any preferential lateral orientation. An optical isotropy (at normal incidence) should be the consequence which is advantageous over one-dimensional AR structures [4].

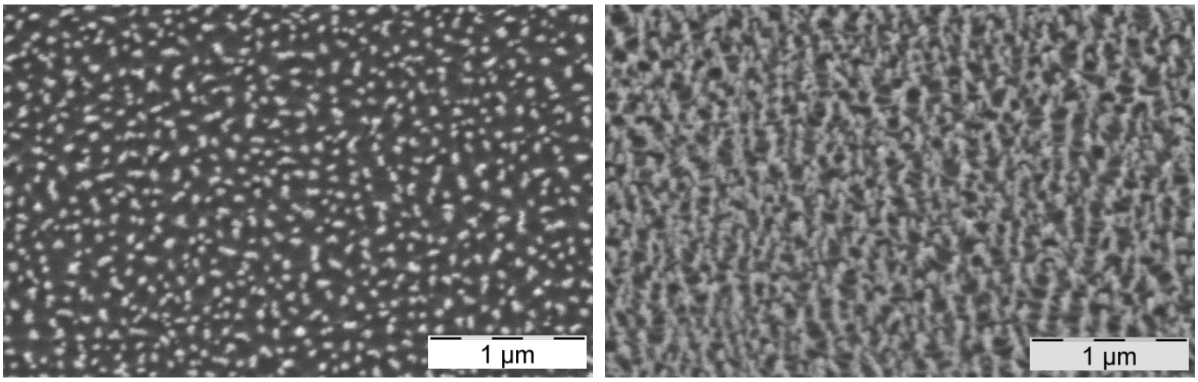

Fig. 5.20: *Scanning electron micrographs of plasma treated PC surface in top-view (left) and tilted by 45° (right), 10 kV, SE detector, magnification 30000×.*

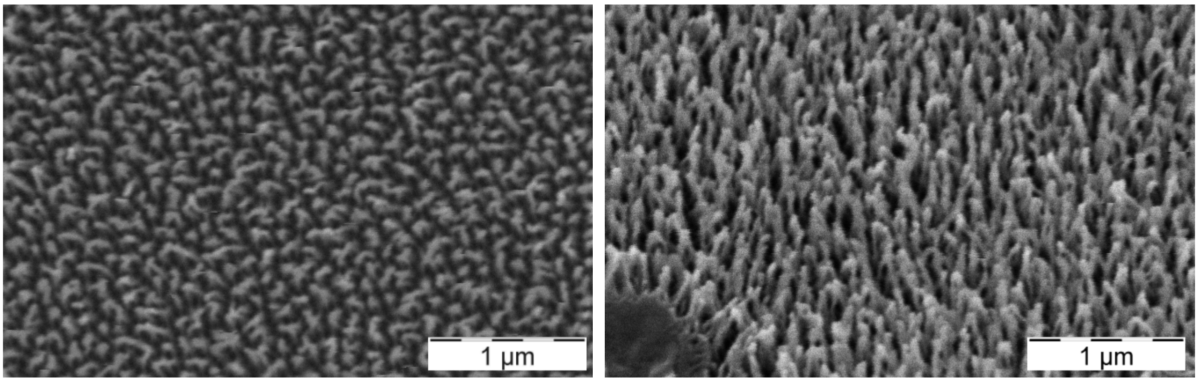

Fig. 5.21: *Scanning electron micrographs of plasma treated PET surface in top-view (left) and tilted by 45° (right), 10 kV, SE detector, magnification 30000×.*

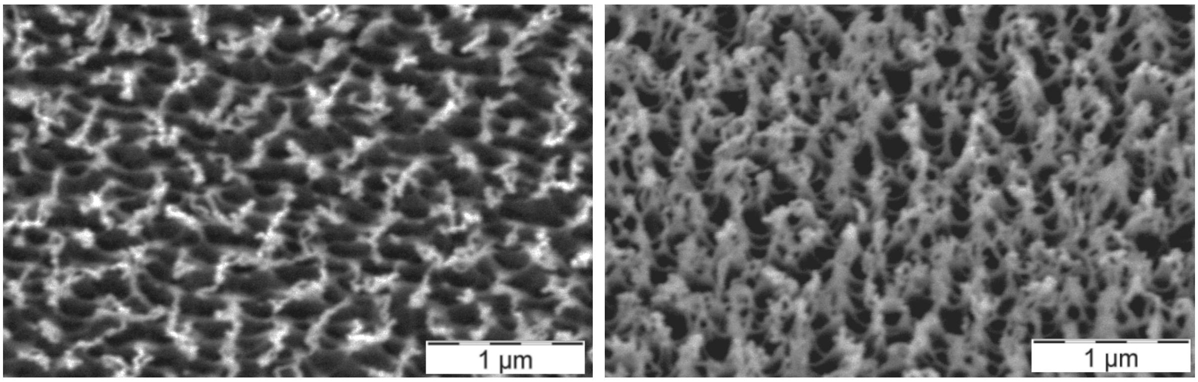

Fig. 5.22: *Scanning electron micrographs of plasma treated PA surface in top-view (left) and tilted by 45° (right), 10 kV, SE detector, magnification 30000×.*

---

[4] The anisotropy in optical properties is negligible for periodic 2D-structures as long as they fulfill the effective medium conditions of sec. 2.1 in all directions.

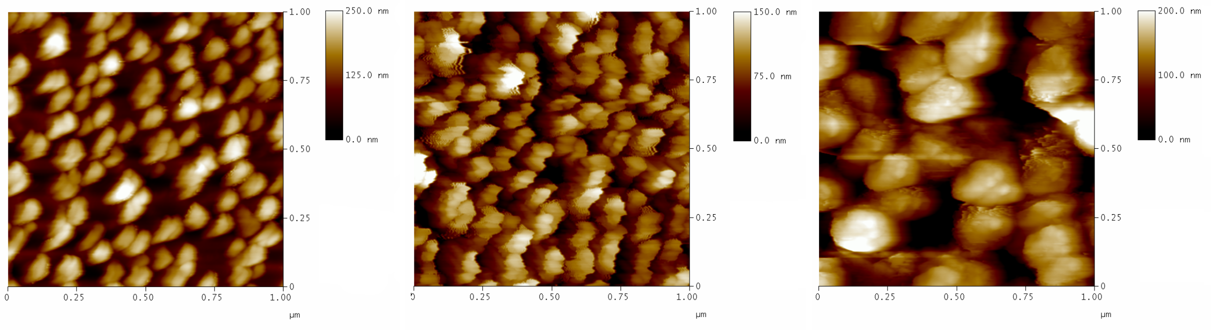

Fig. 5.23: 1×1 *μm^2 AFM-scans of PC (left), PET (middle) and PA (right) surfaces for best antireflection performance.*

Tab. 5.3: *Structure size, aspect ratio, and rms-roughness of PMMA, PC, PET, and PA surfaces based on* 1×1 *μm^2 AFM scans and SEM metrology.*

	L_C	**FWHM**	**height**	**aspect ratio**	**roughness**
Substrate	**AFM**	**AFM / SEM**	**AFM / SEM**	**AFM / SEM**	**AFM**
PMMA	150 nm	85 nm / 90 nm	135 nm / 250 nm	1.6 / 2.7	18.0 nm
PC	90 nm	55 nm / 50 nm	260 nm / 150 nm	4.7 / 3.0	54.5 nm
PET	85 nm	50 nm / 70 nm	190 nm / 325 nm	3.8 / 4.6	46.7 nm
PA	200 nm	120 nm / 130 nm	480 nm / 325 nm	4.0 / 2.5	53.5 nm

Tab. 5.3 summarizes the revealed pin sizes. As a first result, the lateral dimensions the AFM and the SEM are in good agreement. Obviously, the features on the PC and PET surfaces are thinner than for PMMA. Contrary, the pins of PA are broader than for the other polymers. PMMA and PET are rather similar in top-view. There are only few circular pins. The majority is jagged – for PET more than for PMMA. The PET texture is very compact, whereas there is more space between the pins at the PC surface – this is not clear from AFM imaging. The density of the structural elements has an effect on the volume filling factor in order to describe the optical properties of the surface by means of EMA.

Controversial results are obtained for the detected structure height. Actually, the values from AFM and SEM analysis do not match. In the case of AFM, the given value corresponds to the maximum height range in the scan area, whereas the values from SEM analysis results from measuring the height of several pins.[5] The SEM values of PMMA and PET exceed the AFM height that is expected for the incident of an aspect-ratio limiting AFM tip. This coincides with small and compact standing pins. Contrary, the AFM tip does not seem to limit the height measurement for the laterally big pins of PA and the isolated standing pins of PC. Here, the determination of the exact pin height from the SEM images is complicated. The pins of PA look rather curly, being jagged even along the sidewalls.

---

[5] Again, the difficulty is to determine the bottom of the grooves between the pins.

It is difficult to estimate the altitude of the base plane for the structured PC surface.

The highest measured value is suggested as the most likely one. Nevertheless, an exact determination of the structure height may not be important for a correlation with antireflection properties. The subwavelength nature causes an averaging for the incoming waves along several pins of different heights. Moreover, the macroscopic measurement of reflection causes a further leveling due to a finite spot size. The revealed height values should be rather considered as tolerance margins in the optical reverse engineering task.

According to the strong variation in height, specific aspect ratios of singular pins are not very helpful for characterization. The shape itself may be of more importance. PC is the only material that shows columnar pin shape having nearly perpendicular sidewalls ($\eta < 5°$), which indicate a strong anisotropic etching, as affirmed by a low etch rate. The cone shape of the PMMA and the PET structure is comparable, but the flanks of the PET pins are steeper ($\eta \approx 7°$) than that of PMMA ($\eta \approx 10°$). The half cone angle of PA ($\eta \approx 11°$) is close to that of PMMA. The transition zone between the trunks and holes, which was denoted previously as "roots", seems to be most distinctive for PA and is nearly absent for PC.

It is difficult to draw correlations between the pin shape and the results from etch rate measurements, because it must be considered that the processes, which led to the depicted surfaces, underwent different parameters and durations. Clearly, a higher U_B was necessary for PA (160 V) and PC (140 V) to achieve an adequate aspect ratio for a sufficient antireflection performance in a feasible time, since their slopes in Fig. 5.1 are lower than for PMMA and PET (both 120 V). Furthermore, the amount of oxygen was increased in order to accelerate the process. Nonetheless, the plasma-treatment time of more than 10 minutes gave rise to a high thermal load that may lead to an increment in lateral dimension due to enhanced surface diffusion processes, according to the Bradley-Harper model (eq. 3.10).

Fig. 5.24 shows what happens to the surface, if the ion's incidence angle is tilted with respect to the surface normal. This was achieved by tilting the sample with respect to the substrate holder. The drawn in coordinate systems demonstrate the interrelation between angle of incidence and declination of the pins. This result is independent from the rotation of the substrate holder, which points out the homogeneity of essential properties of the plasma sheath layer.[6] At the position of the tilted sample, the particles are extracted into the sheath layer and are accelerated perpendicular to substrate holder.

This result is a strong argument for the structure formation theory according to Oehrlein [17], since the formation of the subsurface damage region happens always normal to the ion bombardment. Contrary, the alignment of a pin structure in direction of the impinging ions was never observed in processes that have been successfully described by the Bradley-Harper model. In this context, the generation of waves, having an elongation that is still normal to the surface, rather than the

---

[6] Nevertheless, if the APS is understand as a point source for particle extraction, the ion density will decrease $\propto r^{-2}$ and far-reaching positions undergo lower ion bombardment and thus smaller etching rate.

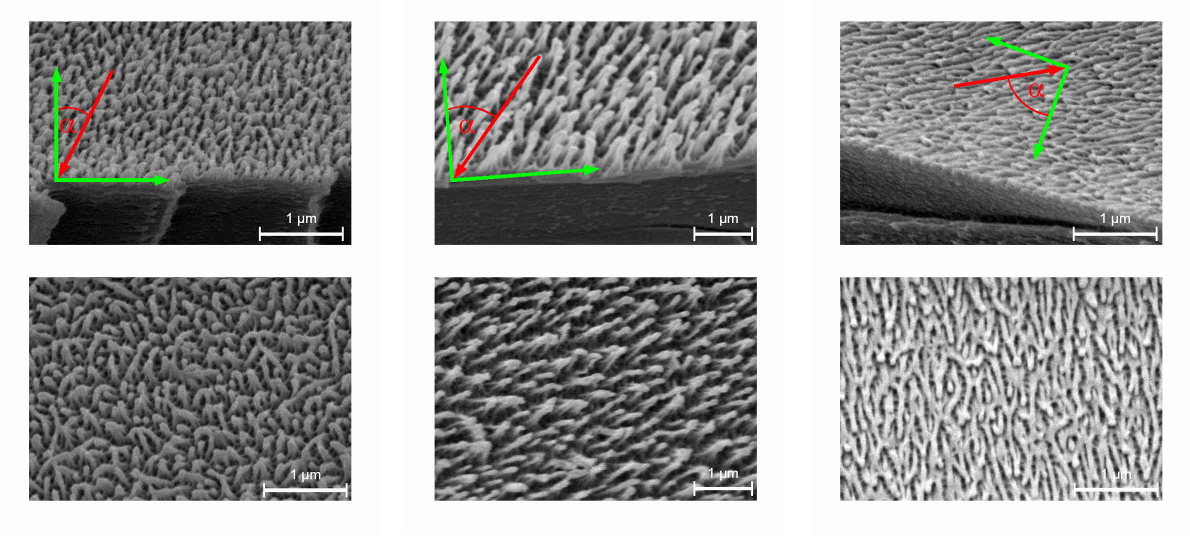

Fig. 5.24: *SEM-image of structured PMMA surfaces for* $30°$*,* $45°$ *and* $60°$ *(f. l. t. r.) angle of ion's incidence with* $45°$ *tilt (top) and in top-view (bottom).*

formation of inclined pins is discussed in literature.

As the pins are not aligned normal to the surface plane, a tilting angle comes arises between the beam of incident light and the pins, that introduces optical anisotropy. On the one hand, a polarization-dependent reflection may follow. On the other hand the subwavelength criterion may be violated in one direction. This behavior affects the application of plasma etching on curved or micro-structured substrates, such as lenses or DOEs. In case of DOEs, a blazed angle can be taken into account by tilting the surface normal relative to ion beam direction. Nevertheless, the advantages in spectral properties due to the broadband antireflection effect (no color impressions) even for non-normal light incidence are more obvious than possible disadvantages.

Starting from the SEM imaging of the breaking edge and the AFM line scan data in Fig. 5.25, the task is now to find analytic expressions that describe the typical (mean) pin profile sufficiently. Furthermore, the impact of the height distribution has to be considered. This preliminary work is necessary for optical modeling by RCWA or thin-film interference matrices (with subsequent calculation of the polymer's volume filling factor).

The pin profiles from Fig. 5.19 (right) and Fig. 5.25 suggest in the 1D-case (without loss of generality) a Gaussian shape $h(x) = \frac{1}{\sqrt{2\pi}\sigma} \exp\left(-\frac{(x-b)^2}{2\sigma^2}\right)$ with the peak at $x = b$ and a width of 2σ. The peak range of the pins is described well by this function, whereas at the bottom the fit becomes worse due to the asymptotic slope of the Gaussian distribution. An alternative approach may be the use of the periodic sine function $h(x) = A \cdot \sin(nx + \phi)$, which shows minima at each $x = (3\pi - 2\phi)/(2n)$. However, the peak's curvature differs from the groove's one. Here, the profile is described insufficiently by the sine function. The exponential-sine function $h(x) = A \cdot \exp(B \sin(nx + \phi) + C)$ is close to the shape of the Gaussian function and shows minima, which

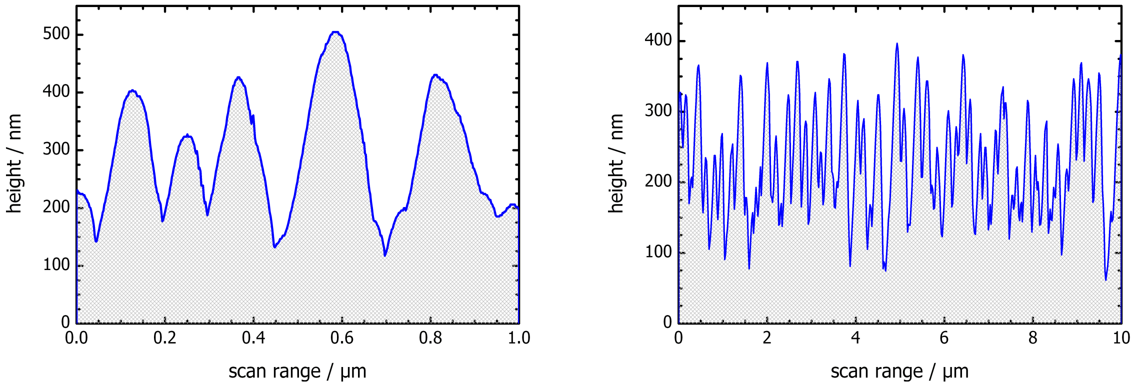

Fig. 5.25: *AFM line scans of a plasma-treated PMMA surface for an 1 μm (left) and a 10 μm (right) scan range.*

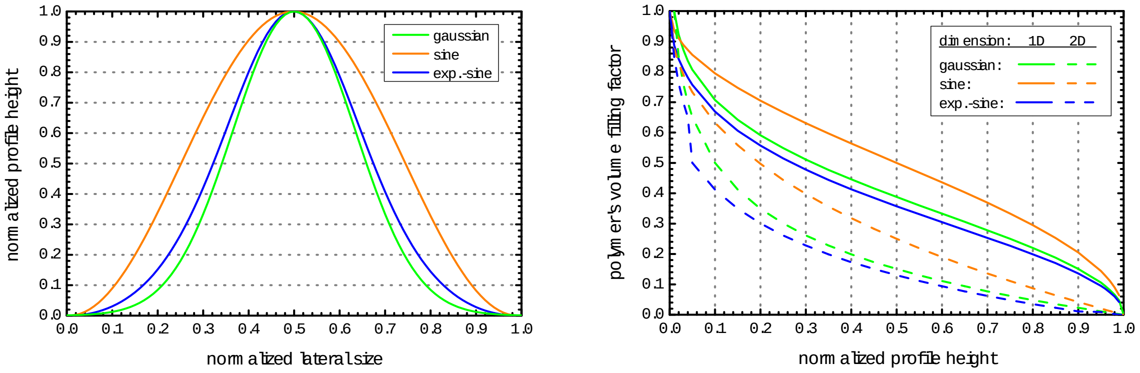

Fig. 5.26: *Analytic functions that are adequate to describe the shape of an individual pin (left), and the resulting filling factor profiles for one- and two-dimensionality (right).*

can be designed relatively sharp by setting B and C.

The three normalized functions and their corresponding volume filling factor profiles ν are plotted in Fig. 5.26. A periodic continuation (1D) and a simple cubic (sc) lattice of cylindric pins (2D) is assumed.[7] In this context, a pin of constant radius – a column – leads to $\nu =$ const., while a cone causes a linear function, with respect to the height. Thus, the non-linear slope of the discussed functions results in a non-linear ν-profile. Because of the asymptotic slope of the Gauss function, ν is not defined for $h = 0$. It is straightforward, that the bigger the area below the pin-describing curve the higher the corresponding ν. In contrast to the 1D-case, the 2D-profiles do not show inflection points, but a steeper gradient at the lower boundary and a shallower curve at the upper limit.

The difficulty with forming a filling factor profile out of singular pins is its relation to a very regional surface characteristics that may not be representative for the total topology. A better consideration of the stochastically distributed pin properties arises from the statistics. Fig. 5.27 shows the histograms

---

[7] The topology suggests a hexagonal arrangement as the most likely representation of the stochastically distributed pins leading to a slightly higher ν.

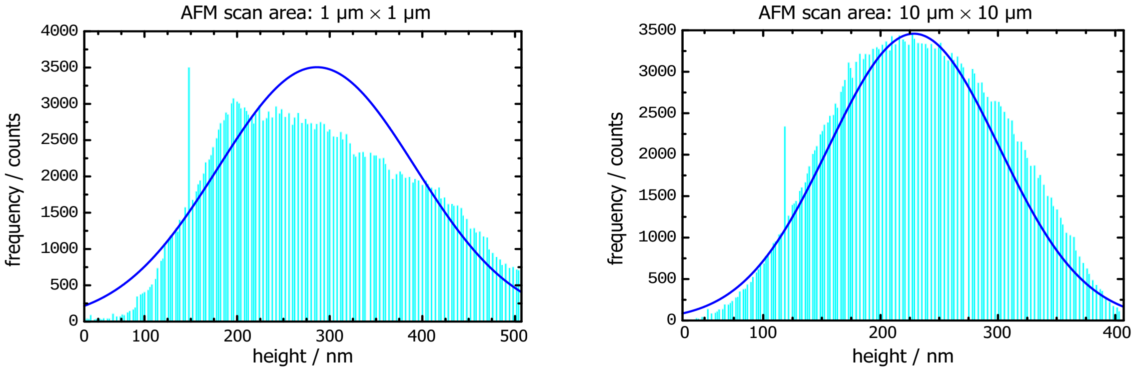

Fig. 5.27: *Histograms of measured height distribution for a 1 μm × 1 μm scan and a 10 μm × 10 μm scan for PMMA surface plasma-treated for 600 s with bias voltage 120 V. (blue dashed lines: Gaussian distribution).*

of two AFM-scans of the same surface after plasma treatment. The length of the bars is equivalent to the number of data points (pixels) of a detected height within the scan range. The most frequent is given for 200 nm (230 nm) for a 1 μm × 1 μm (10 μm × 10 μm) scan. The height range differs due to a variable scan speed, which is usually slower for a higher resolution, and the considered area for the 10×10 μm^2 scan. The histogram of the small scan range is more asymmetric than that of the large scan area according to the Poisson distribution, which can be well-described by the Gaussian (normal) distribution only for a large number of measurement points. Furthermore, a reason for the infrequent appearance of small heights may be found in the aspect ratio of the AFM tip that does not allow for a sufficient penetration of the narrow grooves as explained in sec. 4.4.2. The solitary bar at 150 nm is caused by artifacts. The integration of frequency with respect to the detected height and the subsequent normalization – the scan range as the 2D footprint and the maximum height as the profile thickness – yield again the z-dependent volume filling factor.[8]

An approach for an analytic expression of the filling factor profile from AFM statistics is given by the integration of the Gaussian height distribution which reveals the error function (Gaussian integral): $\mathrm{erf}(x) = 2/\sqrt{\pi} \int_0^x \exp(-\tau^2)\mathrm{d}\tau$. The profiles of Fermi function [183], arc tangent function, and exponential sine function [184] are appropriate beside erf(x) and are shown on the LHS of Fig. 5.28. The quintic polynomial was proposed by Southwall [185] as a (refractive index) profile with very a broad antireflection performance. A more complex profile especially for 2D tapered subwavelength gratings, using Bessel functions, is given in [186].

Fig. 5.28 (right) presents the volume filling factor of air ν_{air} for three plasma treatment times and two scan areas. The polymer's volume filling factor ν_{PMMA} follows by horizontal flipping of the plots, since $\nu_{\text{air}} + \nu_{\text{PMMA}} = 1$. The profiles are characterized by a nearly linear slope in the middle and

---

[8] It may be helpful to imagine an unique pin with the lateral dimensions of the scan range and the maximum measured height within it.

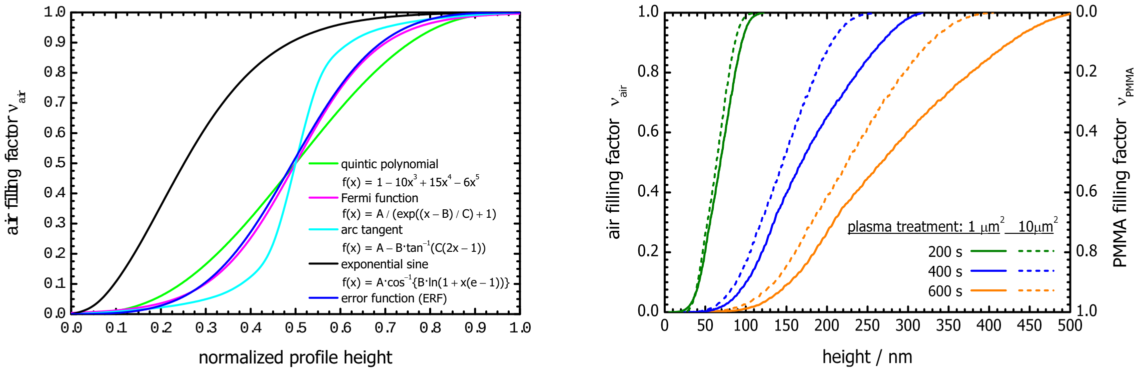

Fig. 5.28: *Analytic functions that are adequate to describe the filling factor (left), and filling factor vs. profile height for three plasma treatment times and two scan areas (right).*

a flattening at the boundaries. The relevance of these boundary zones gains with treatment time, which implies an ongoing broadening of the height distribution. At the same time, the height of the profiles increases with duration in accordance with the pin growth. In this context, a distinction in the profiles' shapes becomes more and more obvious for the different scan ranges. The discrepancy in height obtains 100 nm for the 600 s treatment. The non-gaussian height distribution of the 1×1 μm^2 scans leads to an asymmetric plot, whereas the plots of the large scan areas are rather symmetric relative to their inflection points.

It was found that the differing shapes are probably a reason of a different etching behavior that comes along with material specific properties, like high carbon content or a high resistivity against oxidative decomposition. The initiation from contamination is more likely than from small-scale roughness, since the sputter yield is low in comparison to the chemical etching. A steady state of roughening and smoothing, which would lead to a time-invariant pin shape during erosion, was not found. As long as the pins are growing, the Bradley-Harper model is suitable to only a limited extent. The pin shape was described by analytic expressions, but in order to consider the stochastic distribution of the main feature dimensions a statistical analysis is recommendable. A nonlinear volume filling factor profile follows in both cases.

5.4 Reverse engineering from optical spectra

Now, the task is to correlate the properties of surface features with the recorded optical spectra. Firstly, it is essential to know which pin dimensions cause the reduction in reflection or are advantageous for the bandwidth of transmittance increase. Secondly, reverse engineering from optical spectra provides a non-destructive way for surface characterization.

The knowledge of the materials' optical properties (n, κ) is always needed for establishing a sufficient correlation of structure properties and spectral characteristics. These quantities have been

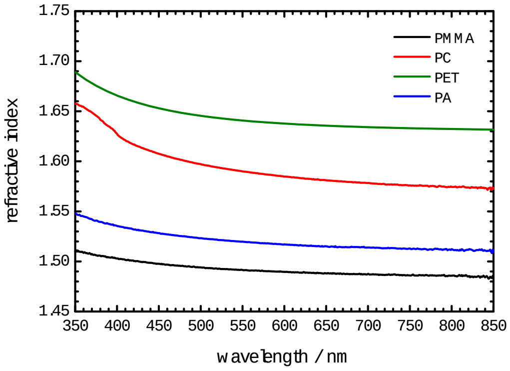

Fig. 5.29: *Refractive index against wavelength for the investigated polymers.*

determined for the tested polymers from the transmittance and reflectance spectra of plain (untreated) samples. The optical loss of the 1 mm (50 μm) thick substrates is below the accuracy of measurement of 0.2% in the wavelength range 400 nm – 850 nm, which implies an extinction coefficient below $5 \cdot 10^{-4}$. Thus, κ is negligible for further use in the optical modeling of the surface structures. The dispersion is given in Fig. 5.29 for the investigated polymers. The refractive index ranges from 1.49 (PMMA) to 1.64 (PET) at $\lambda = 550$ nm.

A correlation between pin shape and reflection is drawn rigorously by the coupled-wave approach. The convergence with respect to the number of considered Rayleigh orders was tested at singular wavelengths for different aspect ratios. The RCWA method converges fast, since the used materials are dielectric, and have a n' comparably close to that of air. The so-called truncation run revealed a relative deviation of 0.5% in reflectance between the 8^{th} and the 9^{th} order for an aspect ratio up to 2.5:1. Thus, the absolute precision of simulation ($\pm 0.002\%$) considering 8 Rayleigh orders is superior to the accuracy of measurement ($\pm 0.2\%$) of the intensity of reflection.

Fig. 5.30 demonstrates the effects of height and period variation on the reflectance for a 2D array of conical-shaped pins. Since absorption has been neglected, the transmittance spectra vary in analogous manner ($T = 1 - R$). In consistence with the subwavelength conditions of sec. 2.1, a coupling of light into higher diffraction orders was not observed for normal incidence.

When setting the period to $\Lambda = 100$ nm in accordance with a typical feature size, the increase in structure height causes decrease in R in a broad spectral range. A significant reduction within the VIS region is already obvious from $h = 100$ nm on, which implies a structural aspect ratio of 1:1. The decrease is highest at small wavelengths, leading to a residual reflection of the structured surface of about 0.4%. The range of residual reflection extends to the whole VIS for $h = 300$ nm, which means an aspect ratio of 3:1.

Contrary, a variation of the period in subwavelength scale does not lead to notable changes in reflection for a given height $h = 250$ nm as long as the period is much smaller than the wavelength of interest. The aspect ratio ranges from 2.3:1 ($\Lambda = 110$ nm) to 3.3:1 ($\Lambda = 75$ nm). A decrease in

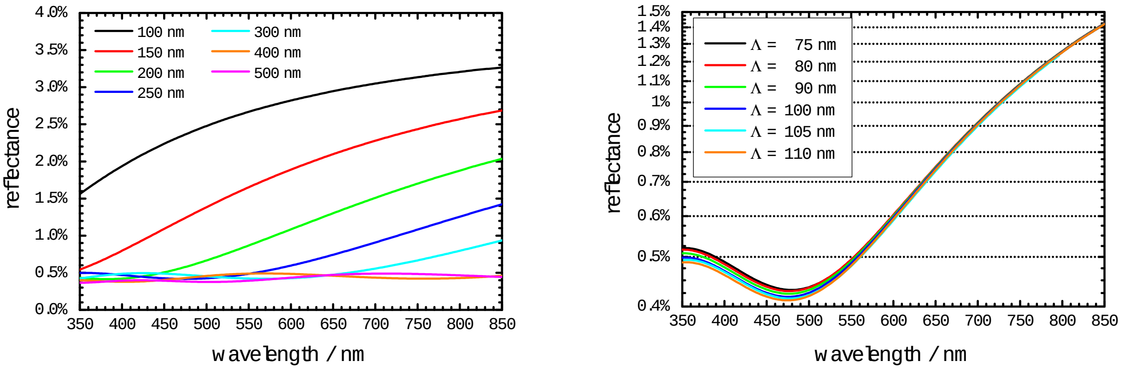

Fig. 5.30: *Reflectance of a structured PMMA surface as a function of structure height (left) and period (right), calculated by RCWA.*

reflection, while expanding the period, is only visible for small wavelengths.

Both, the residual reflection and the small changes in R due to period variation, are indications of the limits in simulation. In addition to the convergence issue, the accuracy is limited by the approximation of the conical pin shape as a stack of 10 homogeneous layers which implies no infinitesimal sharp tip, but a tip area of 0.15%Λ × 0.15%Λ.

What are the consequences of the pin's shape on the reflection of the structured surface? Knowing from the AFM and SEM analysis the conical shape is rather the ideal case. Fig. 5.31 compares the reflectance spectra of different pin profiles, that are aligned in a 2D array of the same period ($\Lambda = 100$ nm) and height ($h = 300$ nm). It becomes apparent, that the shape affects the bandwidth of the spectral range of antireflection. The reflectance of the columnar pins ($\nu_{\text{PMMA}}(h) = const.$) exhibits the full amplitude from $R = 0$% to $R = 3.8$% (plain PMMA surface), which is equivalent to the spectral characteristics of a homogeneous layer like that in Fig. 2.3. The exponential-sine taper represents a Gaussian pin shape, whereas the bearing profile uses the histogram data from the AFM analysis (1×1 μm^2). The residual reflectance of a Gaussian pin structure is very similar to that of an array of cones. The shift in the spectral position of the extrema corresponds to a different optical thickness due to the nonlinear filling factor gradient. The pins from bearing analysis are broader on top than the Gaussian peaks, and have therefore higher amplitude in reflectance. Again, the difference in optical thickness causes a displacement of the extrema.

In sum, the calculation using RCWA gives a correlation between shape dimensions and spectral characteristics of subwavelength-structured surfaces. Nevertheless, this method is not practical for the reverse engineering of the measured spectral data, because of the stipulation of periodicity and the difficult implementation of the stochastic height distribution. Moreover, the algorithm is very time-consuming, impeding the applicability for fast evaluation of *in situ* monitoring data. Therefore, the speed of homogenization by effective medium theory and the subsequent calculation by matrix formalism for homogeneous layers gains over the rigorous approach.

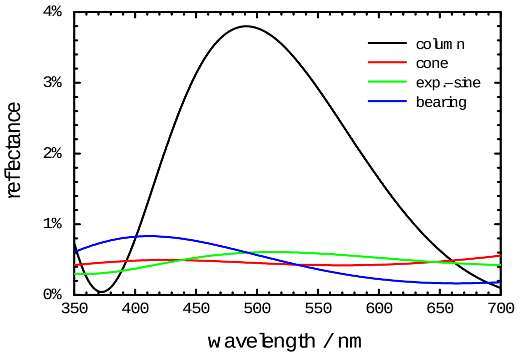

Fig. 5.31: *Reflectance of a structured PMMA surface for different pin shapes, calculated by RCWA.*

The volume filling factor profiles $\nu(h)$ have been transformed into effective refractive index gradients $n_{\text{eff}}(h)$ using eq. (2.7) in 1D geometry ($\mathbf{E}||\mathbf{K}$) and eq. (2.8) for the 2D case. Fig. 5.32 shows them for the parameterized profiles of the AFM analysis (Figs. 5.26 and 5.28). The left diagram presents the results that have been obtained directly from the pin shape, whereas the plots on the right follow from the analytic expressions of the AFM statistics. Because the mixing equations do not provide proportionality between n_{PMMA} and n_{eff}, the transformation is non-linear which has been already expected from Fig. 2.1. The nonlinearity causes an underestimation of the gradients' middle sections, whereas an overestimation follows at the boundaries of the profiles. Because of the comparably small differences in n for the involved materials, this effect is hardly noticeable, but is more present in two dimensions than in the 1D case.

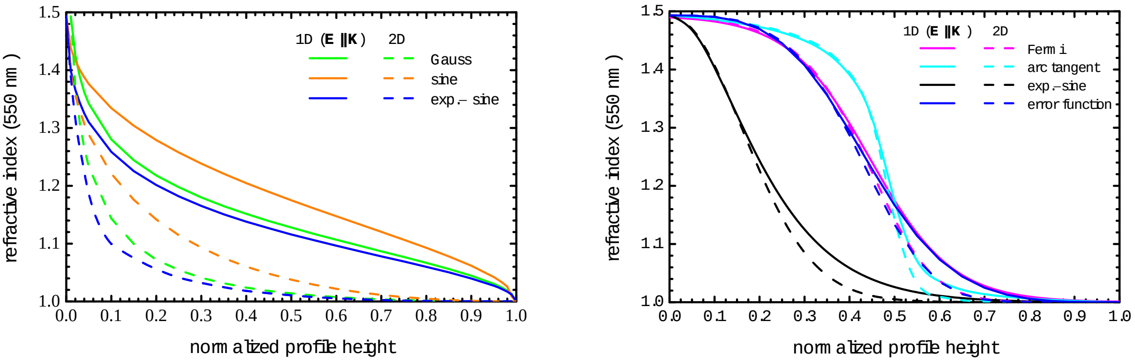

Fig. 5.32: *Effective refractive index for the filling factor profiles (left) of Fig. 5.26, and for the analytic expressions describing the data from AFM statistics (right) of Fig. 5.28.*

The transmittance and the reflectance spectra from Fig. 5.5 were set as target for the reverse engineering procedure. The number of free-variable parameters must be restricted in order to achieve a sufficient convergence of the optimization algorithm, since R and T are the only quantities for fitting. With the help of well-chosen (consistent) assumptions, the parameter range can be constrained and

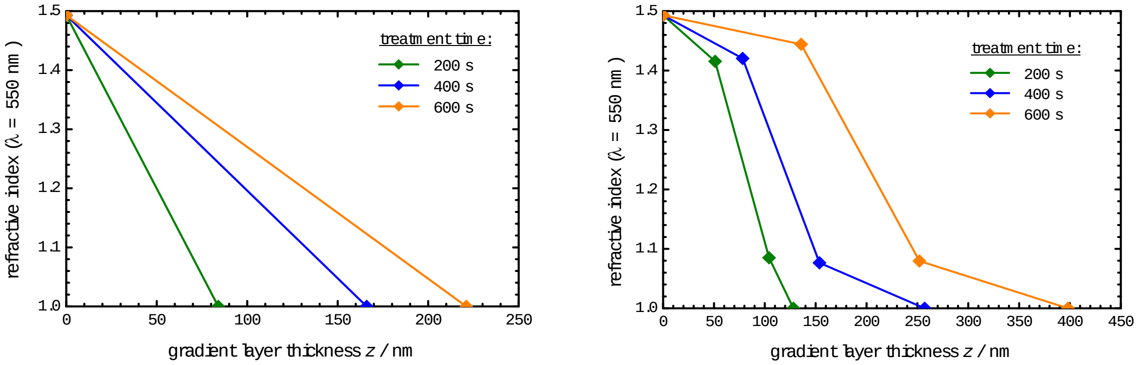

Fig. 5.33: *Re-engineered linear gradient (left), and 3-step gradient (right).*

a few supplemental variables can be added to the optimization task. An approximate pin height has been used from SEM and AFM analytics and consistent values of the refractive indices of the pure materials were set at the boundaries to the substrate and to the ambient material.

Starting with a linear gradient, the thickness d is the only parameter to be varied for optimization, since the refractive indices at the boundaries are fixed: $n(z = 0) = n_{\text{PMMA}}$ and $n(z = d) = n_{\text{air}} = 1$. The software package Film Wizard [56] divides the linear gradient into homogeneous layers (5% of total gradient thickness $\widehat{=}$ 20 sub-layers) by equidistant fragmentation.

Gradient thicknesses of 84 nm $(MF = 0.17)$, 166 nm $(MF = 0.23)$, and 221 nm $(MF = 0.23)$ have been obtained for treatment times of 200 s, 400 s, and 600 s, respectively and suggest an almost linear pin growth with time. The refractive index gradients are plotted in Fig. 5.33 (left) for a wavelength of 550 nm. The systems of equations are over-determined. The gradient's shape does not match with the estimated ones from SEM and AFM, and the revealed thicknesses are smaller than expected, because the considered conical shape is more efficient in refractive index matching than the rounded pins in real. Moreover, the transition zones from the statistical height distribution are unconsidered in the refractive index gradients.

The mismatch between the target and the calculated spectra increases with process duration, but is close to the accuracy of the measurement. Firstly, this is an effect of emerging scatter losses that cannot be considered by EMA and secondly, this is caused by the rising influence of the non-linearity of the profile for long plasma treatment times.

The consideration of nonlinearity leads to an increase in geometrical thickness d_{geom}, while the optical thickness $(d_{opt}(\lambda) = n(\lambda)d_{geom})$ is staying constant. Inserting sampling points into the gradient allows for a non-linear shape. Each node introduces two additional degrees of freedom: the position h_i within the gradient and the refractive index $n_i(h_i)$ at its position. The originally linear gradient splits into two new linear ones that are linked continually together. Now, constrains become useful for the sampling points: (I) The refractive index is in the range of the pure materials. (II) In the case of two or more sampling points, the slope should be monotonic, restricting the position

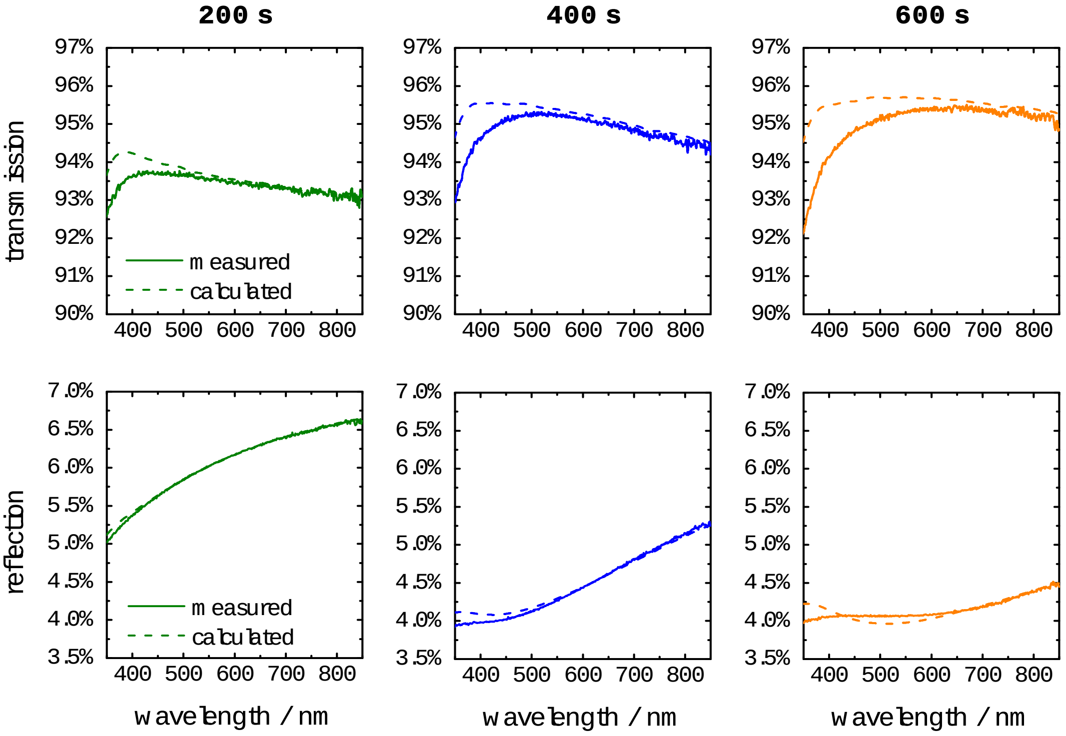

Fig. 5.34: *Comparison of target (measured) spectra and re-engineered (calculated) spectra using the 3-step gradients from Fig. 5.33.*

within the gradient.

With the use of two additional nodes, five parameters (n_1, z_1, n_2, z_2, d) slip in the optimization task, implying an under-determined system of equations.[9] The double bend shape of the revealed 3-step refractive index profiles is obvious in Fig. 5.33 (right). The intervals of the gradient that are used for the transition zones are about one third of the total thickness. This segmentation stays nearly constant during the progress, denoting a broadening in stochastic height distribution of the pins. The total thicknesses of the re-engineered gradients are 128 nm, 257 nm, and 398 nm, which demonstrate again the linear increase in pin height with time. With introduction of nonlinearity, the profile thickness enlarges by a factor 1.5 for 200 s and 400 s, and nearly doubles for 600 s.

The measured reflectance and transmittance spectra are compared with the calculated ones in Fig. 5.34 for the three process durations. The mismatch in the UV region due to upcoming scatter losses lead to an increase in the merit functions of the spectra fits with time. Nevertheless, the MF decreases slightly to 0.14, 0.22, and 0.22 compared to the linear gradient. This underlines the fact that main broadband antireflection performance is already achieved by a linear gradient, and the introduction of transition zones refines the result only slightly. Moreover, if the MF has a lower limit,

---

[9] Introducing only one additional sampling point (two-step gradient) results in a gradient that has no inflection point, which was expected from AFM analysis.

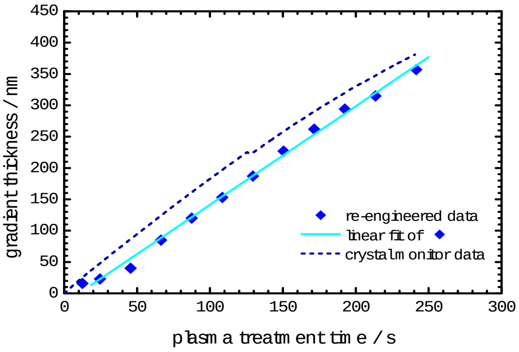

Fig. 5.35: *Re-engineered gradient thickness from in situ transmittance spectra in comparison with the ablated thickness measured via quartz crystal monitoring.*

because the effective medium theory cannot handle the occurring scattering losses correctly, it would be unpromising to increase the number of parameters (nodes) in order to describe the gradient in a better way.

The results of the 3-step gradients emphasize to use parametrized refractive index profiles for reverse engineering, having a slope like that from the AFM bearing analysis. It is suggesting to utilize the error function, Fermi function, the quintic polynomial, or the arc tangent function in Fig. 5.32 (right). Since the shape is determined completely by the analytic expression, the gradient's thickness is again the only variable in the optimization task. More shape-describing parameters (asymmetry, steepness) will be used in future to improve the results of spectra fits.

The reverse engineering task of *in situ* recorded data is more crucial, since only the transmittance spectra are available so far ($R = 1 - T$). Thus, the restriction to the thickness as the solely varying parameter for optimization is essential to ensure a sufficient convergence. The profile was modeled utilizing a symmetric Fermi function $\nu(h) = A/(\exp((h - 0.5)/0.1) + 1)$ for the filling factor which expands as the thickness increases.

Fig. 5.35 shows the calculated thickness as a function of plasma treatment time for the process, that was already discussed in 5.2. The *in situ* recorded spectra have been already presented in Fig. 5.7 (left). The temporal resolution of about 3.5 s is given by the rotational speed of the substrate holder, since a transmission measurement is triggered only once per turn. The interval was extended to 21 s (six measurements) without a drastic loss of information. The period has been halved in the early stage. In addition, the etched thickness, revealed from quartz crystal monitoring, is drawn into the diagram. Its resolution is better than 0.1 s. Both progresses are linear from 30 s of treatment time on.

At the early stage, the computed (gradient) thickness increases slower than the value from quartz crystal measurement suggests. The verification, that the structure formation has already started at that time, has been revealed by the AFM analysis in sec 5.3. The difference between the two thickness values is in average 35 nm and its constancy for most of the plasma treatment time is remarkable, since only the thickness from optical determination considers the filling factor of the pin structure. This is not the case for the quartz crystal data, which assumes a plain erosion. The findings are consistent, if the etching happens all over the surface and not solely in the grooves. The etching is slower on the tip of the pins and faster for the spacings between, which leads to an additional lowering of the (mean) surface plane with respect to the original level. The separation of the etch rate into a homogeneous (lowering) and an inhomogeneous (structure forming) fraction has been described in [63]. In particular, a total lowering of the mean structured surface plane by 180 nm was revealed for this experiment.

The accuracy of calculation from optical data is limited in the stages, where the size of the structures has only minor effects on the recorded spectra. This is the case in the beginning, where the effects should be noticable in the UV region. The same happens for structures that have a too large pin height (gradient thickness) and lead to a non-changing high transmittance "steady state" in the observed spectral range. However, since scattering occurs, the reverse engineering task has to be stopped prior to this moment. The increasing losses in T, that cannot be assigned definitely to a change in R, A, or S, adulterate the result of reverse engineering. In general, it is recommended to utilize the value from crystal monitoring as an initial estimation for the optimization task in order to force the convergence. For more accurate spectral investigations at the early stage the optical monitoring system will be improved regarding time resolution (shorter integration time), sensitivity in the ultraviolet wavelength range (deuterium lamp), and consideration of the reflection to incorporate changes in absorption and scattering.

Being able to interpret the *in situ* optical spectra helps to understand the effects of parameter variation. The change in U_B above 100 V does not lead to a significant variation in peak transmittance which implies the same total height (gradient thickness) and aspect ratio (gradient shape) of the pins. In the case of $U_B < 90$ V the lower transmittance increase is caused by smaller gradient thickness which correlates with the findings from PSD analysis (cp. Fig. 5.17). A reason can be found in a less anisotropic process for low-energetic ions due to a smaller sputter erosion or as a result from a thinner superficial modification zone. The decrease in T_{mean} due to scattering is a size effect and becomes steeper with increased U_B. The fast lateral growth causes a sooner violation of the subwavelength criteria.

The variation in oxygen flow does not cause a change in peak transmittance. Consequently, the same gradient thickness – or pin height – is achieved. Even more, the optical losses are on the same level, which means no additional absorption from a lack of oxygen at small flows and no additional scatter losses due to violation of the subwavelength criterion. The ladder implies the independence of the aspect ratio on oxygen fraction. This is in agreement with Oehrlein [17], if the thickness of the modified subsurface region does not vary. With presence of reactive oxygen the erosion on top of the layer increases, while the generation in the subsurface zone stays constant. Now, the former process defines the thickness, which should be smaller than the penetration depth of the ions.

The erosion behavior changes with the absence of oxygen. Now, it is mainly governed by the sputter yield of the argon ions that is $7\times$ lower than that of oxygen ions and is smaller by orders of magnitude than the chemical decomposition. Thus, the subsurface region is thicker, because the erosion at the surface is slower. The feasible aspect ratio decreases with pin height, when the thickness of the subsurface region increases. Consequently, the low structure height does not lead to noticeable transmittance increase in the VIS range. In addition, the absorption is higher, since the absence of oxygen result in a higher carbon fraction at the surface.

The question is, if argon is essential for the structure formation process at all. In order to hold up a certain modification zone, the impact of the energetic argon ions may be necessary. Additionally, the sputter erosion has to be taken over by oxygen ions. The required penetration depth can be achieved by an increased ion energy, and the necessary sputter yield can be compensated by a higher ion flux. Both methods result in an elevated heat impact and cannot be realized with the Advanced Plasma Source. The changeover to a pure oxygen plasma process was recently mentioned in literature [19] by using an alternative plasma generation concept, but without a quantification of the obtained transmittance.

Increasing the working pressure while maintaining the argon-oxygen ratio leads to a reduced peak transmittance which has to be found again in a lower aspect ratio of the pins. The additional amount of argon atoms can only indirectly cause chemical reactions, but transfer most of their kinetic energy into heat and the damage of the subsurface region. The lowering of peak transmittance is caused by a sooner occurrence of scatter losses in the short-wavelength region from an increased lateral pin size. This implies a direct correlation between the effective period and heat impact. But, this effect is not in agreement with eq. (3.10) that results from Bradley-Harper model [16]. More detailed investigations have to be done in order to prove the thermal impact from ions and from IR radiation of the plasma source on the lateral size of the pins. Both quantities are significant lower at small pressures and low bias voltages (discharge power). Contrary, a fast process compensates a long term heating.

The reverse engineering procedure was exemplified for the structure formation on PMMA surfaces. The results can be assigned to the spectral properties of the other plasma-treated polymers as well. In the case of PC, the gradients' shape will exhibit a distinctive bending point, which is caused by the low filling factor of the relatively freestanding pins. In combination with a material-specific high reflectance of the plain substrates, the antireflection efficiency is rather poor. The rigorous coupled wave approximation was used to reveal the main correlations between effective structure shape and spectral properties. The subwavelength scale and the stochastics recommends the use of the effective medium theory in order to determine quickly the basic structure information. Parameterized gradient's, which consider the stochastic height distribution, are well suited for description.

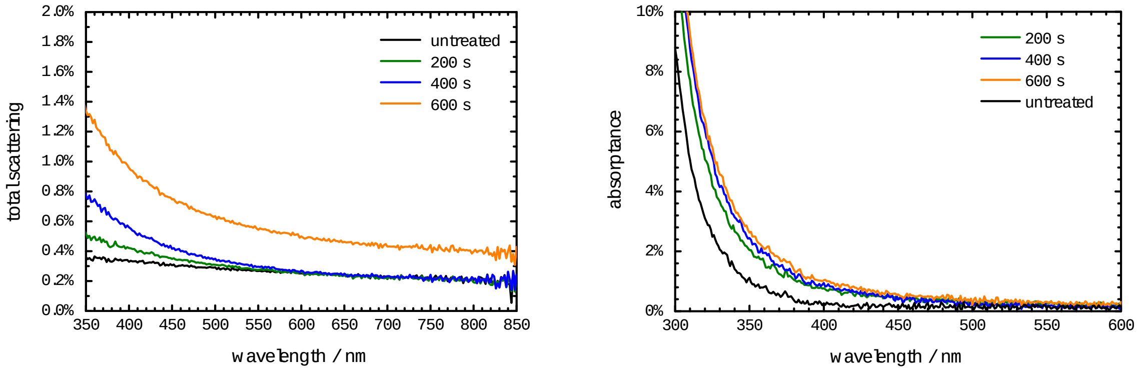

Fig. 5.36: *Total scattering as a sum-up of forward and backward direction (left), and calculated absorptance spectra using* $A = 1 - R - T - S$ *(right).* $U_B = 100$ *V, Ar-flow=* 13 *sccm, O*$_2$*-flow=* 30 *sccm.*

5.5 Origins of optical loss

As already mentioned, scattering is a substantial loss mechanism that is introduced to the polymer surface by plasma treatment. This section focuses once more on the temporal evolution during the PMMA etching. It is expected that the other investigated polymers show in principle the same behavior, corresponding to their typical pin shape and pin alignment. With the quantification of the scatter losses, the absorptance A is also available. In general, the statistical distribution in pin sizes and the stochastic arrangement enhance the disposition to surface scattering, and the analysis of the corresponding spectra may allow for a non-destructive and contactless characterization of structural properties. Furthermore, the impact of other sources of scattering is investigated.

The total scattering was measured for the same set of PMMA samples as in sec. 5.2 in addition to the transmittance and reflectance spectra from Fig. 5.5 for the single-side plasma treatment. The total scattering as depicted in Fig. 5.36 (left) is below 1% in the VIS range up to 600 s of treatment. The main increase is registered between 400 s and 600 s, where the scattering nearly doubles for the entire spectral range. As a first consequence, the optimal process stop time for application with this set of plasma parameters (cp. caption of Fig. 5.36) is close to 400 s in order to avoid significant scatter losses, which reduce the specular transmission performance.

The calculated absorptance $A = 1 - T - R - S$ is presented in Fig. 5.36 (right). The spectra are dominated by the presence of the absorption edge around 300 nm. A of untreated PMMA is below the accuracy of measurement (0.2%) in the VIS range, but with plasma treatment the absorption increases noticeable. The most significant increment is already observed for 200 s, raising the value by 0.5% at $\lambda = 400$ nm. Further on, this progress slows down, obtaining 1.0% at $\lambda = 400$ nm for 600 s.

There are three possible origins of the loss. (I) The upcoming antireflection performance of the front surface leads to a better coupling of light into the substrate. Since the absorptance of a material

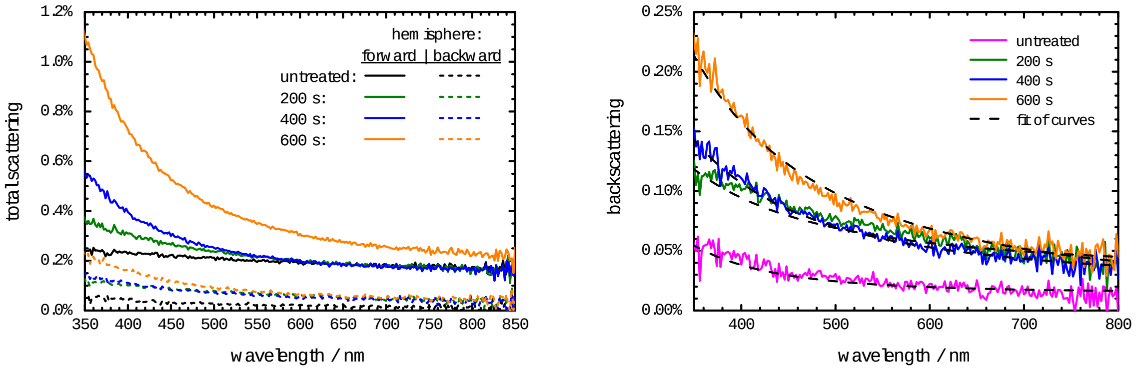

Fig. 5.37: *Total forward and backward scattering of the plasma-treated PMMA surfaces (left) and analysis of backscattering spectra by fitting with eq. (4.6) (right).*

is defined from Beer-Lambert law as $A(z) = -\ln(I(z)/I_0) = \alpha z$, its value increases along with the light intensity I_0. [10] (II) UV radiation emitted from the plasma can generate bulk defects, which would cause a continuously growing A value with duration. (III) The plasma-polymer interaction, especially the decomposition due to selective ablation, forms a surface-covering carbon-rich layer that has a higher extinction coefficient than the substrate. An argument for the third option comes from the *in situ* spectrophotometry where a significant decrease in transmittance was detected within the first 15 seconds. A detailed progress of the A is given in [18]. A carbon-rich layer correlates with the results from Monte Carlo method and from the model of Gokan [111]. However, assuming a layer with a thickness from MCM of $1-2$ nm that is composed purely of carbon (using the refractive index of graphite) would lead to much higher absorption of the complete optical system. Moreover, such a surface would exhibit a reduced electric resistance according to [101], which was not detected with standard measuring equipment.

A detailed investigation of scattering is given in Fig. 5.37 (left), which presents the total (integrated) scattering spectra of PMMA in forward (TS$_f$) and backward (TS$_b$) hemisphere. The scattering in forward direction dominates, while TS$_b$ is below the accuracy of measurement. This is in agreement with the subwavelength criterion of eq. (2.6) which is violated first for the forward direction in consideration of the polymers refractive index. An increase in scattering is obvious with process duration, especially for short wavelengths. Until 400 s TS$_f$ increases only below 550 nm. Afterwards an overall increase is observed. The main increment in backward direction is already observed for 200 s and additional scatter losses below 500 nm appear for 600 s. The backscattered light intensity is examined once more in Fig. 5.37 (right), fitting the plots by use of the eq. (4.6). The temporal evolution of the coefficients is summarized in Tab 5.4.

---

[10] In fact, this is the standard practice for generating a good absorber: Coupling as much light as possible into a sufficient absorbing material. The realization was shown in [27] by overcoating the plasma-treated surface with a high absorbing metal and illumination of the resulting interface from the dielectric backside (the polymer).

Tab. 5.4: *Coefficients of fit with the use of (4.6).*

Time / s	X **/ nm**	Y **/ nm**	Z
0	156	0.6	0.015
200	130	91.1	0.002
400	157	100.2	0.001
600	158	141.3	0.002

The coefficient X, standing for the weighting of the impact of the subwavelength features due to the Rayleigh term, is nearly constant with time. Obviously, the pin structures themselves do not correspond to the increase in scattering which is in agreement with the findings from the PSD-analysis from the AFM. Instead, Y increases significantly with time, implying a drastic change in the roughness in the scale of λ. The main increment is found within the first 200 s of etching – a subsequent raise is observed between 400 s and 600 s, which corresponds with the occurrence of the smaller second bulge around 1 μm^{-1} in the PSD for a duration of 300 s (Fig. 5.16). The possible reasons for its appearance, like local-dependent etch rates from charge domains and local melting from heat-up, are stated above. Z is only of minor importance, and a comparatively high value for the untreated substrate may be caused by the relative high noise to signal ratio in this measurement.

The knowledge of TS$_b$, R and λ allows for a quantitative statement of rms-roughness in the wavelength scale utilizing eq. (4.4). It is important to choose probing wavelengths far from absorption bands to neglect other loss mechanisms. Table 5.5 lists the values for σ. Their accuracy depends particularly on reflectance and as R drops below measurement accuracy the uncertainty in σ increases rapidly. In the beginning, the uncertainty is approximately ± 0.7 nm. It is estimated by ± 5 nm for 600 s. The untreated substrate has a surface roughness of less than 4 nm, which doubles during the first 200 s of plasma treatment. A substantial increment is observed to the duration of 400 s. The mean roughness is close to 26 nm which is a rise of 320%. The further growth is more slowly having an additional increase of about 5%.

At this stage, a comparison to the rms-roughness values, tab. 5.2, from AFM analytics is possible. It was found 0.5 nm, 7.2 nm, 10.2 nm, and 18.0 nm for 0 s, 100 s, 150 s, and 300 s, respectively. These values are in good agreement with the results from scatter measurement, considering that the AFM data results from a large band of spatial frequencies and the optical methods utilizes only two spatial frequencies (wavelengths) for averaging. Nevertheless, both methods are faulty when the structures become to height. The AFM tip is not able to resolve details due to the limitation of its aspect ratio and the analysis of backscattering is limited by the accuracy of the reflection measurement ($R \rightarrow 0$).

Even if a detailed scattering analysis is denied due to the accuracy of measurement, the trend reveals that the cause of the main scatter losses in the observed time scale is not solely the antireflective SWS

Tab. 5.5: *Determination of rms-roughness from (4.4) at two probing wavelengths.*

Time / s	$\lambda = 400$ nm			$\lambda = 500$ nm			**average**
	$\boldsymbol{R}$	$\mathbf{TS}_b$	σ / **nm**	$\boldsymbol{R}$	$\mathbf{TS}_b$	σ / **nm**	$\tilde{\sigma}$ / **nm**
0	3.9%	0.04%	3.2	3.8%	0.03%	3.6	3.4
200	1.5%	0.10%	8.3	2.1%	0.08%	7.8	8.0
400	0.1%	0.11%	33.5	0.4%	0.07%	18.0	25.8
600	0.2%	0.16%	31.2	0.3%	0.10%	22.8	27.0

(and thus not its shape), but an overlaying far reaching surface corrugation (waviness). It emerges from the plasma etching process, since it is not detectable for an untreated substrate. A reason may be a surface charge-induced deceleration or deflection of the plasma's particle flux followed by a decreased etch performance. Material inhomogeneities that affect the density may have the same consequence.

As the pins are growing with time, their lateral dimensions (width and effective period) will violate the subwavelength criteria from sec. 2.1 sometime, and the scatter losses should increase tremendously. This stage was not investigated further, but it might be of special interest for the light coupling into or out of structured substrates.

5.6 Aspects of self-organization

Up to now, the structure formation has to be seen as a self-organizing process, since no external mechanisms force the pattern generation in this dimension. Moreover, it is a spontaneous process. The typical conditions for self-organization are apparent and can be related to certain substeps.

As the surface underlies permanent energy impact, substance exchange, and modifications (etching, redeposition) during plasma treatment, this system is far from thermodynamic equilibrium. The discussed internal processes (e.g., angle-dependent sputter erosion, chemical decomposition, surface diffusion, generation of a layer due to subsurface damage) are highly nonlinear processes within the available energy range of the participating plasma species. The processes are cooperative, meaning they represent protagonist and antagonist. Sputtering and decomposition can cause redeposition. As another example, the heat impact by ions and fast neutrals may lead to thermal diffusion and subsequent smoothing. The thickness of the modified region is forced by a balance of formation in the subsurface region and chemical etching at the top. Critical parameters must be exceeded to initiate the structure formation. In the discussed case, this may be a certain selectivity in etching or a minimum etch rate to achieve an adequate aspect ratio. A charging of domains caused by the dielectric strength as discussed in sec. 3.3.3 may be another mechanism that influences the emergence of structures. The surface diffusion and the chemical reactions depend strongly on temperature leading to limitations for the process. Finally, microscopic fluctuations have to be present to initiate the process which are given in the natural roughness of the substrate for the angle-dependent sputter process, the varying thickness of the subsurface damage region, or even the statistical process of ion impact and collision cascades.

The comparable structure formation was found on all of the discussed thermoplastic surfaces – and even on further tested polymers, too. Their analysis would go beyond the scope of this work, but underlines the fundamental character of the plasma-induced structure formation process. The difference in pin shape is specific to the plasma-treated polymer. The intrinsic material properties determine the etch rate that is crucial to achieve an applicable antireflection effect within an economically justifiable process time.

The structure formation was stopped in order to reveal a sufficient antireflection performance in the visible spectral range. Thus, the investigated surfaces exhibit pins, whose growth is not in steady state, but in a dynamic state. They would still grow, if exposed further to the plasma. A steady state, which may be described sufficiently by the Bradley-Harper theory, was only observed, when oxygen was absent. Shifting to a reactive process means to amplify the structure formation due to a dominant erosion.

6 Conclusions

The subject of this work was to extend the understanding in the growth and characterization of antireflective subwavelength structures on polymer surfaces. The formation has been addressed to a self-organizing process. Comparable morphologies have been established for PMMA, PC, PET, and PA. Thus, it is suggested that this process is fundamental for the spanning polymer class.

A comprehensive plasma analysis was utilized to find out the main processes of plasma-polymer-interaction and their relevance on the structuring. The effect of physical ablation was simulated by means of Monte Carlo method and have revealed an increase in sputter yield with ion energy and angle of incidence. The decomposition results from differing sputter yields of the polymers' constituents carbon, oxygen, nitrogen and hydrogen. It has been pointed out, that an enrichment of carbon can limit the process and defines the total (physical + chemical) etch rate. This is consistent with the measured value that is lowest for the polymers with highest relative carbon content and depends strongly on the oxygen fraction in the gas phase.

Nevertheless, describing a structure formation by self-organization according to Bradley and Harper [16] solely due to physical ablation disregards the chemical etching as a main decomposition process. Moreover, the underlying formation mechanisms are in the order of penetration depth of the impinging ions and thus too small for antireflective structures. The model may be strictly allowed only for small pin sizes, as they occur in the initial state. Contrary, this time is too short to heat-up the surface region above the softening temperature to introduce surface diffusion as the typical smoothing mechanism. Furthermore, the structure formation at oblique ion incidence is not consistent with the Bradley-Harper theory, which outlines a wavy corrugation normal to the surface plane, instead of a slanted pin structure.

A convenient method to detect thin modified surface layers on rough polymeric substrates directly, was not found yet in literature, but the results from Monte Carlo method and a detectable increase in absorption have suggested the formation in the subsurface region. Its thickness is self-regulating, because of the two competing processes synthesis in the subsurface region and etching at the surface. The existence of a thin modified layer can introduce a spatial selectivity in erosion that can explain the structure formation in terms of Oehrlein [17] even for tilted surfaces.

The influence of the high-energetic photons (UV range) is still indistinct in the structure formation process, because photons cannot be excluded from the plasma process, are able to break the chemical bondings, but cause only minor ablation. The kind of excited species has been determined from emission spectroscopy in the visible region and their potential radiation in the UV range has been deduced. However, the damage mechanisms, found in literature, do not have any clue for an ablative structure formation.

A deterministic description of the stochastic morphology is suitable only to a limited extent. A meaningful estimation of distinctive shape properties is accessible from statistical averaging. The imaging of scanning electron microscopy and atomic force microscopy has revealed typical feature dimensions, but only the statistical analysis have shown results that are in agreement with the spectral properties of the structured surface. The computation using rigorous diffraction theory has revealed typical structure heights of at least 300 nm and tapered pin shape as the basic conditions in order to get broadband antireflection effect in the visible spectral region.

Effective medium theory has been applied to model the rough surface as a layer with a refractive index gradient. Laterally homogeneous, such films have been computed by using transfer matrix methods that allow for real-time spectral reverse engineering, even of *in situ* recorded data. Therefore, sensible constrained parameters are very important. The obtained refractive index gradients are in agreement with the estimation from statistical AFM analysis. The Fermi function has been suggested as an analytical expression for a well-suiting profile and has been applied for *in situ* calculation.

An increase in optical loss in the visible spectral region has been found during plasma treatment. While a small increase in absorption is observed already in the beginning and indicates a carbon-rich zone at the surface, tremendous scatter losses occur after a certain process duration due to the ongoing pin growth that causes lateral distances in the size of the wavelength. An optimal process shut-off time follows, for which scatter losses are not relevant. A total transmittance of 99% for a double-side treated PMMA sheet in the VIS region has been demonstrated.

This thesis demonstrates for the first time the feasibility of antireflective surfaces on polymeric substrates different than PMMA by a plasma treatment. Especially the modified PET surfaces are currently discussed in terms of industrial application. The plasma parameters, except process duration, have shown only a minor impact on shape and size of the structure. The pin shape is rather influenced by the material itself. Thus, the flexibility of this technique is limited, regarding the achievable spectral properties like wavelength range and peak transmission, due to an attainable aspect ratio. This behavior is quite typical for self-organization processes.

Additional applications arise from overcoating. The deposition with metals lead to a subwavelength structured dielectric-metal interface with the contour of the needles [27], which acts as a broadband absorber, if irradiated from the dielectric polymer side. Moreover, the increase in roughness can be used to amplify the wetting behavior. This allows for super-hydrophobic surfaces, when overcoated with materials having a low surface energy like fluoralkylsilanes, or hydrophilicity when deposited with high surface energy substances like SiO_2. Finally, multifunctional surfaces are available that combine antireflective and easy-to-clean properties or antifog effects [187].

References

[1] Lommel, "Versuche über die Ursachen des Anlaufens und Mattwerdens des Glases und die Mittel denselben zuvorzukommen," in *J. von Fraunhofers gesammelte Schriften* pp. 3 – 50 (1888).

[2] A. Smakula, "Verfahren zur Erhöhung der Lichtdurchlässigkeit optischer Teile durch Erniedrigung des Brechungsexponenten an den Grenzflächen dieser optischen Teile," Patent DE **685767** (1935).

[3] H. A. Macleod, *Thin-film optical filters* (Institute of Physics Publishing, London, 2001).

[4] J. A. Dobrowolski, D. Poitras, P. Ma, H. Vakil, and M. Acree, "Toward perfect antireflection coatings: numerical investigation," Applied Optics **41**, 3075 – 3083 (2002).

[5] D. Poitras and J. A. Dobrowolski, "Toward perfect antireflection coatings. 2. Theory," Applied Optics **43**, 1286 – 1295 (2004).

[6] R. Leitel, O. Stenzel, S. Wilbrandt, D. Gäbler, V. Janicki, and N. Kaiser, "Optical and non-optical characterization of Nb_2O_5-SiO_2 compositional graded-index layers and rugate structures," Thin solid films **497**, 135 – 141 (2006).

[7] H. Bartzsch, S. Lange, P. Frach, and K. Goedicke, "Graded refractive index layer systems for antireflective coatings and rugate filters deposited by reactive pulse magnetron sputtering," Surface and Coatings Technology **180 − 181**, 616 – 620 (2004).

[8] D. Chen, "Anti-reflection (AR) coatings made by sol-gel processes: A review," Solar Energy Materials & Solar Cells **68**, 313 – 336 (2001).

[9] C. G. Bernhard, "Structural and functional adaption in a visual system," Endeavour **26**, 79 – 84 (1967).

[10] W. H. Lowdermilk and D. Milam, "Graded-index antireflection surfaces for high-power laser applications," Applied Physics Letters **36**, 891 – 893 (1980).

[11] R. N. Wenzel, "Resistance of solid surfaces to wetting by water," Industrial and Engineering Chemistry **28**, 988 – 994 (1936).

[12] A. B. D. Cassie and S. Baxter, "Wettability of porous surfaces," Transactions of the Faraday Society **40**, 546 – 551 (1944).

[13] P. B. Clapham and M. C. Hutley, "Reduction of lens reflexion by the "moth eye" principle," Nature **244**, 281 – 282 (1973).

[14] A. Gombert, B. Bläsi, C. Bühler, P. Nitz, J. Mick, W. Hoßfeld, and M. Niggemann, "Some application cases and related manufacturing techniques for optically functional microstructures on large areas," Optical Engineering **43**, 2525 – 2533 (2004).

[15] P. Munzert, H. Uhlig, M. Scheler, U. Schulz, and N. Kaiser, "Verfahren zur Reduzierung der Grenzflächenreflexion von Kunststoffsubstraten," Patent DE **10241708** (2004).

[16] R. M. Bradley and J. M. E. Harper, "Theory of ripple topography induced by ion bombardment," J. Vac. Sci. Technol. A **6**, 2390 – 2395 (1988).

[17] G. S. Oehrlein, J. F. Rembetski, and E. H. Payne, "Study of sidewall passivation and microscopic silicon roughness phenomena in chlorine-based reactive ion etching of silicon trenches," J. Vac. Sci. Technol. B **8**, 1199 – 1211 (1990).

[18] A. Kaless, *Oberflächenmodifizierung von Polymethylmethacrylat durch Plasmabehandlung*, Ph.D. thesis, Martin-Luther Universität Halle-Wittenberg (2006).

[19] N. Vourdas, A. Tserepi, and E. Gogolides, "Nanotextured super-hydrophobic transparent poly(methyl methacrylate) surfaces using high-density plasma processing," Nanotechnology **18**, 1 – 7 (2007).

[20] P. Esena, C. Riccardi, S. Zanini, M. Tontini, G. Poletti, and F. Orsini, "Surface modification of PET film by a DBD device at atmospheric pressure," Surf. Coat. Technol. **200**, 664 – 667 (2005).

[21] H. Yasuda, C. E. Lamaze, and K. Sakaoku, "Effect of electrodeless glow discharge on polymers," J. Appl. Pol. Sci. **17**, 137 – 152 (1973).

[22] J. C. Stover, *Optical Scattering - Measurement and Analysis* (SPIE, Bellingham,USA, 1995).

[23] R. Leitel, A. Kaless, U. Schulz, and N. Kaiser, "Broadband antireflective structures on PMMA by plasma treatment," Plasma Process. Polym. **4**, S878 – S881 (2008).

[24] M. G. Moharam and T. K. Gaylord, "Rigorous coupled-wave analysis of planar-grating diffraction," Journal of Optical Society of America A **71**, 811 – 818 (1981).

[25] E. B. Grann and M. G. Moharam, "Comparison between continuous and discrete subwavelength grating structures for antireflection surfaces," Journal Optical Society of America A **13**, 988 – 992 (1996).

[26] P. Lalanne and M. Hutley, *Encyclopedia of Optical Engineering* (Marcel Dekker,Inc., 2003), chap. Artificial media optical properties - subwavelength scale, pp. 1 – 16.

[27] R. Leitel, J. Petschulat, A. Kaless, U. Schulz, O. Stenzel, and N. Kaiser, "Optical properties of stochastic subwavelength surface structures," in *Optical Fabrication, Testing and Metrology II* (SPIE, 2005), pp. 59 651O1 – 10.

[28] F. Abelès, "Recherches sur la propagation des ondes electomagnetique sinusoidales dans les milieux stratifiés. Applixation aux couches minces," Ann de Physique **5**, 596 – 640 (1950).

[29] R. T. Phillips, "A numerical method for determining the complex refractive index from reflectance and transmittance of supported thin films," J. Phys. D.: Appl. Phys. **16**, 489 – 497 (1983).

[30] J. P. Borgogno, B. Lazarides, and E. Pelletier, "Automatic determination of the optical constants of inhomogeneous thin films," Applied Optics **21**, 4020 – 4029 (1982).

[31] V. G. Bordo and H.-G. Rubahn, *Optics and Spectroscopy at Surfaces and Interfaces* (Wiley-VCH, Weinheim, 2005).

[32] C. Joachim, "To be nano or not to be nano?" Nature Mat. **4**, 107 – 109 (2005).

[33] D. G. Stearns, "Stochastic model for thin film growth and erosion," Appl. Phys. Lett. **62**, 1745 – 1747 (1992).

[34] P. Sigmund, “A mechanism of surface micro-roughening by ion bombardment,” J. Mater. Sci. **8**, 1545 – 1553 (1973).

[35] M. Kadar, G. Parisi, and Y.-C. Zhang, “Dynamic scaling of growing interfaces,” Phys. Rev. Lett. **56**, 889 – 892 (1986).

[36] R. Cuerno and A.-L. Barabási, “Dynamic scaling of ion-sputtered surfaces,” Phys. Rev. Lett. **74**, 4746 – 4749 (1995).

[37] D. H. Raguin and G. M. Morris, “Antireflection structured surfaces for the infrared spectral region,” Applied Optics **32**, 1154 – 1167 (1993).

[38] P. Lalanne and D. Lalanne, “Depth dependence of the effective properties of subwavelength gratings,” Journal of Optical Society of America A **14**, 450 – 458 (1997).

[39] S. M. Rytov, “The electromagnetic properties of finely layered medium,” Sov. Phys. JETP **2**, 466 – 475 (1956).

[40] E. B. Grann, M. G. Moharam, and D. A. Pommet, “Artificial uniaxial and biaxial dielectrics with use of two-dimensional subwavelength binary gratings,” Journal Optical Society of America A **11**, 2695 – 2703 (1994).

[41] W. Theiß, “The use of effective medium theories in optical spectroscopy,” Adv. Solid State Physics **33**, 149 (1993).

[42] L. Rayleigh, “On the influence of obstacles arranged in rectangular order upon the properties of a medium,” Philos. Mag. **34**, 481 – 502 (1892).

[43] J. C. M. Garnett, “Colours in metal glasses and in metallic films,” Philos. Trans. R. Soc. London A **203**, 385 – 420 (1904).

[44] D. A. G. Bruggeman, “Berechnung verschiedener physikalischer Konstanten von heterogenen Substanzen,” Annalen der Physik **24**, 636 – 664 (1935).

[45] T. Hanai, “Dielectric theory on the interfacial polarization for two-phase mixtures,” Bull. Inst. Chem. Res. Kyoto University **39**, 341 – 367 (1962).

[46] L. D. Landau and E. M. Lifschitz, *Lehrbuch der theoretischen Physik,Band 8: Elektrodynamik der Kontinua* (Akademie Verlag, Berlin, 1967).

[47] W. M. Merrill, R. E. Diaz, and N. G. Alexópoulos, “Extending the asymmetric Bruggeman effective medium theory to include scattering from small spherical inclusions,” IEEE Antennas and Propagation Society International Symposium **1**, 92 – 95 (1998).

[48] B. R. Johnson, “Exact theory of electromagnetic scattering by a heterogeneous multilayer sphere in the infinite-layer limit: effective-media approach,” Journal Optical Society of America A **16**, 845 – 852 (1999).

[49] O. Stenzel, *The physics of thin film optical spectra* (Springer-Verlag, Berlin, 2005).

[50] H.-J. Kuehn, *Möglichkeiten zur Bestimmung von Brechzahlprofil und Dispersion verlustfreier dünner Schichten auf der Basis von Reflexionsmessungen*, Ph.D. thesis, Friedrich-Schiller-University Jena (1989).

[51] H. Schröder, "Bemerkung zur Theorie des Lichtdurchgangs durch inhomogene durchsichtige Schichten," Annalen der Physik **39**, 55 – 58 (1941).

[52] A. V. Tikhonravov, M. K. Trubetskov, B. T. Sullivan, and J. A. Dobrowolski, "Influence of small inhomogeneities on the spectral characteristics of single thin films," Applied Optics **36**, 7188 – 7198 (1994).

[53] S. Furman and A. V. Tikhonravov, *Basics of Multilayer Films* (Editions Frontières, Gif-sur Yvette, 1992).

[54] R. R. Willey, *Practical Design and Production of Optical Thin Films* (Marcel Dekker,Inc., New York, 2002).

[55] Optilayer Ltd., http://www.optilayer.com/, *Optilayer Thin Film Software, Version 6.11* (1996 – 2007).

[56] Scientific Computing International, http://www.sci-soft.com/, *Film Wizard,Version 8.20* (1993 – 2007).

[57] Thin Film Center Inc., http://www.thinfilmcenter.com/, *Essential Macleod, Version 8.16* (1993 – 2007).

[58] K. Kurihara, "Development of large-scale production technology of anti-reflective lens using nanoparticles," AIST Today **7**, 13 – 15 (2007).

[59] Y. Zhao, J. Wang, and G. Mao, "Colloidal subwavelength nanostructures for antireflection optical coatings," Opt. Lett. **30**, 1885 – 1887 (2005).

[60] A. Musset and A. Thelen, *Multilayer antireflection coatings* (North-Holland, Amsterdam, 1970).

[61] U. Schulz, U. B. Schallenberg, and N. Kaiser, "Antireflection coating design for plastic optics," Applied Optics **41**, 3107 – 3110 (2002).

[62] S. Wilbrandt, O. Stenzel, and N. Kaiser, "Experimental determination of the refractive index profile of rugate filters based on in situ measurements of transmission spectra," J. Phys. D: Appl. Phys. **40**, 1435 – 1441 (2007).

[63] R. Leitel, U. Schulz, N. Kaiser, and A. Tünnermann, "Stochastic subwavelength structures on poly(methyl methacrylate) surfaces for antireflection generated by plasma treatment," Appl. Opt. **47**, C143 – C146 (2008).

[64] G. Ehret, E. Buhr, A. Höpe, M. Gebhardt, and H.-M. Bitzer, "Rigorose Modellierung der Wechselwirkung optischer Strahlung mit stochastisch nanostrukturierten PMMA-Oberflächen," in *108. Jahrestagung der DGaO, Bad Heringsdorf* (Deutsche Gesellschaft für angewandte Optik, 2007), pp. 4 – 5.

[65] Optimod, http://www.unigit.com/, *Unigit, Version 1.00.14* (1999 – 2006).

[66] P. M. Bellan, *Fundamentals of Plasma Physics* (Cambridge University Press, Cambridge, 2006).

[67] R. Rank, T. Wünsche, and S. Günther, "Magnetically enhanced RF discharges for effective pre-treatment of plastic webs at high speed," Surf. Coat. Technol. $\mathbf{174-175}$, 218 – 221 (2003).

[68] A. Anders, "Plasma and ion sources in large area coating: A review," Surf. Coat. Technol. **200**, 1893 – 1906 (2005).

[69] B. Chapman, *Glow Discharge Processes* (John Wiley & Sons, New York, 1980).

[70] Röhm-Degussa,Evonik Industries, http://www.roehm.de/degussa/de/, *Produktdatenblatt PLEXIGLAS Formmasse 7N* (2006).

[71] Bayer MaterialScience AG, http://plastics.bayer.com/plastics/emea/en/product/makrolon/-Product_description.html, *Makrolon - Product Range & Typical Values* (2005).

[72] DuPont Teijin Films, http://www.dupontteijinfilms.com/FilmEnterprise/FilmType-Selector.asp?Version=US, *Film Type Selector* (2006).

[73] High Performance Polymers Degussa AG, Evonik Industries, http://www.degussa-hpp.de/ger/produkte/hpp/trogamid_cx.shtml, *TROGAMID CX - Polyamid PA PACM 12* (2003).

[74] D. J. McClure, "Polyester (PET) film as a substrate: a tutorial," in *50th SVC TechCon,Louisville,KY,USA* (Society of Vacuum Coaters, 2007), pp. 51 – 57.

[75] S. A. Baeurle, A. Hotta, and A. A. Gusev, "On the glassy state of multiphase and pure polymer materials," Polymer **47**, 6243 – 6253 (2006).

[76] K. Mazur, "More data about dielectric and electret properties of poly(methyl methacrylate)," J. Phys. D: Appl. Phys. **30**, 1383 – 1398 (1997).

[77] T. Ficker, "Electrostatic microdischarges on the surface of electrets," J. Phys. D: Appl. phys. **38**, 483 – 489 (2005).

[78] G. M. Yang, G. M. Sessler, H. Müller, and W. Roth, "Electret behavior of PET films in various stages of production," in *9th International Symposium on Electrets* (IEEE, 1996), pp. 201 – 206.

[79] G. Yianakopoulos, J. Vanderschueren, J. Niezette, and A. Thielen, "Influence of physical aging processes on electrical properties of amorphous polymers," in *Transactions on Electrical Insulation* (IEEE, 1990), pp. 693 – 701.

[80] J. L. Gil-Zambrano and C. Juhasz, "Space charge polarisation in nylon films," J. Phys. D.: Appl. Phys. **15**, 119 – 128 (1982).

[81] H. Gong, Z. G. Song, and C. K. Ong, "Space-charge dynamics of polymethylmethacrylate under electron beam irradiation," J. Phys.: Condens. Matter **9**, 5027 – 5031 (1997).

[82] V. I. Arkhipov, A. I. Rudenko, and G. M. Sessler, "Radiation-induced conductivity and charge storage in irradiated dielectrics," J. Phys. D: Appl. Phys. **26**, 1298 – 1300 (1993).

[83] O. N. Oliveira and G. F. L. Ferreira, "Electron transport in corona charged 12 μm Teflon FEP with saturable deep traps," Appl. Phys. A **42**, 213 – 217 (1987).

[84] G. for Infrared Spectroscopy, *Near infrared table*, Bruker Optik GmbH,Germany (2000).

[85] P. K. Chu, J. Y. Chen, L. P. Wang, and N. Huang, "Plasma-surface modification of biomaterials," Materials Science and Engineering **R 36**, 143 – 206 (2002).

[86] J. Ulbricht, *Grundlagen der Synthese von Polymeren* (Akademie Verlag, Berlin, 1978).

[87] R. Hippler, S. Pfau, M. Schmidt, and K. H. Schoenbach, *Low Temperature Plasma Physics* (Wiley-VCH, Berlin, 2001).

[88] N. C. Us, R. W. Sadowski, and J. W. Coburn, "Quartz crystal microbalance simulation of the directionality of Si etching in CF4 glow discharges," Plasma Chem. Plasma Process. **6**, 1 – 10 (1985).

[89] E. Occhiello, F. Garbassi, and J. W. Coburn, "On the effect of low-energy ion bombardment on polystyrene and polymethylmethacrylate etch rates in rf plasmas," Plasma Chem. Plasma Process. **9**, 3 – 12 (1989).

[90] R. d'Agostino, *Plasma Deposition, Treatment, and Etching of Polymers* (Academic Press, Inc., San Diego, 1990).

[91] U. Schulz, P. Munzert, and N. Kaiser, "Surface modification of PMMA by DC glow discharge and microwave plasma treatment for the improvement of coating adhesion," Surface and Coatings Technology **142 − 144**, 507 – 511 (2001).

[92] T. G. Vargo, J. A. Gardella, and L. Salvati, "Multitechnique surface spectroscopic studies of plasma modified polymers III. H_2O and O_2/H_2O plasma modified poly(methyl methacrylate)s," Journal of Polymer Science A **27**, 1267 – 1286 (1989).

[93] T. J. Hook, J. A. Gardella, and L. Salvati, "Multitechnique surface spectroscopic studies of plasma modified polymers I. H_2O/Ar plasma-modified polymethylmethacrylates," Journal of Material Research **2**, 117 – 131 (1987).

[94] M. Collaud, P. Groening, S. Nowak, and L. Schlapbach, "Plasma treatment of polymers: effect of the plasma parameters on the chemical,physical and morphological state of the polymer surface and on the metal-polymer interface," Journal of Adhesion Science Technology **8**, 1115 – 1127 (1994).

[95] P. Groening, M. Collaud-Coen, G. Dietler, and L. Schlapbach, "Plasma modification of polymethylmethacrylate and polyethyleneterephthalate surfaces," Journal of Applied Physics **76**, 887 – 892 (1994).

[96] P. Groening, O. M. Küttel, M. Collaud-Coen, G. Dietler, and L. Schlapbach, "Interactions of low-energy ions (<10 eV) with polymethylmethacrylate," Applied Surface Science **89**, 83 – 91 (1995).

[97] R. Kallweit and J. P. Biersack, "Ion beam induced changes of the refractive index of PMMA," Radiation Effects and Defects in Solids **116**, 29 – 36 (1991).

[98] A. Kaless, U. Schulz, and N. Kaiser, "Self-organized antireflective nanostructures on PMMA by ion etching," in *Optical Fabrication, Testing and Metrology II* (SPIE, 2005), pp. 59 651N1 – 9.

[99] A. Valsesia, M. M. Silvan, G. Ceccone, and F. Rossi, "Surface topographic and structural characterization of plasma treated PMAA-PMMA copolymer films," Surface Science **560**, 121 – 129 (2004).

[100] Y. Koval, "Mechanism of etching and surface relief development of PMMA under low-energy ion bombardment," J. Vac. Sci. Technol. B **22**, 843 – 851 (2004).

[101] Y. Koval, M. V. Fistul, and P. Müller, "Conductance enhancement of polymethylmethacrylate bombarded by low-energy ions," J. Vac. Sci. Technol. A **23**, 1375 – 1378 (2005).

[102] B. Wasserman, "Fractal nature of electrical conductivity in ion-implanted polymers," Phys. Rev. B **34**, 1926 – 1931 (1986).

[103] J.-P. Salvetat, J.-M. Costantini, F. Brisard, and L. Zuppiroli, "Onset and growth of conduction in polyimide Kapton induced by swift heavy-ion irradiation," Phys. Rev. B **55**, 6238 – 6248 (1997).

[104] E. Occhiello, M. Morra, F. Gardassi, and J. Bargon, "On the application of XPS, SSIMS and QCM to study the surface of a CF_4/O_2 plasma treated polycarbonate," Applied Surface Science **36**, 285 – 295 (1989).

[105] N. Inagaki, K. Narushima, and S. K. Lim, "Effects of aromatic groups in polymer chains on plasma surface modification," J. Appl. Surf. Sci. **89**, 96 – 103 (2003).

[106] N. Inagaki, S. Tasaka, H. Kawai, and Y. Yamada, "Surface modification of aromatic polyamide film by remote oxygen plasma," J. Appl. Poly. Sci. **64**, 831 – 840 (1998).

[107] N. Inagaki, S. Tasaka, and H. Kawai, "Surface modification of aromatic polyamide film by oxygen plasma," J. Polym Sci.,Polym Chem. **33**, 2001 – 2011 (2001).

[108] F. Garbassi, M. Morra, and E. Occhiello, *Polymer Surfaces - From Physics to Technology* (John Wiley & Sons Ltd., West Sussex,England, 1998).

[109] F. S. Denes and S. Manolache, "Macromolecular plasma-chemistry: an emerging field of polymer science," Prog. Polym. Sci. **29**, 815 – 885 (2004).

[110] S. Wu, *Polymer Interface and Adhesion* (Marcel Dekker, Inc., New York, 1982).

[111] H. Gokan, Y. Ohnishi, and K. Saigo, "Oxygen ion-beam etch resistance of metal-free and organosilicon resist materials," Microelectr. Eng. **1**, 251 – 262 (1983).

[112] R. H. Hansen, J. V. Pascale, T. de Benedictis, and P. M. Rentzepis, "Effect of atomic oxygen on polymers," J. Polym. Sci. A **3**, 2205 – 2214 (1965).

[113] R. M. Mantell and W. L. Ormand, "Activation of plastic surfaces in a plasmajet," Ind. Eng. Chem.,Prod. Res. Dev. **3**, 300 – 303 (1964).

[114] T. Venkatesan, S. R. Forrest, M. L. Kaplan, C. A. Murray, P. H. Schmidt, and B. J. Wilkens, "Ion-beam-induced conductivity in polymer films," J. Appl. Phys. **54**, 3150 – 3153 (1983).

[115] S. Brock, S. P. Hersh, P. L. Grady, and J. J. Wortman, "Enhanced electrical conductivity of poly(ethylene terephthalate) implanted with fluorine ions," J. Polym Sci: Polym Phys. Ed. **22**, 1349 – 1452 (1984).

[116] J. R. Kulish, H. Franke, A. Singh, R. A. Lessard, and E. J. Knystautas, "Ion implantation, a method for fabricating light guides in polymers," J. Appl. Phys **63**, 2517 – 2521 (1988).

[117] R. Kallweit, U. Roll, P. Eichinger, H. Strack, and A. Pöcker, "Correlation between chemical modification and generated refractive index on ion implanted PMMA," in *Materials Modification by Energetic Atoms and Ions* (Material Research Society, 1992), pp. 363 – 368.

[118] A. Holländer, J. E. Klemberg-Sapieha, and M. R. Wertheimer, "Vacuum-ultraviolet induced oxidation of the polymers polyethylene and polypropylene," J. Polym. Sci. A **33**, 2013 – 2025 (1995).

[119] J. Hudis, "Surface cross-linking of polyethylene using a hydrogen glow discharge," J. Appl. Polym. Sci. **16**, 2397 – 2415 (1972).

[120] M. R. Wertheimer, A. C. Fozza, and A. Holländer, "Industrial processing of polymers by low-pressure plasmas: the role of VUV radiation," Nucl. Instr. Meth. Phys. Res. B **151**, 65 – 75 (1999).

[121] J. F. Rabek, *Polymer Photodegradation: Mechanisms and experimental methods* (Chapman & Hall, London, 1995).

[122] A. C. Fozza, J. Roch, J. E. Klemberg-Sapieha, A. Kruse, A. Holländer, and M. R. Wertheimer, "Oxidation and ablation of polymers by vacuum-UV radiation from low pressure plasmas," Nucl. Instr. Meth. Phys. Res. B **131**, 205 – 210 (1997).

[123] A. C. Fozza, J. E. Klemberg-Sapieha, and M. R. Wertheimer, "Vacuum ultraviolet irradiation of polymers," Plasma and Polymers **4**, 183 – 206 (1999).

[124] S. Kueper, S. Modaressi, , and M. Stuke, "Photofragmentation pathways of a PMMA model compound under UV excimer laser ablation conditions," Journal of Physical Chemistry **94**, 7514 – 7518 (1990).

[125] C. Wochnowski, S. Metev, and G. Sepold, "UV–laser-assisted modification of the optical properties of polymethylmethacrylate," Applied Surface Science $\mathbf{154-155}$, 706 – 711 (2000).

[126] N. Bityurin, S. Muraviov, A. Alexandrov, and A. Malyshev, "UV laser modifications and etching of polymer films (PMMA) below the ablation threshold," Applied Surface Science $\mathbf{109-110}$, 270 – 274 (1997).

[127] P. Munzert, *Entwicklung von Vakuumbeschichtungsprozessen für die Entspiegelung von Polymethylmethacrylat*, Ph.D. thesis, Martin-Luther Universität Halle-Wittenberg (2004).

[128] M. Nowicki, H. Kaczmarek, R. Czajka, and B. Susla, "Atomic force microscopy investigation of nanometer-scale modifications of polymer morphology caused by ultraviolet radiation," J. Vac. Sci. Technol. A **18**, 2477 – 2481 (2000).

[129] Y. Ichihashi, P. Henzi, M. Bruendel, D. G. Rabus, and J. Mohrt, "Material investigation of alicyclic methacrylate copolymer for polymer waveguide fabrication," Jap. J. Appl. Phys. **45**, 2572 – 2575 (2006).

[130] A. Rivaton, D. Sallet, and J. Lemaire, "The Photochemistry of Bisphenol-A Polycarbonate Reconsidered," Polymer Photochemistry **3**, 463 – 481 (1983).

[131] M. C. Burrell and M. G. Tilley, "Surface chemistry of polycarbonate film and adhesion of ultraviolet-cured inks," J. Vac. Soc. Am. A **12**, 2507 – 2514 (1994).

[132] A. Ram, O. Zilber, and S. Kenig, "Life expectation of polycarbonate," Polym. Eng. Sci. **25**, 535 – 540 (1985).

[133] M. Day and D. M. Wiles, "Photochemical degradation of poly(ethylene terephthalate). II. Effect of wavelength and environment on the decomposition process," J. Appl. Polym. Sci. **16**, 191 – 202 (1972).

[134] G. J. M. Fechine, M. S. Rabello, R. M. S. Maior, and L. H. Catalani, "Surface characterization of photodegraded poly(ethylene terephthalate). The effect of ultraviolet absorbers," Polymer **45**, 2303 – 2308 (2004).

[135] A. Franck, *Kunststoff-Kompendium, 4. Auflage* (Vogel, Würzburg, 1996).

[136] R. Srinivasan and S. Lazare, "Modification of polymer surfaces by far-ultraviolet radiation of low and high (laser) intensities," Polymers **26**, 1297 – 1300 (2003).

[137] J. T. C. Yeh, "Laser ablation of polymers," J. Vac. Sci. Technol. A **4**, 653 – 658 (1986).

[138] M. Csete, R. Eberle, M. Pietralla, O. Marti, and Z. Bor, "Attenuated total reflection measurements on poly-carbonate surfaces structured by laser illumination," Applied Surface Science $\mathbf{208-209}$, 474 – 480 (2003).

[139] J. E. Sipe, F. Young, J. S. Preston, and H. M. Driel, "Laser-induced periodic surface structures. I. Theory," Phys. Rev. B **27**, 1141 – 1154 (1983).

[140] H. M. Driel, J. E. Sipe, and J. F. Young, “Laser-induced periodic surface structures on solids: a universal phenomenon,” Phys. Rev. Lett. **49**, 1955 – 1958 (1982).

[141] M. Csete and Z. Bor, “Laser-induced periodic surface structure formation on polyethylene-terephthalate,” Applied Surface Science **133**, 5 – 16 (1998).

[142] W. Wong, K. Chan, K. W. Yeung, and K. S. Lau, “Surface structuring of poly(ethylene terephthalate) by UV excimer laser,” J. Mater. Proc. Technol. **132**, 144 – 118 (2003).

[143] C. M. Chan, T.-M.Ko, and H. Hiraoka, “Polymer surface modification by plasmas and photons,” Surf. Sci. Rep. **24**, 1 – 54 (1996).

[144] G. Carter, M. J. Nobes, and R. P. Webb, “A second-order erosion slowness theory of the development of surface topography by ion-induced sputtering,” J. Mater. Sci **16**, 2091 – 2102 (1981).

[145] W. W. Mullins, “Theory of thermal grooving,” J. Appl. Phys. **28**, 333 – 339 (1957).

[146] E. Chason and M. J. Aziz, “Spontaneous formation of patterns on sputtered surfaces,” Scripta Materialia **49**, 953 – 959 (2003).

[147] F. Frost, B. Ziberi, T. Höche, and B. Rauschenbach, “The shape and ordering of self-organized nanostructures by ion sputtering,” Nucl. Instr. Meth. Phys. Res. B **216**, 9 – 19 (2004).

[148] S. Habenicht, “Morphology of graphite surfaces after ion-beam erosion,” Phys. Rev. B **63**, 125 419 – 125 426 (2001).

[149] T. M. Mayer, E. Chason, and A. J. Howard, “Roughening instability and ion-induced viscous relaxation of SiO2 surfaces,” J. Appl. Phys. **76**, 1633 – 1643 (1994).

[150] U. Valbusa, C. Boragno, and F. B. de Mongeot, “Nanostructuring surfaces by ion sputtering,” J. Phy.: Condens. Matter **14**, 8153 – 8175 (2002).

[151] M. A. Makeev, R. Cuerno, and A.-L. Barabási, “Morphology of ion-sputtered surfaces,” Nucl. Instr. Meth. Phys. Res. B **197**, 185 – 227 (2002).

[152] M. Köhler, *Etching in Microsystem Technology* (Wiley VCH, Weinheim, 1999).

[153] J. W. Coburn and H. F. Winters, “Plasma etching: a discussion of mechanisms,” J. Vac. Sci. Technol. **16**, 391 – 403 (1979).

[154] J. C. Arnold and H. H. Sawin, “Charging of pattern features during plasma etching,” J. Appl. Phys. **70**, 5314 – 5317 (1991).

[155] S. G. Ingram, “The influence of substrate topography on ion bombardment in plasma etching,” J. Appl. Phys. **68**, 500 – 504 (1990).

[156] M. Schulze, H.-J. Fuchs, E.-B. Kley, and A. Tünnermann, “New approach for antireflective fused silica surfaces by statistical nanostructures,” in *Advanced Fabrication Technologies for Micro/Nano Optics and Photonics* (SPIE, 2008), p. 68830N.

[157] S. Pongratz and A. Zöller, “Plasma ion-assisted deposition: a promising technique for optical coatings,” J. Vac. Sci. Technol. A **10**, 1897 – 1904 (1992).

[158] W. Lochte-Holtgreven, *Plasma Diagnostics* (North-Holland Publishing Company, Amsterdam, 1969).

[159] A. Zöller, S. Beisswenger, R. Götzelmann, and K. Matl, "Plasma ion assisted deposition: a novel technique for the production of optical coatings," Proc. SPIE **2253**, 394 – 402 (1994).

[160] H. Bubert and H. Jenett, *Surface and Thin Film Analysis* (Wiley-VCH Verlags GmbH, Weinheim, 2002).

[161] A. Richard, T. Czerwiec, T. Belmonte, S. Bockel, and H. Michel, "Detection by emission spectroscopy of active species in plasma-surface processes," Thin Solid Films **341**, 1 – 8 (1999).

[162] W. Demtröder, *Molecular Physics: Theoretical Principles and Experimental Methods* (Wiley-VCH, Weinheim, 2005).

[163] Y. Ralchenko, F.-C. Jou, D. E. Kelleher, A. E. Kramida, A. Musgrove, J. Reader, W. L. Wiese, and K. Olsen, *NIST Atomic Spectra Database* (National Institute of Standards and Technology, Gaithersburg, MD, 2007).

[164] ECD, http://www.ecd.com/tutorials/HTML/index.html, *SuperM.O.L.E. Gold*, 3.00 edn. (1991 – 1999).

[165] J. F. Ziegler, J. P. Biersack, and U. Littmark, *The Stopping and Range of Ions in Solids* (Pergamon Press, New York, 1985).

[166] J. F. Ziegler, *SRIM - The Stopping and Range of Ions in Matter*, http://www.srim.org/ (2000).

[167] J. F. Ziegler and J. M. Manoyan, "The stopping of ions in compounds," Nuclear Instruments and Methods B **35**, 215 – 228 (1989).

[168] M. Born and E. Wolf, *Principles of Optics, 7th ed.* (Cambridge University Press, Cambridge, 1999).

[169] P. J. Goodhew, J. Humphreys, and R. Beanland, *Electron Microscopy and Analysis, 3rd ed.* (Taylor & Frances, London, 2001).

[170] Philips, FEI Company, *Operating Instructions, XL 40 ESEM TMP, Scanning Electron Microscope*, 2.1 edn. (2001).

[171] G. Binnig, C. F. Quate, and C. Gerber, "Atomic force microscopy," Physical Review Letters **56**, 930 – 933 (1986).

[172] S. N. Magonov and M. H. Whangbo, *Surface Analysis with STM and AFM* (VCH-Verlagsgesellschaft, Weinheim, 1996).

[173] J. Griffith, *Probe-Simulator*, Lehigh Microscopy School, http://www.nanoscience.com/education/software.html (2003).

[174] D. Instruments, *Dimension 3100*, Digital Instruments, Veeco Metrology Group, 3.0 edn. (2000).

[175] A. Gombert, W. Glaubitt, K. Rose, J. Dreibholz, B. Bläsi, A. Heinzel, D. Sporn, W. Döll, and V. Wittwer, "Subwavelength-structured antireflective surfaces on glass," Thin Solid Films **351**, 73 – 78 (1999).

[176] B. Bläsi, *Holographisch hergestellte Antireflexoberflächen für solare und visuelle Anwendungen*, Ph.D. thesis, Albert-Ludwigs-Universität Freiburg i. Br. (2000).

[177] Perkin Elmer, Inc., http://www.perkinelmer.com/, *User's Guide Lambda 900* (2001).

[178] S. Wilbrandt, N. Kaiser, and O. Stenzel, "In-situ broadband monitoring of heterogeneous optical coatings," Thin Solid Films **502**, 153 – 157 (2006).

[179] J. Beaulieu, *A Guide to Integrating Sphere Radiometry and Photometry*, Labsphere, Inc., http://www.labsphere.com/ (2000).

[180] T. Q. Khanh and W. Dähn, "Die Ulbrichtsche Kugel: Theorie und Anwendungsbeispiele in der optischen Strahlungsmesstechnik," Photonik **4**, 6 – 9 (1998).

[181] H. E. Bennett and J. Porteus, "Relation between surface roughness and specular reflectance at normal incidence," J. Opt. Soc. Am. A **51**, 123 – 129 (1961).

[182] A. Duparré, J. Ferre-Borrull, S. Gliech, G. Notni, J. Steinert, and J. M. Bennett, "Surface characterization techniques for determining the root-mean-square roughness and power spectral densities of optical components," Applied Optics **41**, 154 – 171 (2002).

[183] A. Mahdjoub and L. Zighed, "New designs for graded refractive index antireflection coatings," Thin Solid Films **478**, 299 – 304 (2005).

[184] D. Poitras, "Admittance diagrams of accidental and premediated optical inhomogeneities in coatings," Applied Optics **41**, 4671 – 4679 (2002).

[185] W. H. Southwall, "Gradient-index antireflection coatings," Optics Letters **8**, 584 – 586 (1983).

[186] E. B. Grann, M. G. Moharam, and D. A. Pommet, "Optimal design for antireflective tapered two-dimensional subwavelength grating structures," Journal Optical Society of America A **112**, 333 – 339 (1995).

[187] U. Schulz, P. Munzert, R. Leitel, I. Wendling, N. Kaiser, and A. Tünnermann, "Antireflection of transparent polymers by advanced plasma etching procedures," Optics Express **15**, 13 108 – 13 113 (2007).

Acknowledgments

I thank Prof. Andreas Tünnermann for supervision and Prof. Norbert Kaiser for setting-up the experimental conditions to work on the topic at the ”Optical Coatings” department of the Fraunhofer-Institute for Applied Optics and Precision Engineering.

Because of the high degree of complexity, the progress can be made only by a team that is dedicated to this matter: Many thanks to Dr. Ulrike Schulz, Dr. Peter Munzert, Dr. Antje Kaless, Irmina Wendling and Nancy Bollwahn, that all contribute to this work. Gratitude to Jörg Petschulat and Sven Schröder for very fruitful discussions and collaborations on optical modeling and surface characterization. An outstanding thank to Dr. Olaf Stenzel for professional assistance beyond all project limits.

Special thanks to the ”crew” of the office B2.26, namely Kevin Füchsel, Heidi Malaka and Dr. Petra Heger as well as the helping hands from Heidi Haase, Michael Scheler, Wieland Stöckl and Gisela Kühne.

Finally, I thank my family for encouraging me to scientific studies and supporting my doings.

Ehrenwörtliche Erklärung

Ich erkläre hiermit ehrenwörtlich, dass ich die vorliegende Arbeit selbstständig, ohne unzulässige Hilfe Dritter und ohne Benutzung anderer als der angegebenen Hilfsmittel und Literatur angefertigt habe. Die aus anderen Quellen direkt oder indirekt übernommenen Daten und Konzepte sind unter Angabe der Quelle gekennzeichnet.

Bei der Durchführung von Messungen haben mir die nachstehend aufgeführten Personen in der jeweils beschriebenen Weise entgeltlich/unentgeltlich geholfen:

- Plasma-Emissionsspektroskopie: Maik Sode
- AFM-Messungen und PSD-Analytik: Sven Schröder.

Weitere Personen waren an der inhaltlich-materiellen Erstellung der vorliegenden Arbeit nicht beteiligt. Insbesondere habe ich hierfür nicht die entgeltliche Hilfe von Vermittlungs- bzw. Beratungsdiensten (Promotionsberater oder andere Personen) in Anspruch genommen. Niemand hat von mir unmittelbar oder mittelbar geldwerte Leistungen für Arbeiten erhalten, die im Zusammenhang mit dem Inhalt der vorgelegten Dissertation stehen.

Die Arbeit wurde bisher weder im In- noch im Ausland in gleicher oder ähnlicher Form einer anderen Prüfungsbehörde vorgelegt.

Die geltende Promotionsordnung der Physikalisch-Astronomischen Fakultät ist mir bekannt.

Ich versichere ehrenwörtlich, dass ich nach bestem Wissen die reine Wahrheit gesagt und nichts verschwiegen habe.

Jena, den

Curriculum vitae

Author:	Robert Leitel
Date of birth:	19th January 1980 in Jena, Germany
Nationality:	German
Address:	Am Steinborn 3, 07749 Jena, Germany

- Career / Internships
    - since 2004 Research associate at Fraunhofer-Institute for Applied Optics and Precision Engineering, Jena
    - 2003 – 2004 Analysis of graded-index layers and rugate structures using optical *ex situ* and *in situ* spectroscopy (diploma thesis) at Fraunhofer-Institute for Applied Optics and Precision Engineering, Jena
    - 2000 – 2003 Construction of measurement devices for hardness evaluation of coated thermoplasts; *in situ* stress monitoring for thin-film deposition; optical characterization of coatings with mixed materials at Fraunhofer-Institute for Applied Optics and Precision Engineering, Jena
    - 2003 Coatings of high temperature superconductive by laser deposition at Institute of Solid State Physics, University of Jena
    - 2000 Generation of silica films for fiber sensors by tempering and development of software tools for calibratation of grating-polychromators at Institute for Physical High Technology, Jena
- Education
    - since 2004 graduate student at Friedrich Schiller University of Jena
    - 2004 – 1999 study of physics at Friedrich Schiller University of Jena (diploma)
    - 1991 – 1998 scientific grammar school "Ernst Abbe Gymnasium" (A-level)
- Special Interests
    - Certificates of photonics (major field of study), microelectronics (summer school), and optical thin-film design (Macleod)
- Language Skills
    - 1st language: german (native speaker)
    - 2nd language: english (B2-C1)
    - 3rd language: spanish (A1)
    - 4th language: russian (basic knowledge)